From the complex seismogram to the pertinent information: examples from the domains of sources and structure

Alessia Maggi

To cite this version:

Alessia Maggi. From the complex seismogram to the pertinent information: examples from the domains of sources and structure. Geophysics [physics.geo-ph]. Université de Strasbourg, 2010. tel-00782642

HAL Id: tel-00782642
https://theses.hal.science/tel-00782642
Submitted on 30 Jan 2013

UNIVERSITÉ DE STRASBOURG

MÈMOIRE

pour obtenir l'

HABILITATION À DIRIGER LES RECHERCHES
de l'Université de Strasbourg

Spécialité : **Sismologie**

préparée à **Ecole et Observatoire des Sciences de la Terre**

présentée et soutenue publiquement
par

Alessia Maggi

le 1 septembre 2010

Titre:

Du sismogramme complexe à l'information pertinente : exemples dans le domaine des sources et des structures.

Garant de HDR: **Jean-Jacques Lévêque**

Jury

M. Michel Cara,	Rapporteur, Président du jury
Mme. Valérie Maupin,	Rapporteur
M. Guust Nolet,	Rapporteur
M. Luis Rivera,	Examinateur
M. Ruedi Widmer-Schnidrig,	Examinateur
M. Jean-Jacques Lévêque,	Garant

Résumé

Les sujets de recherche que j'ai choisi de traiter ces dix dernières années sont relativement éclectiques, couvrant des aspects relatifs tant aux sources sismiques qu'à la structure de la Terre. Un thème fédérateur qui émerge cependant est mon intérêt pour les nombreuses méthodes utilisées en sismologie pour extraire l'information pertinente des sismogrammes. Dans cette thèse d'habilitation, je parcours le fil conducteur des idées qui ont contribué à former ma pensée sur ce thème, décrivant avec plus de détails deux méthodes que j'ai développées et qui ont abouti récemment: FLEXWIN, qui permet d'identifier automatiquement dans un sismogramme complexe les fenêtres temporelles de mesure les plus appropriées dans un certain contexte, et WaveLoc, qui détecte et localise automatiquement les phénomènes sismiques à partir de formes d'ondes continues en exploitant la cohérence de l'information sur un réseau de stations sismologiques. De tels outils, basés au départ sur l'intégration du savoir-faire "artisanal" et son automatisation, permettent en fait d'aller plus loin dans l'exploitation des sismogrammes, et sont devenus indispensables au sismologue pour faire face au volume de données gigantesque produit par les réseaux sismologiques modernes.

Abstract

My choice of research projects over the past decade has been rather eclectic, covering aspects relating to both seismic sources and Earth structure. There is, however, a consistent theme, and that is a fascination with the large variety of methods for extracting pertinent information from seismic data. In this thesis, I give an brief, largely chronological outline of the steps and insights that have informed my current thinking on this theme, going into more detail on two methods that I have recently developed: FLEXWIN, for automatically selecting the most appropriate time-windows on complex seismograms in which to make measurements, and WaveLoc, for automatically detecting and locating seismic phenomena from continuous waveform data by exploiting the coherence of information across a seismic network. Such tools, based on the the integration and automation of practical seismological "know-how", allow us to exploit seismological data more completely, and are becoming indispensable in the context of the enormous volume of data produced by modern seismic networks.

Contents

Chapter 1

Overview of past and current research

1 Introduction

A habilitation thesis is generally regarded as an occasion to look back on one's early years of research, and find a consistent theme that can be pursued in the future. I found this exercise particularly difficult, as my research over the past 10 years has spanned many subjects and fields, often with little apparent connection with each other. I had had the same difficulty when writing my PhD thesis in 2002, as I had undertaken three distinct subjects (earthquake depth determination, surface waveform tomography and source inversion from empirical Green's functions). It was through discussions with Dan McKenzie during the years of my thesis, and Jean-Jacques Lévêque during my time at EOST, that I started to understand what motivated my choices of research subjects: I am fascinated by the methods of extracting pertinent information from observations, by how these methods work, and how they can fail. I do not consider myself a theoretical seismologist, but more of a "data person" who, having had the good luck to learn to program very early on, is not afraid of developing software.

In this introductory chapter, I give a brief, largely chronological outline of the steps and insights that have informed my current thinking. Chapter 2 describes the first of two software packages I have developed recently, FLEXWIN, whose purpose is to automatically select, on pairs of observed and synthetic waveforms, those portions of the signal that should be used for measurement. As the FLEXWIN method is already published (Maggi et al., 2009), this chapter is relatively short, and concentrates more on the thinking behind the method than on the implementation details. Chapter 3 describes the second software package, WaveLoc, whose purpose is to detect and locate seismic phenomena using continuous data streams, and whose development is still ongoing. This rather long chapter covers the same material as a manuscript recently submitted to Geophysical Journal International, and describes the method in detail. In Chapter 4, I give a brief overview of current research efforts that are less strongly tied to the information extraction theme of this habilitation (mainly my work in Antarctica), and end with a perspective of the directions I plan to take in the near future.

2 Earthquake depths

When I started my PhD thesis in seismology in 1998, I knew next to nothing about the field, having come from a 4-years Physics program which had included only one course of Physics of the Earth containing no more than 8 hours of seismology. I started out with an apparently simple problem: inverting teleseismic waveform data for focal mechanism and earthquake depth (Maggi et al., 2000a,b, 2002). There was nothing revolutionary about the methods used in these early studies, but they were my training ground. I learned hands-on all about the insensitivity of teleseismic data to earthquake dip, about the trade-off between origin-times and earthquake depths, and about the all-important depth-phases, and how they modify the waveforms even for shallow earthquakes.

The depth distributions that came out of this early work, summarized in Figure 1.1, showed that continental earthquakes occur only in the crust and not in the upper mantle, and started a heated debate in the tectonics and geodynamics community regarding the rheology of the lithosphere, debate that has continued for a decade. There are two main camps in this debate: those that favor the 'jelly sandwich' model of lithospheric strength (a strong upper crust, a weak lower crust, a strong mantle) and those that favor the 'crème brulée' model (a strong crust over a weak mantle). The former camp is headed by Dan McKenzie, and the latter by Evegeny Burov, each producing a plethora of papers (see Jackson et al., 2008; Burov, 2010, for recent contributions).

A detailed analysis of the controversy, though interesting from a scientific point of view, is outside the scope of this habilitation thesis, because I have not participated in any of the work following the original re-determination of the continental earthquake depth distribution, and because the depths themselves have not since been called into question (see for example Adams et al., 2009, for confirmation of shallow continental seismicity in the Zagros mountains of Iran). The main lessons I

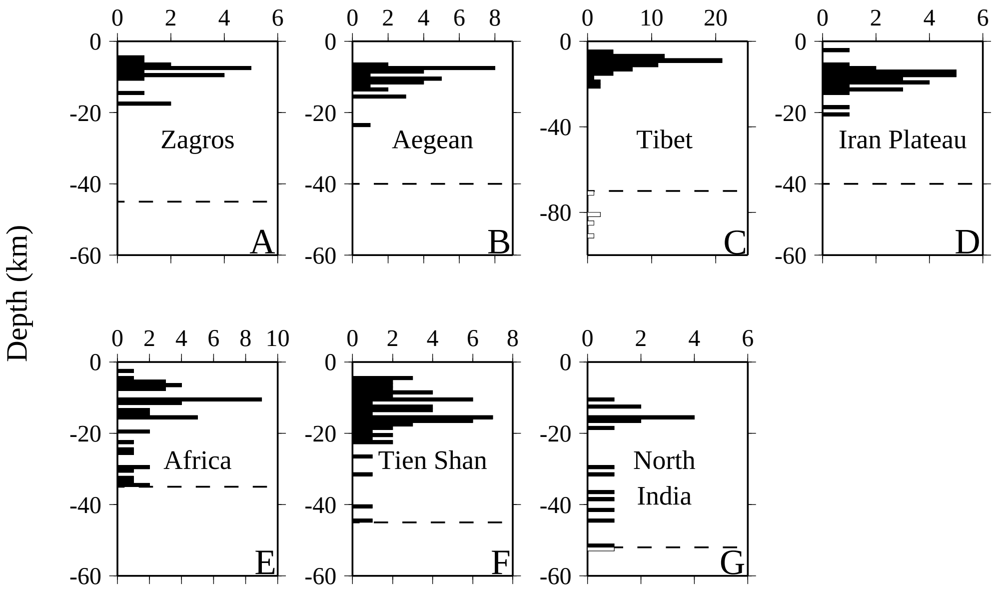

Figure 1.1: Histograms of earthquake focal depths determined by modeling of long-period teleseismic P (primary) and SH (secondary horizontal) seismograms (solid bars).White bar in North India (G) is depth determined from short period depth phases in Shillong Plateau by Chen and Molnar (1990). White bars in Tibet (C) are subcrustal earthquakes, but not necessarily in mantle of continental origin. Approximate Moho depths determined by receiver function analyses are indicated by dashed lines. (Maggi et al., 2000a, Fig.1)

learned from this experience were: (1) not to implicitly trust parameters in earthquake catalogs, especially not the hypocentral depth that can be incorrect by several tens of kilometers; (2) that the seismic waveform contains a wealth of information, often enough to resolve trade-offs inherent when using only selected parts of this information (i.e. phase arrival times); (3) that observations made by seismologists – even robust ones – can ignite furious debates in other communities, and that therefore one must take care not to introduce non-robust observations into the system.

3 Surface waveform tomography

After being convinced from this early work on source parameter estimation that the key to obtaining robust results was to use the information contained in the seismic waveform, I started working in the field of surface waveform inversion and tomography, both during my PhD and during my first Postdoc at EOST, where I explored two ‘competing’ multimode surface waveform inversion techniques: the Partitioned Waveform Inversion method of Nolet (1990), and the secondary observables method of Cara and Lévêque (1987) automated by Debayle (1999). I applied the first method to the Middle East (Maggi and Priestley, 2005) and the second to the Pacific Ocean

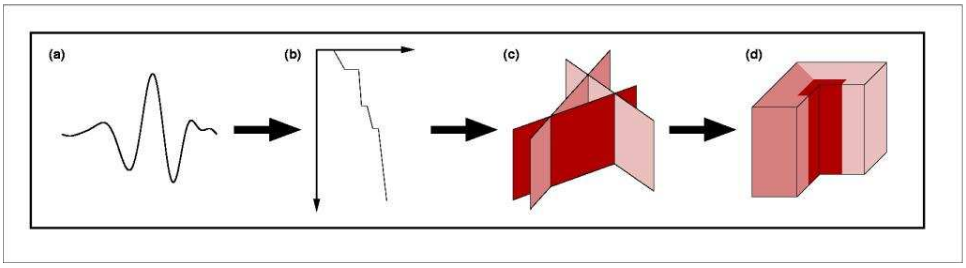

Figure 1.2: Basic schematic of surface waveform tomography: (a),(b) Use a waveform inversion technique to determine a 1-D path-average upper mantle S_V velocity model. (c),(d) Retrieve the local value of S_V from the set of path-average measurements by tomographic inversion.

(Maggi et al., 2006a,b).

Surface wave tomographies using these two methods share a common two-step framework, illustrated by Figure 1.2: the first step consists in a surface waveform inversion performed by matching mode-summation synthetic seismograms and observed regional surface waveforms from earthquakes with known focal parameters and depths, to produce 1-D velocity models along the great-circle propagation paths between sources and receivers; the second step consists in a tomographic inversion performed by combining the ensemble of 1-D models into a single linear system, that is then inverted by damped least squares inversion to determine the 3-D velocity model for the region. In this framework, the Nolet (1990) surface waveform inversion is paired with the Van der Lee and Nolet (1997) tomographic inversion, while the Cara and Lévêque (1987) surface waveform inversion is paired with the Debayle and Sambridge (2004) tomographic inversion.

Much could be written about the comparison between these two methods, which, though similar in framework, differ substantially in the implementation details. Such an exercise, though instructive for a detailed understanding of the waveform tomography problem, is once more outside the scope of this habilitation thesis, as I did not, myself, participate in the formulation of either method. I shall concentrate here on the personal considerations that I brought to two tomographic studies carried out with these methods.

In the first step of both tomographic methods, 1-D path-averaged velocity structures are obtained from measurements made on pairs of observed and synthetic seismograms, where the synthetic seismograms are constructed by assuming a starting 1-D velocity model and an earthquake location and focal mechanism. The problems inherent in the choice of 1-D starting velocity model, and the necessity of adapting this starting model to the crustal structure between the source and station, have been well documented in the literature and will not be repeated here. Given my

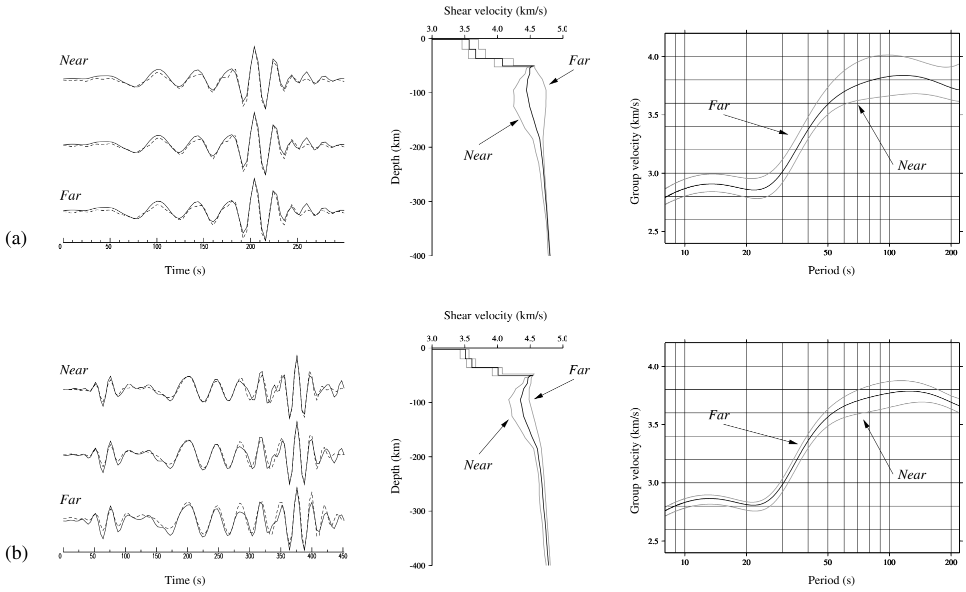

Figure 1.3: Sensitivity of 1-D waveform inversions to a ±50 km epicentral mislocation for (a) an event with epicentral distance ∼1700 km and (b) an event with epicentral distance ∼2500 km. Inversion velocity models and dispersion curves for the correct epicentral location are shown as thick black lines. If the epicentre is closer to the event than the true epicentre, then the phase arrivals will be late, and the waveform inversion will make the inversion velocity model slower to compensate; if the epicentre is further from the event than the true epicentre, the phase arrivals will be early, and the resulting inversion velocity model will be faster. The effects are more pronounced for shorter epicentral distances, but the quality of fit is always unchanged because the mislocation produces a timing error which does not change the amplitude and relative phase of any part of the seismogram. (Maggi and Priestley, 2005, Fig.2)

previous experience on earthquake depth and focal mechanism estimation, in which I had found numerous instances of large errors in the parameters given in earthquake catalogs, including the Engdahl catalog (Engdahl et al., 1998) and the Harvard CMT catalog, I started worrying about the influence these errors could have on the surface waveform inversion, and in particular that errors in the source parameters might be mapped into the inverted model as erroneous Earth structure.

At this time, I was working on a PWI tomography of the Middle East (Maggi and Priestley, 2005), a region for which earthquake epicenters and depths were notoriously inaccurate due essentially to the nonexistence or inaccessibility of local seismic networks, and the poor azimuthal coverage for teleseismic observations. Lateral errors in epicentral location in the region could reach up to 50 km (Lohman and Simons, 2002), and I had found that earthquake depths could also be in error by up to 50 km (Maggi et al., 2000a). Lateral errors map directly into the 1-D veloc-

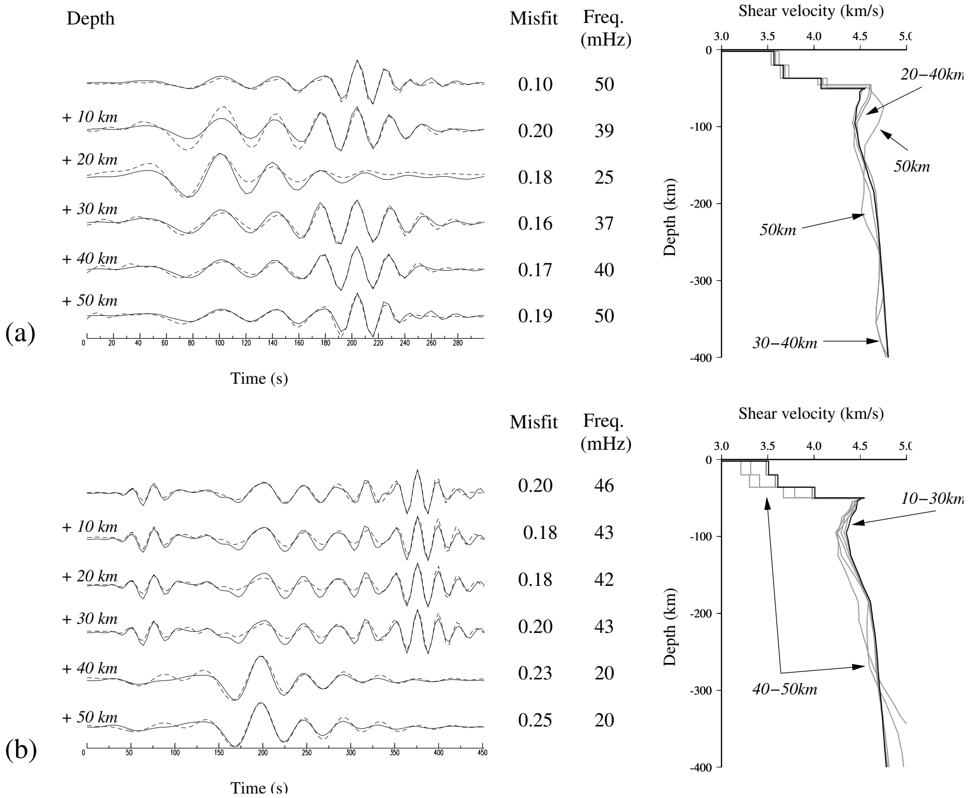

Figure 1.4: Sensitivity of 1-D waveform inversions to focal depths. The effects of varying focal depth for the two events in Fig 1.3: (a) focal depth 2 km (b) focal depth 9 km. Fits of final synthetic (dashed) to observed (solid) seismograms for shifts in focal depths of 10–50 km are shown on the left, and the corresponding inversion velocity models (thin lines) are shown on the right along with the velocity model for the correct depth (thick line). The misfit and maximum frequency achieved by the waveform inversion are denoted to the right of each waveform fit. (Maggi and Priestley, 2005, Fig.3)

ity models via the apparent group-velocity dispersion curves, without altering the waveform misfit (see Fig. 1.3). Depth errors lead to incorrect assumptions about the modal and frequency content of surface waves, and they can change the output 1-D velocity models significantly without necessarily having a large effect on waveform misfit (Fig. 1.4). Errors in focal mechanisms, not unknown in the Harvard CMT catalogue for this region (Dziewonski et al., 1981; Baker et al., 1993; Maggi et al., 2000a), also affect the reliability of the 1-D models as they lead to incorrect assumptions about the phase of surface waves.

Most tomographic algorithms take into account the estimated uncertainty in the data (in our case the path-averaged shear wave velocity models) used to drive the inversion. These data errors not only regulate the relative weight given to each datum within the inversion, but also regulate how far beyond the a-priori model variance the inversion will push the final model in order to fit the data within their errors.

However, if the data are unreliable and the data errors underestimate the true uncertainties, this same behavior can lead to artifacts in the final result. I have shown above that errors in earthquake epicenter, origin time and hypocentral depth affect directly the shear wave velocity models obtained by waveform inversion, without any influence on the quality of the waveform fit. These source errors lead to erroneous path-averaged shear wave velocity models coupled with underestimated uncertainties, and cause artifacts in the tomographic inversion. In order to reduce these artifacts, excessive smoothing is often used, leading to loss of horizontal resolution and a decrease in data fit.

In my Middle East and Pacific Ocean tomographic studies, I have used two different approaches to resolve this problem. The approach for the first study was to remove the unreliable data, while that for the second study was to obtain better estimates of the true data errors.

3.1 Middle East strategy: Remove unreliable data

In my Middle East study (Maggi and Priestley, 2005), I decided to be very stringent in the data selection, and only considered data from events for which focal mechanisms and depths had been independently determined by body waveform modeling. This approach drastically reduced the size of my dataset, and meant I could no longer assume the effects of epicentral mislocation would average out. However, artifacts in the 3-D velocity model caused by errors in focal depth and source mechanism were minimized. In order to isolate cases of significant epicenter mislocation, I com-

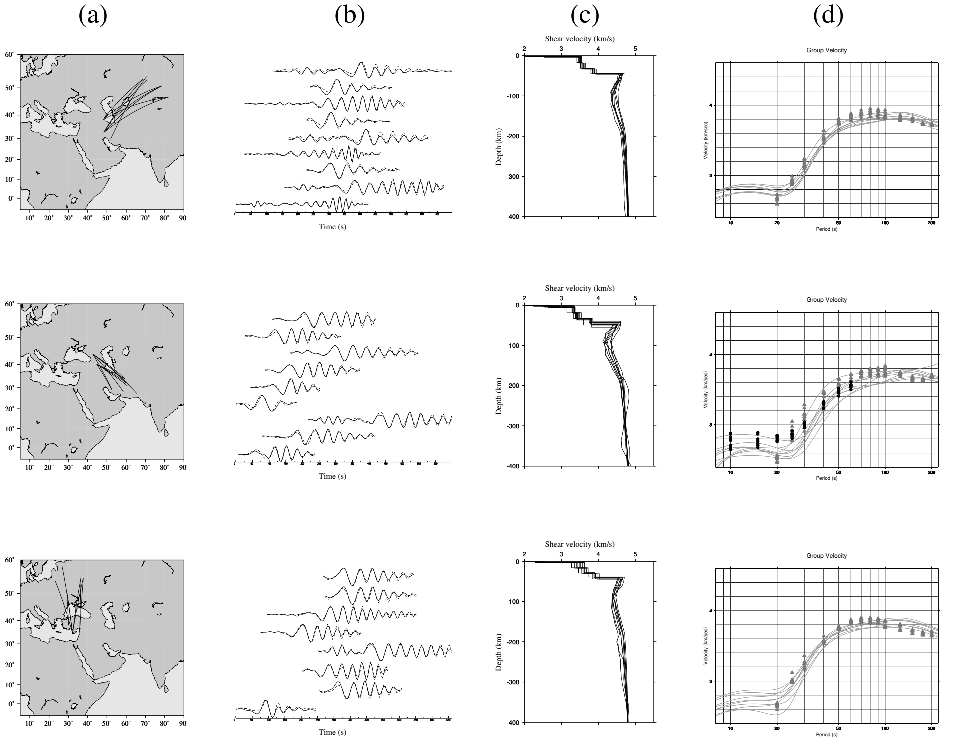

Figure 1.5: Examples of clustered 1-D results: (a) propagation paths; (b) waveform fits; (c) 1-D shear wave velocity models; (d) fundamental mode group velocity dispersion curves and path integrated group velocity values from Ritzwoller and Levshin (1998) (Gray triangles) and Pasyanos et al. (2001) (black circles). (Maggi and Priestley, 2005, Fig.4)

pared final waveform inversion 1-D models and their dispersion curves for clusters of similar paths, that should therefore have produced similar 1-D velocity models (Fig. 1.5). Comparison of inversion models within each cluster enabled me to identify and remove inconsistent data, but was still a ‘majority vote’ method and did not guarantee that the source parameters used in determining the remaining velocity models were accurate. I therefore went one step further, and compared velocity dispersion curves calculated from the final 1-D Earth models with the group velocity dispersion previously measured by Ritzwoller and Levshin (1998) and Pasyanos et al. (2001) (Figure 1.5d), to isolate any residual erroneous 1-D models.

Of the 1100 seismograms originally chosen for analysis, the above data selection procedure accepted 550 ‘good quality’ seismograms, many of which had very similar propagation paths. The resulting uneven geographical distribution biased the tomography results towards the structure of the regions with highest path density: multiple sampling along certain paths re-enforced the structure along those paths compared with that of the crossing paths, and led to smearing artifacts in the 3-D model. I therefore thinned the paths so as to render the path coverage as uniform as possible, selecting only the highest signal-to-noise ratio seismograms from each cluster. I was left with only 303 good quality and approximately evenly-distributed paths, the inversion of which produced the tomographic model presented in detail in Maggi and Priestley (2005), and shown in Figure 1.6.

Results

Figure 1.6a shows horizontal cross-sections through the 3-D tomographic model at 100, 150 and 250 km depth. The slices are color shaded by absolute shear wave velocity perturbation with respect to a common background model (Maggi and Priestley, 2005, Fig.6); poorly constrained areas are masked in gray. Also shown for guidance are the ray density and azimuthal coverage that are essential for a correct interpretation of the tomographic images. For example, the 250 km depth SE-NW trending slow anomaly between the Gulf of Oman and lake Balkhash in Kazakhstan passes at each end through zones of low path density, and is almost entirely contained within a region with poor azimuthal coverage, strongly suggesting that the elongated nature of the anomaly is an artifact due to smearing.

The most significant upper mantle feature of the shear wave velocity model is the low velocity zone extending beneath the Turkish–Iranian plateau. A similar image of this structure exists in the continental scale surface wave group and phase velocity maps for Asia (Ritzwoller et al., 1998; Curtis et al., 1998). Variation in shear wave velocity is caused by changes in temperature and composition as well

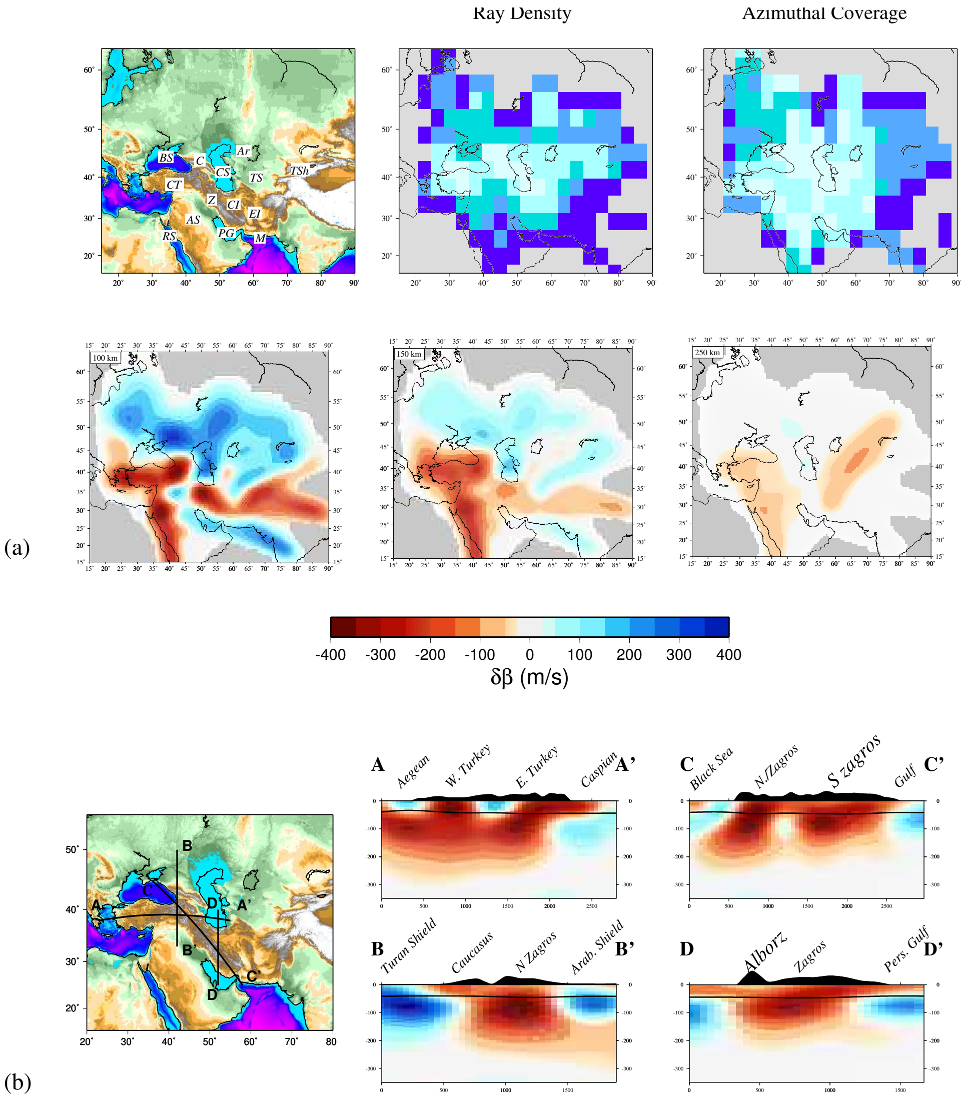

Figure 1.6: (a) Horizontal slices through the tomographic model at 100, 150 and 250 km depth. Also shown for reference are the geographic region, and the density and azimuthal coverage images. Abbreviations on topographic map: *BS* – Black Sea, *C* – Caucasus, *CT* – Central Turkey, *CS* – Caspian Sea, *Ar* – Aral Sea, *TS* – Turan Shield, *TSh* – Tien Shan, *Z* – Zagros, *CI* – Central Iran, *EI* – Eastern Iran, *RS* – Red Sea, *AS* – Arabian Shield, *PG* – Persian Gulf, *M* – Makran. (b) Vertical cross-sections both along and across the Turkish Plateau and the Zagros mountains of southern Iran. Depths and distances along the profiles are given in km. Elevations, shown in black above the plots, are exaggerated by a factor of 10. (Maggi and Priestley, 2005, Fig.7)

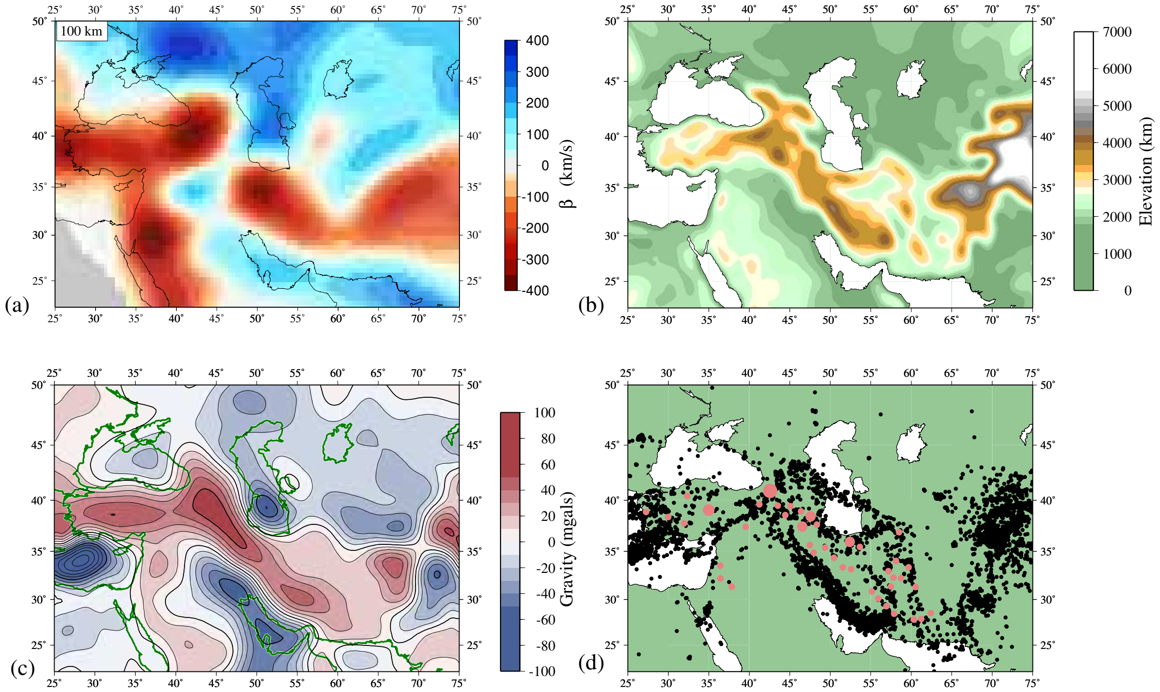

Figure 1.7: Comparative images of the Middle East. (a) Tomographic slice at 100 km depth; (b) regional topography low-pass filtered at 400 km; (c) free–air gravity anomalies (EGM96, Lemoine et al., 1996) low–pass filtered at 800 km; (d) regional seismicity (black circles) 1964-1998 from Engdahl et al. (1998), and Neogene–Quaternary volcanic outcrops (pink circles) (Haghipour and Aghanabati, 1989; Alavi, 1991; Choubert and Faure-Muret, 1976). (Maggi and Priestley, 2005, Fig.10)

as by the presence of volatiles and partial melt. The low shear wave velocities observed beneath the Turkish–Iranian plateau and the recent volcanism suggest that the upper mantle in this region is above the solidus temperature, a suggestion confirmed by the poor S_n propagation found in the same region (Kadinsky-Cade et al., 1981; Rodgers et al., 1997; Sandvol et al., 2001).

Figure 1.7 compares the pattern of low shear wave velocity observed at ∼100 km depth in the tomographic model with other geophysical and geological observations suggesting a warm, low density upper mantle beneath the Turkish–Iranian plateau. Figure 1.7c shows long wavelength (800–3500 km) free air gravity anomalies from the EGM96 dataset (Lemoine et al., 1996). There is a striking correlation between the gravity high running under the Turkish peninsula and the Zagros Mountains, and the low velocity anomaly beneath the same regions (Fig. 1.7a). Long wavelength free air gravity anomalies reflect density differences in the mantle: less dense mantle is buoyant and will tend to rise, creating an upward deflection of the surface. This

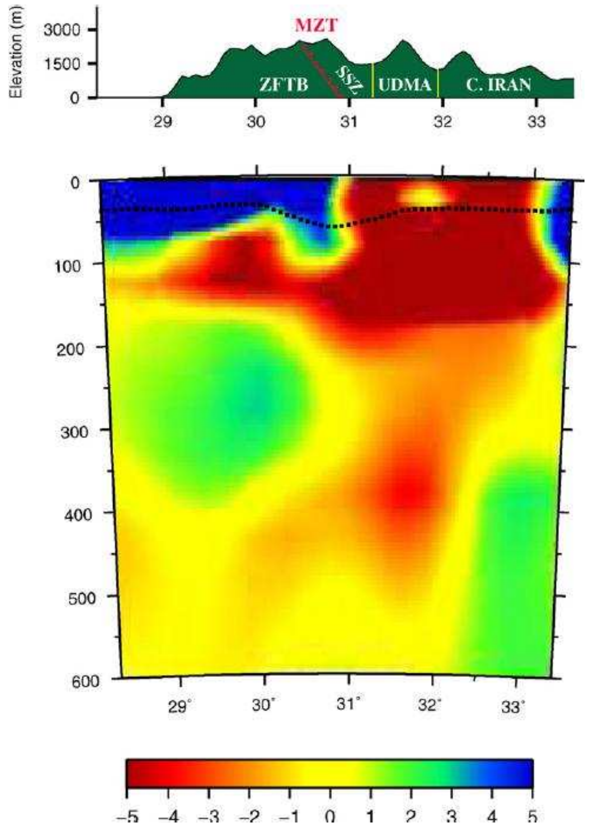

Figure 1.8: The vertical cross-section shows the model for the upper 600 km along the Zagros profile. The velocity scale saturates at ±5% of the reference background model. The dotted line shows Moho depth variations along the Zagros profile resulting from the inversion. Vertical and horizontal axes are depth (km) and latitude (degree) along the profile, respectively. The main tectonic units and elevation variations along the Zagros profile are also shown in the top panel. (Manaman and Shomali, 2010, Fig.8)

deflection produces a larger positive gravity anomaly than the negative anomaly caused by the density deficit itself, thereby producing an overall positive anomaly and a correlation between long wavelength free air gravity anomalies and long wavelength topography. The density differences in the mantle are most likely caused by temperature differences. The distribution of volcanism across the Turkish–Iranian plateau also suggests a warm upper mantle as the source for the low shear wave velocities. Figure 1.7d shows the correlation between the locations of the low shear wave velocity zone and recent volcanism.

In Maggi and Priestley (2005) we suggest that the upper mantle low shear wave velocity zone, the high free air gravity, and the deep lithospheric source depth for the basaltic volcanism are consistent with a partial delamination of the lower lithosphere (Pearce et al., 1990; Keskin et al., 1998), caused by an instability due to earlier thickening of the lithospheric during the continental collision of Arabia and Eurasia. This interpretation has been called into question by later studies that prefer a slab break-off scenario (e.g. Paul et al., 2006), based partly on evidence for crustal-scale thrusting in the Zagros and on the shallow depths of earthquakes there (Maggi et al., 2000b). The broken-off slab has not yet been unequivocally seen in tomographic images, because of the requirement for high resolution at transition zone depths, which is difficult to obtain. Manaman and Shomali (2010) have performed a new PWI tomographic inversion of the Iranian region using data from the Iranian regional network and from the seismic profile across the Zagros mountains of Paul et al. (2006). They see hints of a high velocity region below Central Iran at depths of 400–600 km (Figure 1.8), but warn that the anomaly is at the limit of their resolution. The question of slab break-off for the Arabia–Eurasia collision remains to be resolved.

3.2 Pacific Ocean strategy: Estimate data errors

In my Pacific Ocean study (Maggi et al., 2006a,b), I analyzed vertical component Rayleigh wave seismograms from all earthquakes of magnitude greater than M_W 5.5 that occurred between January 1977 and April 2003, and for which the $R1$ portion of the surface waves propagated exclusively in the Pacific Ocean hemisphere (i.e. between 120E and 300E). These earthquakes occurred mostly on the subduction zones surrounding the Pacific Plate, and to a lesser extent on the mid-ocean ridges. The vast majority of the recordings were obtained from the public IRIS (Incorporated Research Institutions for Seismology) and GEOSCOPE databases, with the addition of a few thousand recordings from two years of temporary deployment of 10 seismograph stations in French Polynesia (PLUME, Barruol et al., 2002). These Polynesian records provided extra coverage in the South Pacific, allowing me to improve the resolution in this region compared to previous studies. The full data-set contained several hundred thousand seismograms.

The Debayle (1999) automated waveform procedure left me with a very large number of 1-D paths (56,217), so I decided to obtain a better estimate of the data errors by comparing multiple path averaged measurements along repeatedly sampled propagation paths. I clustered the path-averaged models geographically with a cluster radius of 200 km, and treated the shear wave models that formed each cluster as independent measurements of the average shear wave velocity profile along the common path (see Figure 1.9a for the ray density of the resulting 15,165 clusters). I took the path-averaged profile and depth-dependent measurement error

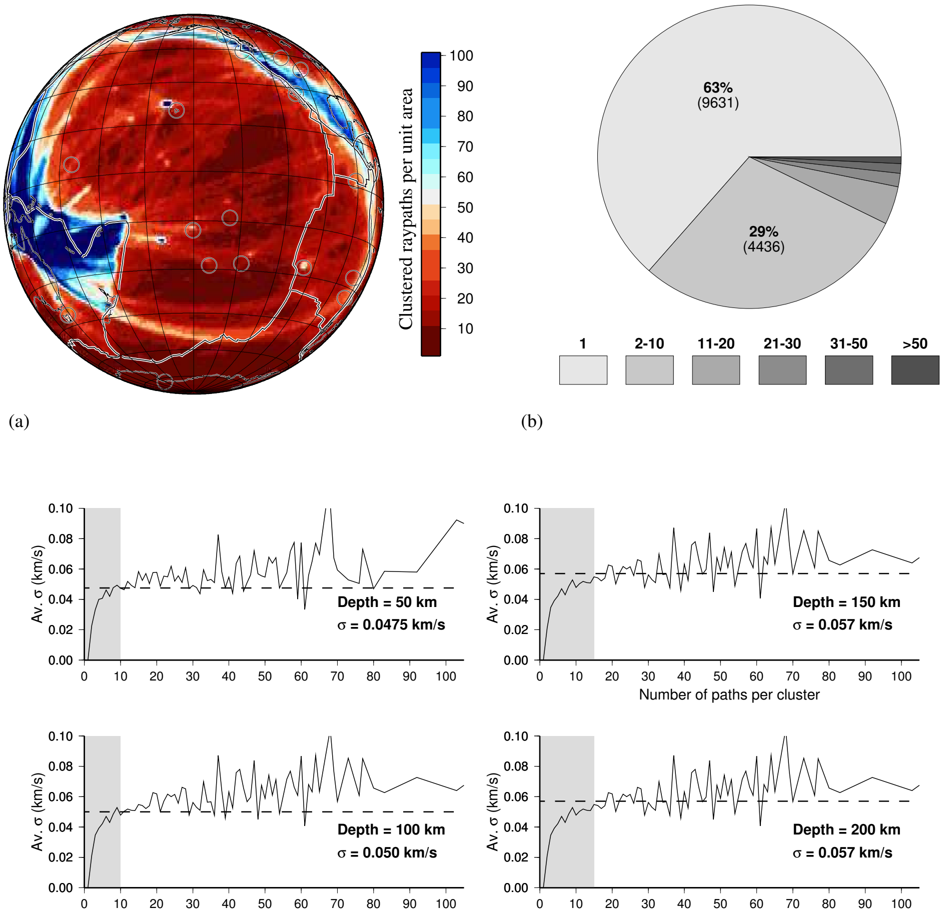

(a)

(b)

(c)

Figure 1.9: (a) Ray density for the 15,165 clusters. The unit area is the area of a one degree cell at the equator. (b) The distribution of cluster sizes. Shading indicates the range of cluster sizes (1 path, 2–10 paths, 11–20 paths etc.); the percentage of clusters that fall in the two most populated bins are shown on the pie-chart, above the number of clusters in the bin (in brackets). (c) The average σ for clusters *vs* cluster size at depths of 50 to 200 km (solid lines). The average σ oscillates around a central value $\bar{\sigma}(z)$ indicated by the dashed lines and given within the plot. For each depth, the range of cluster sizes for which small number statistics seem to apply (10–15) is highlighted in gray. (Maggi et al., 2006a, Fig.4)

associated with each cluster to be respectively the mean and the standard deviation on the mean of the 1D shear wave velocity models of its component paths.

Of the 15,165 clustered ray-paths, 63% contained only one path (see Fig. 1.9b), and therefore represented a single shear wave velocity measurement with no error estimate other than the a-posterior waveform fitting error. In order to use these single–path models in the tomography, they need to be assigned a reasonable data error. I averaged at each depth all the standard deviations calculated for a given cluster size. I found that this average standard deviation increased rapidly with cluster size for small clusters, before tending towards a constant value (see Fig. 1.9c). This suggested that the low value of σ for the smaller clusters was simply a low-number sampling effect, and that if there had been more data for these clusters, the standard deviation would increase to become compatible with the larger clusters. I therefore used the flat portion of the curve to set an equivalent $\bar{\sigma}$ for small clusters, as shown in Fig. 1.9c, from which I calculated the corresponding data error $\sigma_D(z) = \bar{\sigma}(n)|_z/\sqrt{n}$.

The azimuthally anisotropic tomographic model obtained using this improved estimation of data errors, presented in detail in Maggi et al. (2006a) and Maggi et al. (2006b) and shown in Figures 1.10 and 1.11, enabled me to analyse the dependence of seismic velocity on the age of the oceanic lithosphere, to recover the signature of the French Polynesian plumes, and to discuss plate-motion related and plume-perturbed azimuthal anisotropy.

Dependence of seismic velocity with age

The longest wavelength isotropic feature of the tomographic model shown in Figure 1.10 is the increase in V_{SV} with increasing ocean age, progressing from East to West across the Pacific plate. An intuitive image of the dependence of V_{SV} on age can be found in the age-dependent average cross-section for the Pacific Ocean lithosphere in Figure 1.12, which was created by taking sliding window averages of the tomographic results at depths from 40 to 225 km along the isochrons of Müller et al. (1997). V_{SV} contours in Fig. 1.12 deepen progressively with age, approximately following the trend predicted by Parker and Oldenburg (1973) for purely diffusive cooling. The large oscillation for ages >140 Ma coincides with a region of large scatter in V_{SV}, and should not be interpreted as a robust feature in the average cooling trend.

In Maggi et al. (2006a), I compared the observed trend for V_{SV} with ocean age against three representative and well-known cooling models: the half-space cooling model of Parker and Oldenburg (1973) (hereafter referred to as HSC), the Parsons

(a) 50 km (b) 100 km

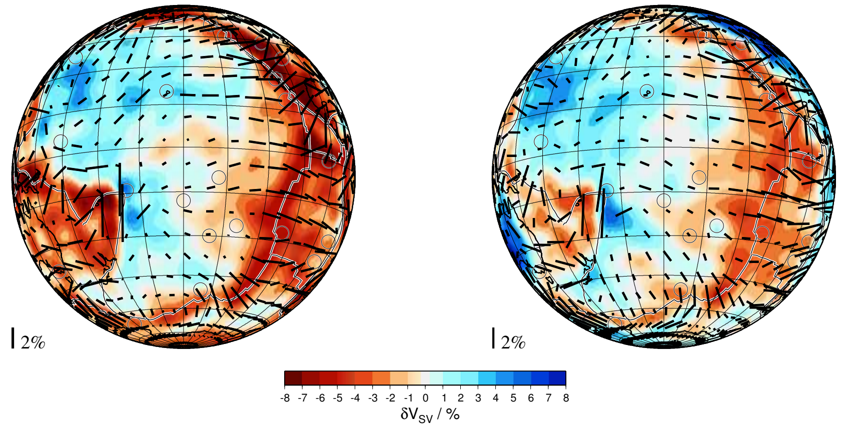

(c) 150 km (d) 200 km

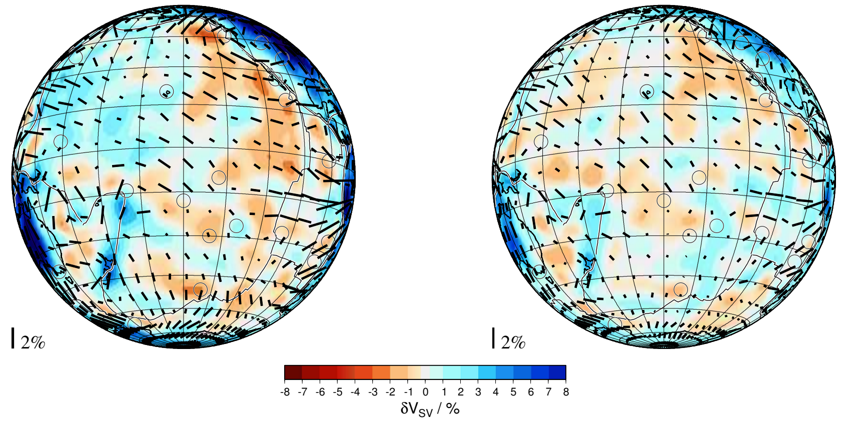

(e) 300 km (f) 400 km

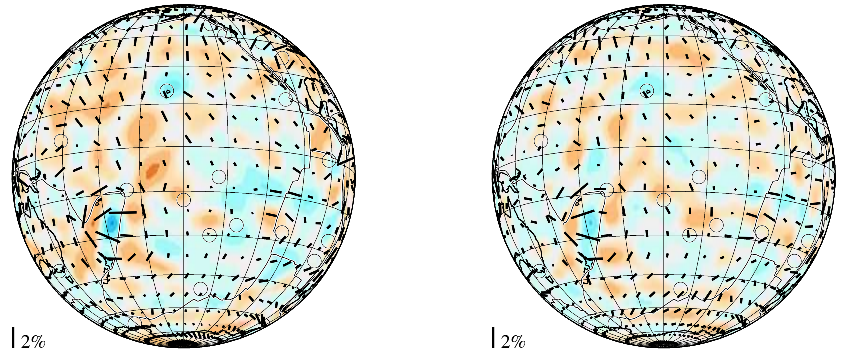

Figure 1.10: The tomographic inversion at (a) 50 km, (b) 100 km, (c) 150 km, (d) 200 km, (e) 300 km and (f) 400 km depth. The isotropic component of V_{SV}, expressed as a percentage variation with respect to the model average, is indicated by the color shading. The azimuthal anisotropy results are plotted as black segments whose direction is parallel to the fast–V_{SV} direction, and whose length is proportional to the amplitude of the anisotropy (the difference between maximum and minimum V_{SV} expressed as a percentage of the model average). The black bar at the side of each plot is a scale bar representing 2% anisotropy. (Maggi et al., 2006b, Fig.7)

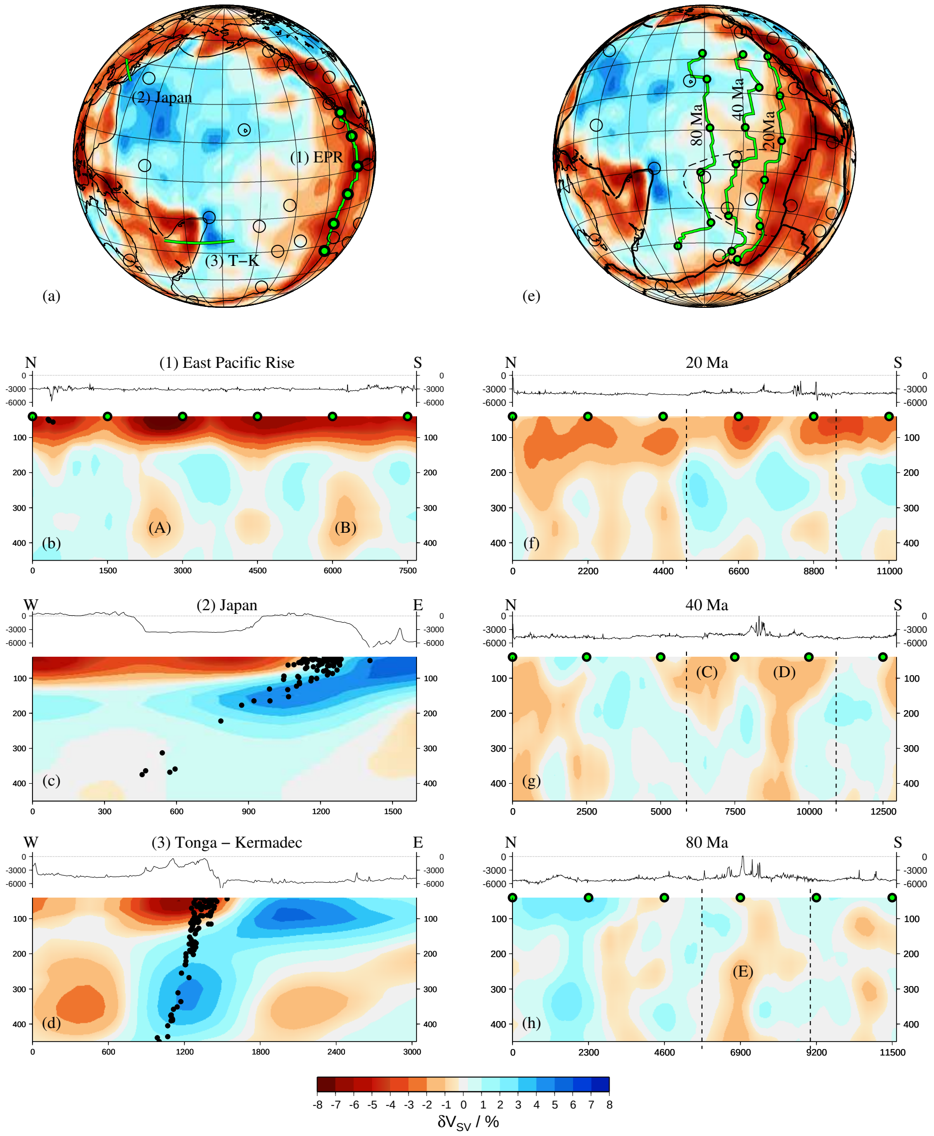

Figure 1.11: Selected cross-sections through our tomographic model. (a) Location of cross-sections shown in panels (b) to (d). (e) location of cross-sections shown in panels (f) to (h); the approximate boundary of the region of anomalously elevated sea-floor topography known as the South Pacific Super-Swell is indicated by a dashed line. The intersections of this boundary with the 20–80 Ma isochron profiles in panels (f)–(h) are indicated by vertical dashed lines. Green/black circles along the EPR profile in (a) and the 20–80 Ma isochron profiles in (e) correspond to the circles in panels (b), (f)–(h) and are used as distance markers. Sea-floor topography profiles from Smith and Sandwell (1997) are shown above each tomographic cross-section. Earthquakes from the Harvard CMT catalog within 200 km of the profiles are shown as small black circles. (Maggi et al., 2006a, Fig.6)

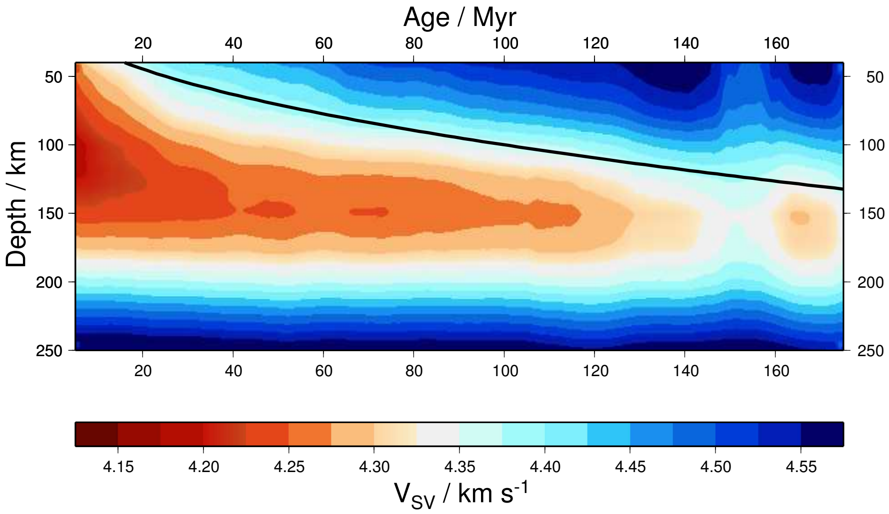

Figure 1.12: Tomographic cross-section with respect to age for the Pacific Ocean region. This smoothed image was created by averaging V_{SV} along the Müller et al. (1997) isochrons, using a sliding age window of 10 Ma width and excluding areas with no age information. Color shading represents absolute V_{SV}. The continuous black line indicates the position of the thermal boundary layer for the Parker and Oldenburg (1973) half-space cooling model. (Maggi et al., 2006a, Fig.10)

and Sclater (1977) plate model (hereafter referred to as PS) and the GDH1 plate model of Stein and Stein (1992). All three lithospheric cooling models fit the age-binned seismic velocities within their standard deviation, therefore the tomography itself could not formally rule out any of them. The best fit to the overall shape of the V_{SV}–age trend was provided by the Stein and Stein (1992) GDH1 plate model, while HSC model and the PS thick-plate model were almost indistinguishable in terms of goodness of fit.

In order to test the robustness of any interpretation of the V_{SV}–age curves, I performed a synthetic tomographic experiment using a PREM + HSC input model (Maggi et al., 2006a). I computed the path averaged shear wave velocity models along each of the 15,165 paths, and imposed the same values of σ_D used in the original inversion; I then inverted this tomographic model under the same conditions as the real tomographic inversion. The shape of the output V_{SV}–age trend was distinctly flatter than the input model between 60 and 100 Ma, and seemed to be fit better by the GHD1 model than by the HSC model. The tomographic inversion, therefore, tended to flatten the true V_{SV}–age trend, calling into question my earlier conclusion that a thin plate model provided the best fit to the surface wave observations, and suggesting that a half-space cooling model or a thick plate model was more appropriate, in accordance with most previous surface wave studies of lithospheric cooling (Forsyth, 1977; Zhang and Tanimoto, 1991; Zhang and Lay, 1999).

In a more recent, high resolution tomographic inversion of the East Pacific rise, Harmon et al. (2009) revisited the question of the conductive cooling model. They jointly inverted the data from two long-term broad-band ocean-bottom seismometer deployments, MELT and GLIMPSE, both close to the East Pacific Rise at 17°S. The study area covered seafloor of 0–8 Ma in age, and provided an order of magnitude better spatial resolution than that available in other studies. They found that the 16–33 s period Rayleigh wave phase velocities showed a strong square-root of seafloor age dependence, confirming that conductive cooling plays an important role in developing the seismically fast lid in the oceans.

Images of mantle plumes in French Polynesia

Panels (e)–(h) in Fig. 1.11 focus on my tomographic results for the South Pacific Super-Swell region, a shallow bathymetric anomaly (indicated by a dashed line in Fig. 1.11e) that has been postulated to be the surface expression of a large-scale mantle super-plume in the south-central Pacific Ocean (see e.g. McNutt and Fischer, 1987; Sichoix et al., 1998; Mégnin and Romanowicz, 2000). This region is characterized by an increased rate of volcanism compared to other oceanic regions of similar age, and has been reported as having anomalously slow shear wave velocity by a number of surface wave tomographic studies (e.g. Ekström and Dziewonski, 1998; Montagner, 2002). The panels show cross-sections through the Super-Swell region and the adjacent regions of the Pacific plate, taken along the 20, 40 and 80 Ma isochrons as defined by Müller et al. (1997). The 20 Ma profile shows a localized low shear wave velocity anomaly within the Super-Swell region confined to the upper 100–150 km of the mantle. The 40 Ma profile shows two low velocity anomalies (C and D) within the Super-Swell region, associated with the approximate locations of the Marquesas and Macdonald hotspots respectively. The anomaly associated with the Macdonald hotspot (D) is continuous down to $\sim$420 km depth, as is the broad low velocity anomaly at the northern end of this profile, indicating a possible thermal upwelling from the transition zone. The 80 Ma profile shows a narrow low velocity anomaly (E), apparently also of thermal origin, rising from the transition zone close to the location of the Society hot-spot. It seems clear that the low velocity anomalies in the Super-Swell region, imaged with higher resolution thanks to the data from the PLUME experiment, are confined to localized structures, and are not pervasive throughout the entire area.

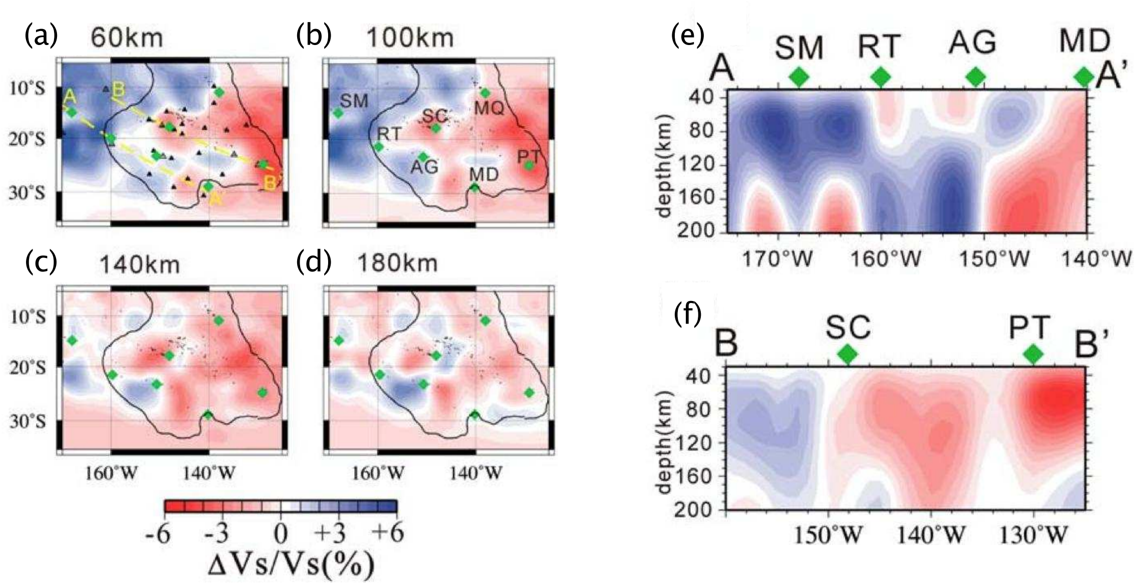

Figure 1.13: S wave velocity model in the upper mantle beneath the South Pacific. Lateral variation in S wave velocity at depths of (c) 60, (d) 100, (e) 140, and (f) 180 km. Green diamonds are active hot spots. Two-letter labels on the diamonds are the abbreviated names of the hot spots: SM, Samoa; RT, Rarotonga; SC, Society; AG, Arago; MD, Macdonald; MQ, Marquesas; PT, Pitcairn. The solid curve indicates the superswell region defined by anomalous seafloor uplift greater than 300 m. Black triangles in (a) denote temporary PLUME or BBOBS stations. Curves A-A' and B-B' in Figure 4c indicate locations of cross section shown in (e) and (f). (Adapted from Suetsugu et al., 2009, Fig.4 and Fig.5)

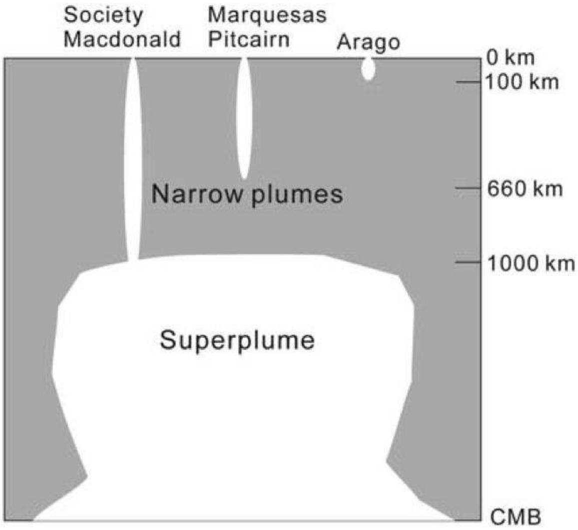

Figure 1.14: A cartoon illustrating the possible relationships between the deep superplume and narrower and shallower plumes beneath the South Pacific superswell. The superplume is located in the lower mantle from the core-mantle boundary to 1000 km depth. Narrow plumes beneath the hot spots may have various depth origins. The Society and Macdonald hot spots are likely deeply rooted down to the superplume head, while other hot spots may have origins in the transition zone (Pitcairn and perhaps Marquesas) or in the uppermost mantle (Arago). (Suetsugu et al., 2009, Fig.12)

In a more recent study, including data from a BBOBS (broad-band ocean-bottom seismometer) deployment in French Polynesia as well as the PLUME data, Suetsugu et al. (2009) also find low velocity anomalies of 2–3% near the Society, Macdonald, Pitcairn and Marquesas hotspots, that could represent narrow plumes in the upper mantle, confirming my observations (Figure 1.13). They also confirm that the average *S* velocity profile beneath the South Pacific superswell is close to that of other oceanic regions whose seafloor is of a similar age, suggesting that the slow anomalies are localized. In the same study, Suetsugu et al. image large scale low-velocity anomalies in the superswell region, extending from the base of the mantle to a depth of 1000 km, and indicative of a superplume. They speculate that the superplume may be a hot and chemically distinct mantle dome, and that small-scale anomalies in the shape of narrow plumes may be generated from the top of the dome, as shown by the cartoon in Figure 1.14.

Anisotropy, plate motion, and mantle plumes

According to the commonly held perception of the evolution of the oceanic mantle, the ridge-normal mantle flow signature close to the mid-ocean ridges is expected

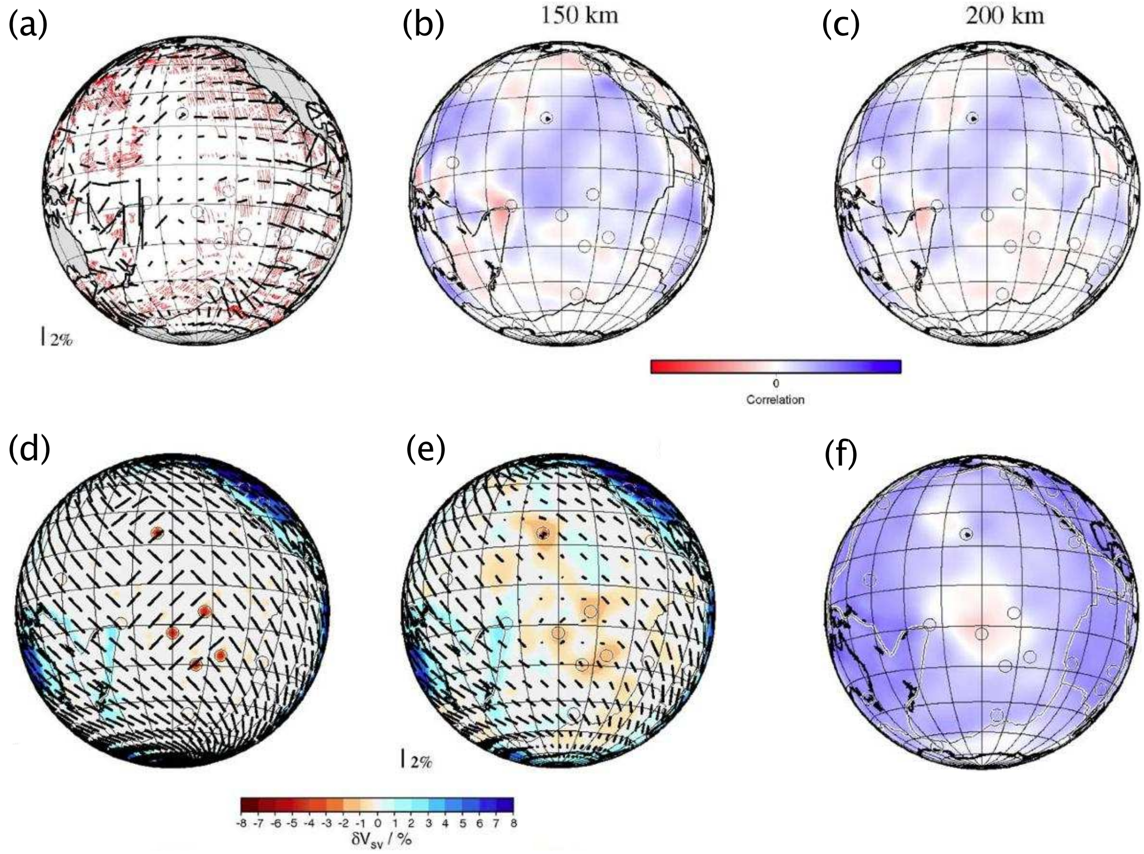

Figure 1.15: (a) Shallow anisotropy and oceanic magnetic anomalies. The azimuthal anisotropy results for 50 km depth plotted above the magnetic anomaly traces. Magnetic anomalies are from Cande et al. (1989). (b)-(c) The correlation between the fast V_{SV} direction and the direction of absolute plate motion (APM) calculated from NUVEL1 in the no-net rotation reference frame. Areas of strong correlation (anisotropy and APM directions are parallel) are shown in blue; areas of strong anti-correlation (anisotropy and APM directions are perpendicular) are shown in red; areas of weak correlation (either the directions of anisotropy and APM are at 45° to each other, or one of the two quantities is small) are shown in lighter shades of the two colors. (d)-(f) Synthetic test for the recovery of plume-related disturbances in azimuthal anisotropy: (d) synthetic input model with uniform 2% NW-trending anisotropy, 5 plumes of radius 200 km and 5% shear wave anomaly, and parabolic regions of rotated anisotropy; (e) output of the synthetic test; (f) correlation of the output model with respect to a 'plate motion' (velocity 100 mm/yr) parallel to the background anisotropy. (Adapted from Maggi et al., 2006b, Fig.8-10)

to ‘freeze’ into the fabric of the lithosphere, through lattice–preferred–orientation (LPO), as the lithosphere cools, becomes more viscous, thickens, and moves away from the ridge axis (McKenzie, 1979). The fast directions of anisotropy at lithospheric depths are therefore expected to remain perpendicular to the magnetic lineations of the same age (e.g. Nishimura and Forsyth, 1989; Smith et al., 2004). Figure 1.15a shows a comparison of my azimuthal anisotropy results at 50 km depth (in the lithosphere of all but the youngest oceanic regions), with catalogued magnetic anomalies (Cande et al., 1989). The agreement is particularly good in the younger oceans, where fast azimuthal anisotropy directions are consistently perpendicular to magnetic lineations.

We observe in Figure 1.10 that the directions of anisotropy, which are heterogeneous in the older oceans at shallow depth, tend to align themselves in longer–wavelength patterns consistent with the directions of plate motion as the depth increases and we pass from the lithosphere into the asthenosphere. Figures 1.15b,c map the correlation between azimuthal anisotropy and the directions of absolute plate motion (APM). At 150 and 200 km depth the region of good correlation (blue in the images) covers most of the Pacific Ocean. These correlation plots and the correspondence at shallow depths between azimuthal anisotropy directions and magnetic anomalies confirm the hypothesis — dating back to the earliest anisotropic studies and still in use today (Nishimura and Forsyth, 1989; Smith et al., 2004) — of stratification of the anisotropic structure in the Pacific ocean, with fossil anisotropy related to spreading directions in the lithosphere, and anisotropy conforming with current plate motion in the asthenosphere.

Also visible in Figures 1.15b,c are anomalous regions, in which the correlation between azimuthal anisotropy and the direction of absolute plate motion breaks down. These anomalous regions are large (1000–3000 km), and are located in the vicinity of known hot-spots: Bowie, Juan de Fuca, Hawaii, Solomon, Samoa, Galapagos, Easter Island, Society, Marquesas, MacDonald and Louisville. This geographical correspondance suggests that the observed perturbation to the plate-motion oriented anisotropy may be related to mantle upwelling associated with these hot-spots. Fluid dynamical models of the interaction between an axisymmetric upwelling plume and the simple shear flow induced by a moving plate produce a flow with a roughly parabolic pattern centered over the plume, with a width several times the plume’s diameter (Kaminski and Ribe, 2002). Subsequent numerical modeling of lattice preferred orientation (LPO) in this complex flow pattern using plastic deformation and dynamic re-crystallisation models predicts that the fast axes may orient themselves almost perpendicular to the parabolic flow pattern. Although the upwelling plumes

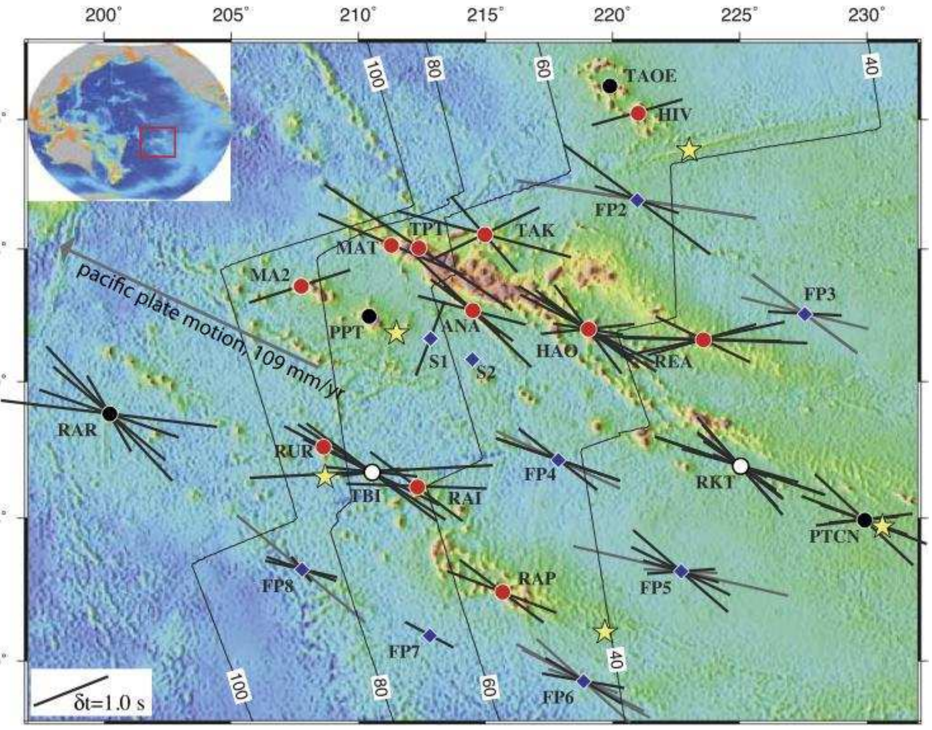

Figure 1.16: Bathymetric map of French Polynesia, showing the BBOBS (blue diamonds), the PLUME (red circles), the IRIS/GEOSCOPE (black circles), and the LDG/CEA stations (white circles). Stars indicate locations of hotspots. Black bars represent good and gray bars fair quality measurements: The azimuth of each bar represents the fast split direction and its length the delay time between the two split arrivals. Null and anomalous splitting observations at S1 and S2 are taken as evidence for parabolic asthenospheric flow. (Barruol et al., 2009, Fig.1)

themselves are too narrow for their intrinsic anisotropic signature to be resolved, I suggested in Maggi et al. (2006b) that the large-scale perturbations of mantle flow induced by the plumes should be detectable using surface wave azimuthal anisotropy.

Figures 1.15d-f show a synthetic test designed to determine the behavior of the tomographic inversion in the presence of a strong, plume-generated disturbance of the azimuthal anisotropy pattern with the geometry predicted by Kaminski and Ribe (2002). After the inversion (Figure 1.15e), the main NW-trending azimuthal anisotropy is well-recovered over most of the model, albeit with a reduction in amplitude of up to a factor of two in some regions. The 90° perturbation to the anisotropic directions present in the input model is not recovered in the synthetic inversion, however the resulting anisotropic pattern is still perturbed compared to the background NW trending pattern, as is confirmed by the correlation plot (Figure 1.15f). Furthermore, the size and amplitude of the anti-correlation anomalies recovered in this test are similar to those found in our tomographic inversion. This test indicates that although we do not have sufficient resolution to recover the pattern of a small or medium-scale disturbance in the anisotropy, we are able to detect its presence if the disturbance is severe enough. Recently, further evidence of parabolic asthenospheric flow may have been found from SKS splitting measurements at ocean bottom seismometers up-stream of the Society hotspot (Barruol et al., 2009).

4 Towards full waveform tomography

The above studies using two different surface waveform tomography methods left me with the impression that, so long as the tomographic methods are well thought out and self-consistent, and the data used do not violate the assumptions and approximations made by the methods, the end quality of a tomographic model is directly related to the the data themselves, and the procedures used in selecting the data, making the measurements (i.e. extracting the primary information from the data), and evaluating the true uncertainties on these measurements.

When I was starting out in tomography, discoveries were already being made about the volumetric sensitivity of certain seismic measurements (Marquering et al., 1999; Zhao et al., 2000; Dahlen et al., 2000), which opened up the possibility of calculating accurate analytic sensitivity kernels in 1D media (e.g. Dahlen and Baig, 2002; Dahlen and Zhou, 2006). These kernels were rapidly taken up by tomographers (e.g. Montelli et al., 2004; Zhou et al., 2006) to produce new 3D Earth models. The information that went into this generation of 3D Earth models was derived from measurements made with respect to synthetic seismograms (or synthetic traveltimes) generated using 1-D Earth models. I had no doubts that the analytic 1D sensitivity kernels would improve the first iteration of the tomographic process, the one producing the first 3D intermediate model, but what about the following ones? Were these kernels still appropriate for the further iterations? Could one really continue the process without re-measuring, and without updating the sensitivity kernels?

At the same time, advances were also being made in computational methods for forward modeling seismic propagation in fully 3D media (Komatitsch and Vilotte, 1998; Komatitsch et al., 2002; Capdeville et al., 2003), and for calculating numerical sensitivity kernels in 3D media (e.g. Capdeville, 2005; Tromp et al., 2005; Zhao et al., 2005; Liu and Tromp, 2006, 2008), thereby opening up the possibility of '3D-3D' tomography, i.e. seismic tomography based upon a 3D reference model, 3D numerical simulations of the seismic wavefield, and finite-frequency sensitivity kernels (Tromp et al., 2005; Chen et al., 2007). Measurements and sensitivity kernels could now be made for the full seismic waveform, and updated at each iteration.

This new type of tomography would require a new type of automated data-selection strategy, in order to maximize the amount of pertinent information fed into the system at each iteration, and minimize the amount of noise. My second Postdoc, at Caltech, was dedicated to designing and implementing the data-selection strategy for the adjoint tomography method of Tromp et al. (2005). The resulting software package, FLEXWIN (distributed to the community via the Computational Infrastructure for Geodynamics, `http://www.geodynamics.org`) has been downloaded by researchers all over the world, and was pivotal to producing the adjoint tomography model of Southern California (Tape et al., 2009, 2010). The FLEXWIN algorithm is described in detail by Maggi et al. (2009), a shortened version of which forms the main part of Chapter 2.

5 Coherence and earthquake location

In both the surface waveform inversion methods and the measurement methods used for adjoint tomography, the extraction of pertinent information to be tomographically inverted was carried out one path at a time, by comparing pairs of observed and synthetic seismograms. The coherence of the information extracted in this manner only came into play during the tomographic inversions themselves. I had been working with this kind of paradigm – make single measurements then combine them later – for a number of years, without conscious realization. Then, during Fall AGU 2006, I attended Goran Ekstrom's medal lecture, in which he presented his method for locating the long period energy from global earthquakes by reversing the dispersion of surface waves (Ekström, 2006). The method consists in reversing the dispersion starting from each point on a grid of possible locations in turn; the un-dispersed signals will only stack up on one of these points if an earthquake actually occurred there.

This essentially brute-force approach to the location problem was entirely based on the physical fact that information originating from a single source is necessarily coherent across a network of stations, if the waveform deformations due to source geometry and propagation are properly taken into account. I became fascinated with this concept, and rapidly developed my own version of Ekstrom's method for the Indian Ocean, with the idea of exploiting the Southern Indian Ocean and Antarctic stations, for which I have operational responsibility, to detect long-period signals from non-standard earthquakes occurring on the mid-ocean ridges (Maggi et al., 2007). Shortly afterwards, Alberto Michelini and I started developing a method to exploit the coherence of waveforms across the Italian national network to routinely locate local and regional earthquakes, using correlation with reference waveforms instead of de-propagation.

Development has been ongoing over the past three years, essentially as a spare time project (I have been busy with FLEXWIN and also with the International Polar Year work in Antarctica). We have presented the method at several conferences and have received enthusiastic feedback from the seismic monitoring community. The manuscript of our first WaveLoc publication, recently submitted to Geophysical Journal International, is reproduced as Chapter 3 of this habilitation thesis.

Chapter 2

FLEXWIN : automated selection of time windows

In this chapter I shall give an outline of FLEXWIN, my open source algorithm for the automated selection of time windows on pairs of observed and synthetic seismograms.

The algorithm was designed specifically to accommodate synthetic seismograms produced from 3D wavefield simulations, which capture complex phases that do not necessarily exist in 1D simulations or traditional traveltime curves. Relying on signal processing tools and several user-tuned parameters, the algorithm is able to include these new phases and to maximize the number of measurements made on each seismic record, while avoiding seismic noise. FLEXWIN can be used in iterative tomographic inversions, in which the synthetic seismograms change from one iteration to the next, and may allow for an increasing number of windows at each model iteration. Multiple frequency bands may also be used, allowing for more detail to be included into the tomographic model at each iteration, as the higher frequency synthetics gradually start to match the data. The algorithm is sufficiently flexible to be adapted to many tomographic applications and seismological scenarios, including those based on synthetics generated from 1D models.

FLEXWIN is described in more detail in Maggi et al. (2009), and in the manual available from `http://www.geodynamics.org`. The algorithm was used to perform an adjoint tomography inversion of Southern California (Tape et al., 2009, 2010). Some results from this inversion will be presented at the end of this chapter.

1 Introduction

Seismic tomography — the process of imaging the 3D structure of the Earth using seismic recordings — has been transformed by recent advances in methodology. Finite-frequency approaches are being used instead of ray-based techniques, and 3D reference models instead of 1D reference models. These transitions are motivated by a greater understanding of the volumetric sensitivity of seismic measurements (Marquering et al., 1999; Zhao et al., 2000; Dahlen et al., 2000) and by computational advances in the forward modelling of seismic wave propagation in fully 3D media (Komatitsch and Vilotte, 1998; Komatitsch et al., 2002; Capdeville et al., 2003). In the past decade we have learned to calculate analytic sensitivity kernels in 1D media (e.g. Li and Tanimoto, 1993; Dahlen and Baig, 2002; Dahlen and Zhou, 2006) and numeric sensitivity kernels in 3D media (e.g. Capdeville, 2005; Tromp et al., 2005; Zhao et al., 2005; Liu and Tromp, 2006, 2008). The analytic kernels have been taken up rapidly by tomographers, and used to produce new 3D Earth models (e.g. Montelli et al., 2004; Zhou et al., 2006). The numeric kernels have opened up the possibility of '3D-3D' tomography, i.e. seismic tomography based upon a 3D reference model, 3D numerical simulations of the seismic wavefield, and finite-frequency sensitivity kernels (Tromp et al., 2005; Chen et al., 2007).

It is common practice in tomography to work only with certain subsets of the available seismic data. The choices made in selecting these subsets are inextricably linked to the assumptions made in the tomographic method. For example, ray-based traveltime tomography deals only with high-frequency body-wave arrivals, while great-circle surface-wave tomography must satisfy the path-integral approximation, and only considers surface-waves that present no evidence of multipathing. In both these examples, a large proportion of the information contained within the seismograms is unused. The emerging 3D-3D tomographic methods take advantage of full wavefield simulations and numeric finite-frequency kernels, thereby reducing the data restrictions required when using approximate forward modelling and simplified descriptions of sensitivity. These methods seem to be the best candidates for studying regions with complex 3D structure, as they permit the use of a larger proportion of the information contained within each seismogram, including complex arrivals not predicted by 1D approximations of Earth structure. In order to exploit the full power of 3D-3D tomographic methods, we require a new data selection strategy that does not exclude such complex arrivals.

As data selection strategies for tomography depend so closely on the tomographic technique, there are nearly as many such strategies as there are tomographic methods. Furthermore, many of these strategies have been automated in some way, as larger and larger volumes of data have become available. Body-wave studies that have moved away from using manual traveltime picks or catalog arrival times generally pick windows around specific seismic phases defined by predicted traveltimes, and include automated tests on arrival time separation and/or the fit of observed to synthetic waveforms to reject inadequate data (e.g. Ritsema and van Heijst, 2002; Lawrence and Shearer, 2008). Partial automation of the VanDecar and Crosson (1990) multi-channel cross-correlation method has led to efficient methods for obtaining highly accurate traveltime (Sigloch and Nolet, 2006; Houser et al., 2008) and even attenuation (Lawrence et al., 2006) measurements. In the surface-wave community, there has been much work done to automate methods for extracting dispersion characteristics of fundamental mode (Trampert and Woodhouse, 1995; Laske and Masters, 1996; Ekström et al., 1997; Levshin and Ritzwoller, 2001) and higher mode (Van Heijst and Woodhouse, 1997; Debayle, 1999; Yoshizawa and Kennett, 2002; Beucler et al., 2003; Lebedev et al., 2005; Visser et al., 2007) surface-waves. Recently, Panning and Romanowicz (2006) have described an algorithm to semi-automatically pick body and surface-wavepackets based on the predicted traveltimes of several phases.

FLEXWIN is designed for tomographic applications with 3D Earth reference models. Unlike the techniques discussed above, it is not tied to arrival time predictions of known phases, and, therefore, is able to accommodate complex phases due to 3D structure. One promising approach to 3D-3D tomography is based upon adjoint methods (Tarantola, 1984; Tromp et al., 2005; Liu and Tromp, 2006; Tape et al., 2007). In “adjoint tomography” the sensitivity kernels that tie variations in Earth model parameters to variations in the misfit are obtained by interaction between the wavefield used to generate the synthetic seismograms (the direct wavefield) and an adjoint wavefield that obeys the same wave equation as the direct wavefield, but with a source term which is derived from the misfit measurements. The computational cost of such kernel computations for use in seismic tomography depends only on the number of events, and not on the number of receivers nor on the number of measurements. It is therefore to our advantage to make the greatest number of measurements on each seismogram. The adjoint kernel calculation procedure allows us to measure and use for tomographic inversion almost any part of the seismic signal. We do not need to identify specific seismic phases, as the kernel will take care of defining the relevant sensitivities. However, there is nothing in the adjoint method itself that prevents us from constructing an adjoint kernel from noise-dominated data, thereby polluting our inversion. An appropriate data selection strategy for adjoint tomography should therefore define measurement time windows that cover as much of a given seismogram as possible, whilst avoiding portions of the waveform that are dominated by noise.

From a signal processing point of view, the simplest way to avoid serious contamination by noise is to select and measure strong signals, which in seismology correspond to seismic arrivals. *Our strategy is therefore to select time windows on the synthetic seismogram within which the waveform contains a distinct energy arrival, then require an adequate correspondence between observed and synthetic waveforms within these windows.* This selection paradigm is general, and can be applied to synthetic seismograms regardless of how they have been obtained. It is clear, however, that a synthetic seismogram obtained by 3D propagation through a good 3D Earth model will provide a better fit to the observed seismogram over a greater proportion of its length than will be the case for a more approximate synthetic seismogram.

In order to isolate changes in amplitude or frequency content potentially associated with distinct energy arrivals, we need to analyze the character of the synthetic waveform itself. This analysis is similar to that used on observed waveforms in automated phase detection algorithms for the routine location of earthquakes. In designing our time-window selection algorithm, we have taken a tool used in this detection process — the short-term average / long-term average ratio — and applied it to the definition of time windows around distinct seismic phases.

The choices made in time-window selection for tomography are interconnected with all aspects of the tomographic inversion process, from the waveform simulation method (direct problem), through the choice of measurement method, to the method used to obtain sensitivity kernels, and the inversion method itself. One of the major difficulties in defining a general data selection strategy is the great range of possible choices open to the tomographer. We have designed a configurable data selection process that can be adapted to different tomographic scenarios by tuning a handful of parameters (see Table 2.1). Although we have designed our algorithm for use in adjoint tomography, its inherent flexibility should make it useful in many data-selection applications.

2 The selection algorithm

FLEXWIN operates on pairs of observed and synthetic single component seismograms. There is no restriction on the type of simulation used to generate the synthetics, though realistic Earth models and more complete propagation theories yield waveforms that are more similar to the observed seismograms, and thereby allow

Standard tuning parameters:	
$T_{0,1}$	bandpass filter corner periods
$r_{P,A}$	signal to noise ratios for whole waveform
$r_0(t)$	signal to noise ratios single windows
$w_E(t)$	water level on short-term:long-term ratio
$\mathrm{CC}_0(t)$	acceptance level for normalized cross-correlation
$\Delta\tau_0(t)$	acceptance level for time lag
$\Delta \ln A_0(t)$	acceptance level for amplitude ratio
$\Delta\tau_{\mathrm{ref}}$	reference time lag
$\Delta \ln A_{\mathrm{ref}}$	reference amplitude ratio
Fine tuning parameters:	
c_0	for rejection of internal minima
c_1	for rejection of short windows
c_2	for rejection of un-prominent windows
$c_{3a,b}$	for rejection of multiple distinct arrivals
$c_{4a,b}$	for curtailing of windows with emergent starts and/or codas
w_{CC} w_{len} w_{nwin}	for selection of best non-overlapping window combination

Table 2.1: Overview of FLEXWIN standard and fine tuning parameters. Values are defined in a parameter file, and the time dependence of those that depend on time is described by user-defined functions. (Maggi et al., 2009, Tab.1)

the definition of measurement windows covering more of the available data. The input seismograms can be measures of displacement, velocity, or acceleration, indifferently. There is no requirement for horizontal signals to be rotated into radial and transverse directions.

The window selection process has five stages, described in detail by Maggi et al. (2009): *Stage A:* pre-processing; *Stage B:* definition of preliminary measurement windows; *Stage C:* rejection of preliminary windows based on the content of the synthetic seismogram alone; *Stage D:* rejection of preliminary windows based on the differences between observed and synthetic seismograms; *Stage E:* resolution of preliminary window overlaps. The parameters that permit tuning of the window selection towards a specific tomographic scenario are all contained in a simple parameter file (see Table 2.1). More complexity and finer tuning can be obtained by making some of these parameters time-dependent via user defined functions that can depend on the source parameters (e.g. event location or depth).

2.1 Stage A

The purpose of Stage A is to pre-process input seismograms, to reject noisy observed seismograms records, and to set up a secondary waveform (the short-term average / long-term average ratio) derived from the envelope of the synthetic seismogram. This synthetic STA:LTA waveform will be used later to define preliminary measurement windows.

Minimal and identical pre-processing is applied to both observed and synthetic seismograms: removal of any linear trend, tapering, and bandpass filtering with a non-causal Butterworth filter, whose short and long period corners we denote by T_0 and T_1 respectively. Values of these corner periods should reflect the information content of the data, the quality of the Earth model, and the accuracy of the simulation used to generate the synthetic seismograms. All further references to "seismograms" will refer to these filtered waveforms. The next step is to reject observed seismograms that are dominated by noise.

The last step in this stage is the creation of the synthetic secondary waveform used to initiate the the window selection process. In order to correctly place windows around distinct energy arrivals in the seismograms, we need to detect these energy arrivals, a process not dissimilar to the detection of seismic phase arrivals routinely performed by automated earthquake location algorithms (e.g. Allen, 1982; Earle and Shearer, 1994b; Aster and Rowe, 2000; Bai and Kennett, 2000; Sleeman and van Eck, 2003). We have therefore taken a tool used in many implementations of the automated detection process — the short-term average long-term average ratio (e.g. Withers et al., 1998a; Bai and Kennett, 2001) — and adapted it to the task of defining time windows around seismic phases.

Given a synthetic seismogram $s(t)$, we derive a synthetic STA:LTA timeseries $E(t)$ using an iterative algorithm applied to the envelope of $s(t)$. If we denote the Hilbert transform of the synthetic seismogram by $\mathcal{H}[s(t)]$, its envelope $e(t)$ is given by

$$e(t) = |s(t) + i\mathcal{H}[s(t)]|. \tag{2.1}$$

The discretized short term average $S(t_i)$ and long term average $L(t_i)$ of $e(t_i)$ are calculated recursively

$$S(t_i) = C_S\ S(t_{i-1}) + e(t_i), \tag{2.2}$$

$$L(t_i) = C_L\ L(t_{i-1}) + e(t_i), \tag{2.3}$$

then combined to obtain $E(t_i) = S(t_i)/L(t_i)$. The constants C_S and C_L determine the decay of the relative weighting of earlier parts of the signal in the calculation of the current average. We set

$$C_S = 10^{-\Delta t/T_0} \qquad \text{and} \qquad C_L = 10^{-\Delta t/12T_0}, \tag{2.4}$$

where T_0 is the low-pass corner period of our bandpass filter (see for comparison Bai and Kennett, 2001).

An example of a synthetic seismogram and its $e(t)$ and $E(t)$ timeseries is shown in Figure 2.1. At each seismic arrival, $E(t)$ rises to a local maximum that corresponds both in position and in width to a seismic phase in the synthetic. The local minima in $E(t)$ correspond to the transitions between one phase and the next. In the following sections we shall explain how these correspondences are used to define time windows.

2.2 Stage B

The correspondence between local maxima in $E(t)$ and the position of the seismic phases in the synthetic seismogram suggests that we should center time windows around these local maxima. The correspondence between the local minima in $E(t)$ and the transition between successive phases suggests the time windows should start and end at these local minima. In the case of complex phases, there may be several local maxima and minima within a short time-span. In order to correctly window these complex phases, we must determine rules for deciding when adjacent local maxima should be part of a single window. From an algorithmic point of view, it is simpler to create all possible combinations of adjacent windows and subsequently reject the unacceptable ones, than to consider combining small, single-maximum windows into larger ones.

We start by defining a water level on $E(t)$ via the time-dependent parameter $w_E(t)$ in Table 2.1. All local maxima that lie above $w_E(t)$ are considered acceptable, and are used for the creation of candidate time windows. For the example in Figure 2.1, we have required the water level $w_E(t)$ to double after the end of the surface-wave arrivals (as defined by the epicentral distance and a group velocity of 3.2 km s^{-1}) so as to avoid creating time windows after $R1$.

We take each acceptable local maximum in turn as a seed maximum, and create all possible candidate windows that contain it. For N local maxima that lie above $w_E(t)$, the number of preliminary candidate windows defined in this manner is

$$N_{\text{win}} = \sum_{n=1}^{N} \left[nN - (n-1)^2 \right] \sim O(N^3). \tag{2.5}$$

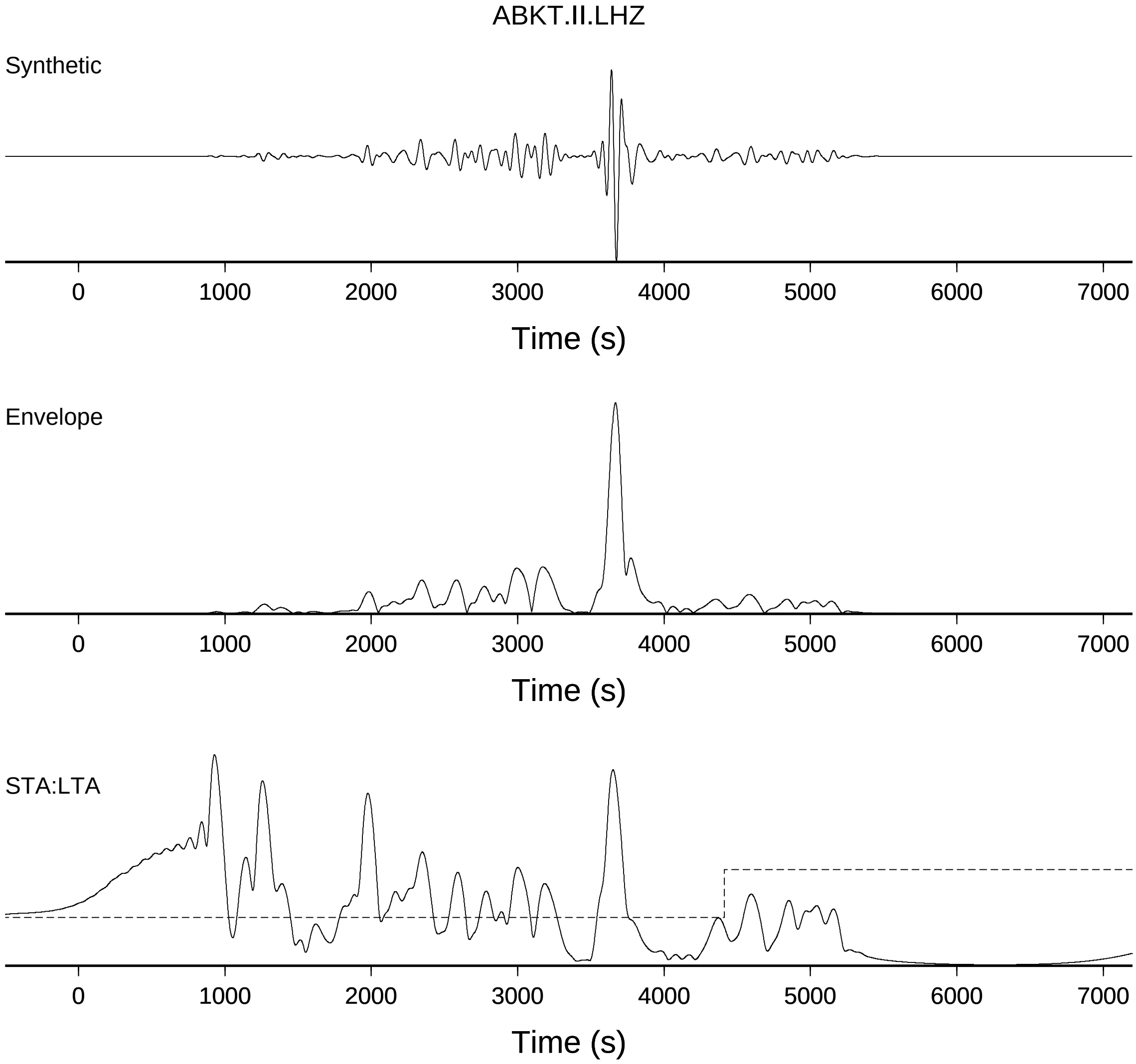

Figure 2.1: Synthetic seismogram and its corresponding envelope and STA:LTA timeseries. The seismogram was calculated using SPECFEM3D and the Earth model S20RTS (Ritsema et al., 2004) for the CMT catalog event 050295B. The station, ABKT, is at an epicentral distance of 14100 km and at an azimuth of 44 degrees from the event. The top panel shows the vertical component synthetic seismogram, filtered between periods of 50 and 150 seconds. The center panel shows its envelope, and the bottom panel shows the corresponding STA:LTA waveform. The dashed line overlaid on the STA:LTA waveform is the water level $w_E(t)$. (Maggi et al., 2009, Fig.1)

2.3 Stage C

After having created a complete set of candidate time windows in the manner described above, we start the rejection process. We reject windows based on two sets of criteria concerning respectively the shape of the STA:LTA waveform $E(t)$, and the similarity of the observed and synthetic waveforms $d(t)$ and $s(t)$ within each window. Here we describe the first set of criteria; the second set is described in the following section.

The aim of shape-based window rejection is to retain the set of candidate time windows within which the synthetic waveform $s(t)$ contains well-developed seismic phases or groups of phases. The four shape-based rejection criteria are parameterized by the constants c_{0-3} in Table 2.1, and are scaled in time by T_0 and in amplitude by $w_E(t)$. We apply these criteria sequentially. These criteria are described in detail in Maggi et al. (2009), and so are only briefly outlined here.

Firstly, we reject all windows that span deep local minima in $E(t)$, thereby forcing partitioning of unequivocally distinct seismic phases into separate time windows. Secondly, we reject short windows, thereby requiring that time windows be long enough to contain useful information. Thirdly, we reject windows whose seed maximum is not prominent, as subdued local maxima of this kind represent minor changes in waveform character, and should not be used to anchor time windows. Lastly, we reject windows that contain at least one strong phase arrival that is well separated in time from the time of the seed maximum. This criterion allows us to distinguish unseparable phase groups from distinct seismic phases.

The candidate windows that remain after application of these four rejection criteria are almost ready to be passed on to the next stage, in which we shall evaluate the similarity between observed and synthetic waveforms within the window limits. Special precautions may have to be taken, however, in the case of windows that contain long coda waves: the details of codas are often poorly matched by synthetic seismogram calculations, as they are essentially caused by multiple scattering processes. In order to avoid rejecting a nicely fitting phase because of a poorly fitting coda or a poorly fitting emergent start, we introduce the c_4 tuning parameters, which permit shortening of windows starting with monotonically increasing $E(t)$ or ending with monotonically decreasing $E(t)$.

Each successive criterion reduces the number of acceptable candidate windows. The upper portion of Figure 2.2 shows the results of shape-based window rejection applied to a real example.

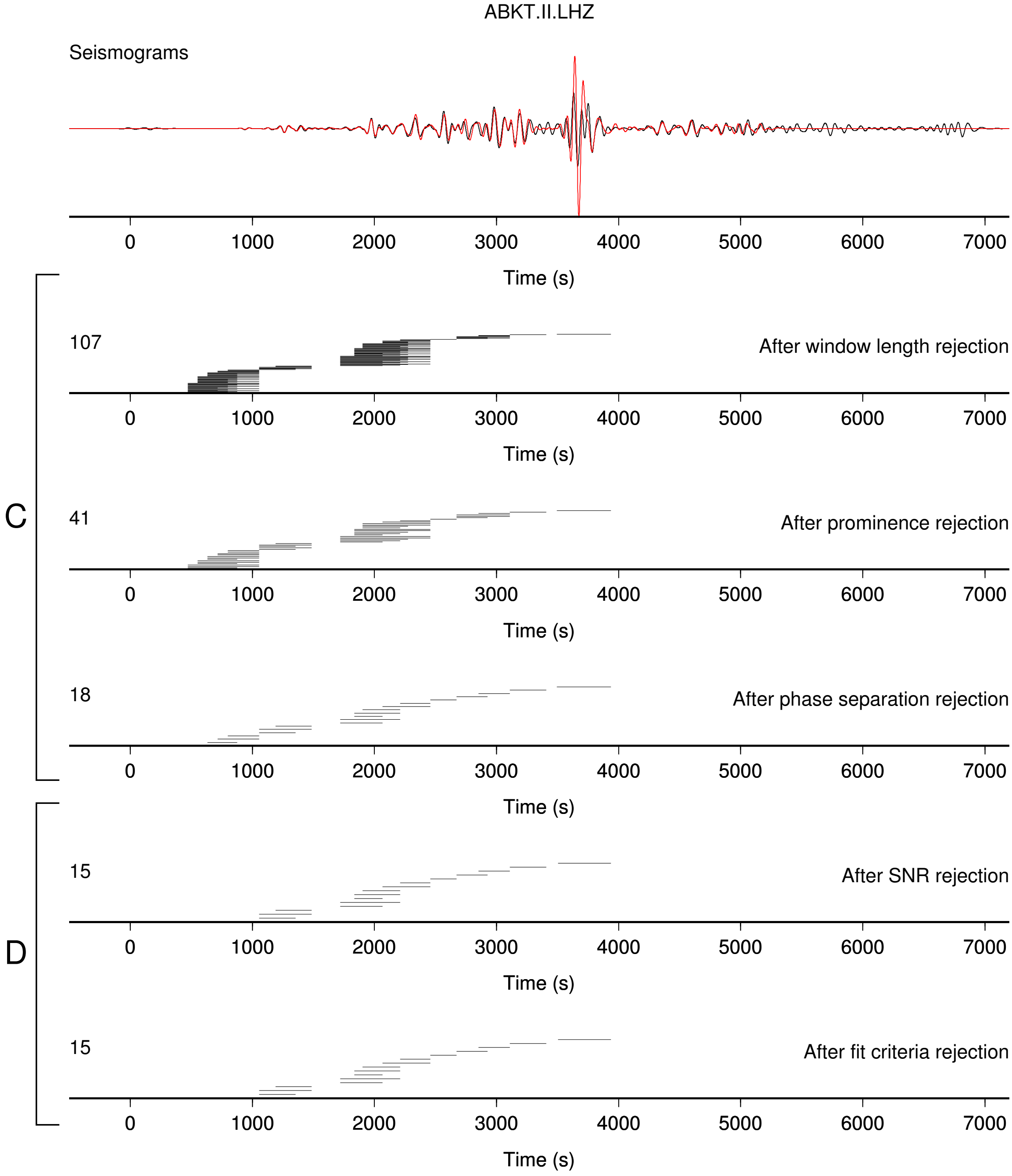

Figure 2.2: Window rejection applied to real data. Top panel: observed (black) and synthetic (red) seismograms for the 050295B event recorded at ABKT (see Figure 2.1). Subsequent panels: candidate windows at different stages, separated into Stage C (shape based rejection) and Stage D (fit based rejection). Each candidate window is indicated by a black segment. The number of windows at each stage is shown to the left of the panel. (Maggi et al., 2009, Fig.4)

2.4 Stage D

After having greatly reduced the number of candidate windows by rejection based on the shape of $E(t)$, we are now left with a set of windows that contain well-developed seismic phases or groups of phases on the synthetic seismogram. The next stage is to evaluate the degree of similarity between the observed and synthetic seismograms within these windows.

The quantities we use to define well-behavedness of data within a window are signal-to-noise ratio SNR_W, normalised cross-correlation value between observed and synthetic seismograms CC, cross-correlation time lag $\Delta\tau$, and amplitude ratio $\Delta \ln A$. The limits that trigger rejection of windows based on the values of these four quantities are the parameters $r_0(t)$, $\mathrm{CC}_0(t)$, $\Delta\tau_{\mathrm{ref}}$, $\Delta\tau_0(t)$, $\Delta \ln A_{\mathrm{ref}}$ and $\Delta \ln A_0(t)$ in Table 2.1. As for the STA:LTA water level $w_E(t)$ used above, the functional forms of the time-dependent parameters are defined by the user, and can depend on source and receiver parameters such as epicentral distance and earthquake depth. Figure 2.3 shows the time dependence of CC_0, $\Delta\tau_0$ and $\Delta \ln A_0$ for the example seismogram of Figure 2.2.

We only accept candidate windows that satisfy all of the following:

$$\mathrm{SNR}_W \geq r_0(t_M), \tag{2.6}$$

$$\mathrm{CC} \geq \mathrm{CC}_0(t_M), \tag{2.7}$$

$$\Delta\tau_{\mathrm{min}} \leq \Delta\tau \leq \Delta\tau_{\mathrm{max}}, \tag{2.8}$$

$$\Delta \ln A_{\mathrm{min}} \leq \Delta \ln A \leq \Delta \ln A_{\mathrm{max}}. \tag{2.9}$$

In words, we only accept windows in which the observed signal is sufficiently above the noise level, the observed and synthetic signals are reasonably similar in shape, their arrival time differences are small, and their amplitudes are broadly compatible.

When the synthetic and observed seismograms are similar, the fit-based criteria of equations (2.7)-(2.9) reject only a few of the candidate data windows (see lower portion of Figure 2.2). They are essential, however, in eliminating problems due secondary events (natural or man-made), diffuse noise sources, or instrumental glitches.

2.5 Stage E

After having rejected candidate data windows that fail any of the shape or similarity based criteria described above, we are left with a small number of windows, each of which taken singly would be an acceptable time window for measurement. As can be

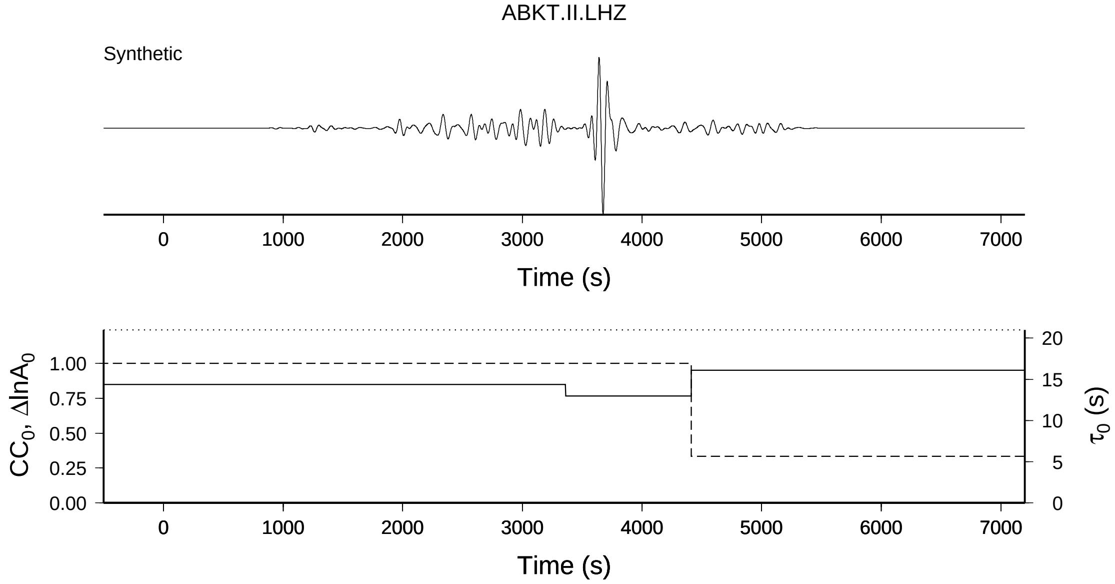

Figure 2.3: Time-dependent fit based criteria for the 050295B event recorded at ABKT. The lower limit on acceptable cross-correlation value, CC_0 (solid line), is lowered during the approximate surface-wave window, and is raised thereafter. The upper limit on time lag, τ_0 (dotted line), is constant for the whole seismogram. The upper limit on amplitude ratio, $\Delta \ln A_0$ (dashed line), is 1.0 for most of the seismogram; it is reduced to 1/3 of this value after the end of the surface-waves. (Maggi et al., 2009, Fig.5)

seen from the last panel of Figure 2.2, the remaining windows may overlap partially or totally with their neighbours. Such overlaps are problematic for automated measurement schemes, as they lead to multiple measurements of those features in the seismogram that lie within the overlapping portions. Resolving this overlap problem is the last step in the windowing process.

Overlap resolution can be seen as a set of choices leading to the determination of an optimal set of time windows. What do we mean by optimal? For our purposes, an optimal set of time windows contains only windows that have passed all previous tests, that do not overlap with other windows in the set, and that cover as much of the seismogram as possible. When choosing between candidate windows, we favor those within which the observed and synthetic seismograms are most similar (high values of CC). Furthermore, should we have the choice between two short windows and a longer, equally well-fitting one covering the same time-span, we may wish to favor the longer window as this poses a stronger constraint on the tomographic inversion.

The condition that optimal windows should have passed all previous tests removes the straightforward solution of merging overlapping windows. Indeed, given any two overlapping windows, we know that the window defined by their merger existed in the complete set of candidate windows obtained at the end of Stage B, and that its absence from the current set means it was rejected either because of the shape of its $E(t)$ time-series (Stage C), or because of an inadequate similarity between observed and synthetic waveforms (Stage D). It would therefore be meaningless to re-instate such a window at this stage. Any modification of current candidate windows would be disallowed by similar considerations. We must therefore choose between overlapping candidates.

We make this choice by constructing all possible non-overlapping subsets of candidate windows, and scoring each subset on three criteria: length of seismogram covered by the windows, average cross-correlation value for the windows, and total number of windows. These criteria often work against each other. For example, a long window may have a lower CC than two shorter ones, if the two short ones have different time lags $\Delta\tau$. Weighting of the three scores is necessary, and is controlled by the three parameters w_{CC}, w_{len} and w_{nwin} in Table 2.1.

Figure 2.4a shows an example of final windows selected on real data. For more examples of FLEXWIN at work on real data, see Maggi et al. (2009).

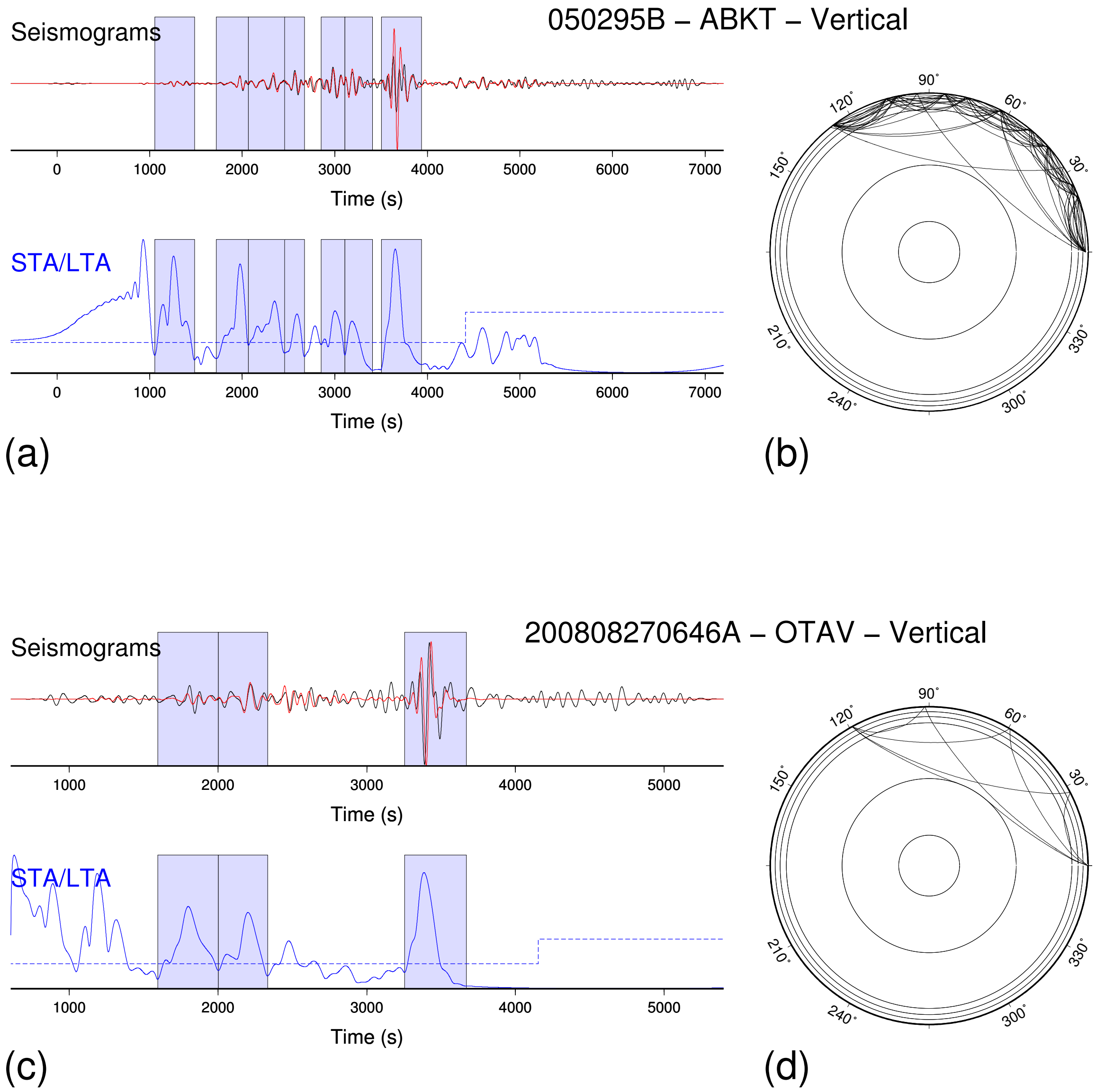

Figure 2.4: Window selection results for event 050295B recorded at ABKT (37.93°N, 58.11°E, $\Delta = 127°$, vertical component). (a) Top: observed and synthetic seismograms (black and red traces); bottom: STA:LTA timeseries $E(t)$. Windows chosen by the algorithm are shown using light blue shading. The phases contained these windows are: (1) PP, (2) $PS{+}SP$, (3) SS, (4) SSS, (5) $S5$, (6) $S6$, (7) fundamental mode Rayleigh wave. (b) Ray paths corresponding to the body-wave phases present in the data windows in (a). (c) Window selection results for event 200808270646A recorded at OTAV (0.24°N, 78.45°W, $\Delta = 119°$, vertical component). Phases contained within selected windows: (1) S_{diff} and $PS + SP$, (2) SS, (3) fundamental mode Rayleigh wave. (d) Ray paths corresponding to the body-wave phases present in the data windows in (c). (Maggi et al., 2009, Fig.7)

3 Using FLEXWIN for tomography

The window selection algorithm described in Maggi et al. (2009) was designed to solve the problem of automatically picking windows for tomographic problems in which phase separation and identification are not necessary: 3D-3D numerical tomography, of which the adjoint tomography proposed by Tromp et al. (2005) and Tape et al. (2007) is an example. For these problems, FLEXWIN provides a window-selection solution that is midway between full-waveform selection — which carries the risk of including high-noise portions of the waveform that would contaminate the tomography — and the selection of known phases or phase-groups based on *a priori* arrival times — which carries the risk of missing the information contained in the non-traditional phases produced by fully 3D structures.

FLEXWIN may also be used to select windows for tomographic problems in which separation of seismic arrivals is necessary and occurs naturally (under certain frequency and epicentral distance conditions) by virtue of differences in traveltimes. It can straightforwardly be adapted to studies of distinct body-wave phases (e.g. Ritsema and van Heijst, 2002), or to emulate the wavepacket selection of Panning and Romanowicz (2006), by modulating the $w_E(t)$ water-level using predicted phase arrival times, and selecting appropriate values for the signal-to-noise, cross-correlation and amplitude limits. The method can also be used to pre-select windows for studies of fundamental mode surface-waves (e.g. those based on the methods of Trampert and Woodhouse, 1995; Ekström et al., 1997; Levshin and Ritzwoller, 2001) by modulating $w_E(t)$ to exclude portions of the waveform that do not correspond to the correct group velocity window or epicentral distance range. Given the dispersed nature of surface-waves, synthetics produced by 1D starting models often are considerably different in shape from the data, so the CC and ΔT conditions (but not the signal-to-noise or $\Delta \ln A$ conditions) should relaxed in the window selection. These windows should then be passed on to specific algorithms used to extract the dispersion information. For this class of tomographic problems, the advantages of using FLEXWIN over manual or specifically designed automated windowing would be the encapsulation of the selection criteria entirely within the parameters of Table 2.1 (and their time-dependent modulation), leading to greater clarity and portability between studies using different inversion methods.

FLEXWIN is not intended for tomographic problems in which the extraction and separation of information from overlapping portions of a single timeseries is required, for example studies of higher-mode surface-wave dispersion for which specific methods have been developed: mode branch stripping (Van Heijst and Woodhouse, 1997), separation of secondary observables (Cara and Lévêque, 1987; Debayle, 1999), partitioned waveform and automated multimode inversion (Nolet, 1990; Lebedev et al., 2005), and non-linear direct search (Yoshizawa and Kennett, 2002; Visser et al., 2007).

3.1 Relevance to adjoint tomography

The full power of FLEXWIN can only be unleashed for problems — such as 3D-3D tomography — that do not require the separation (natural or otherwise) of seismic phases. The specificity of adjoint tomography, among the 3D-3D tomographic methods, is to calculate the sensitivity kernels by interaction between the wavefield used to generate the synthetic seismograms and an adjoint wavefield whose source term is derived from measurements of misfit between the synthetic and observed seismograms Tromp et al. (2005); Liu and Tromp (2006, 2008). The manner in which the adjoint sources are constructed is specific to each type of measurement (e.g. waveform difference, cross-correlation time lag, multi-taper phase and amplitude anomaly), but once formulated can be applied indifferently to any part of the seismogram. Adjoint methods have been used to calculate kernels of various body- and surface-wave phases with respect to isotropic elastic parameters and interface depths (Liu and Tromp, 2006, 2008), and with respect to anisotropic elastic parameters (Sieminski et al., 2007a,b). Adjoint methods allow us to calculate kernels for each and every wiggle on a given seismic record, thereby giving access to virtually all the information contained within.

It is becoming clear, as more finite-frequency tomography models are published, that better kernels on their own are not the answer to the problem of improving the resolution of tomographic studies. Trampert and Spetzler (2006) and Boschi et al. (2007) investigate the factors limiting the quality of finite-frequency tomography images, and conclude that incomplete and inhomogeneous data coverage limit in practice the improvement in resolution that accurate finite-frequency kernels can provide. The current frustration with the data-induced limitations to the improvements in wave-propagation theory is well summarized by Romanowicz (2008). The ability of adjoint methods to deal with all parts of the seismogram indifferently means we can incorporate more information from each seismogram into a tomographic problem, thereby improving data coverage.

The computational cost of constructing an adjoint kernel is independent of the number of time windows on each seismogram we choose to measure, and also of the number of records of a given event we choose to work with. It is therefore computationally advantageous to make measurements on as many records as possible for each event, while covering as much as possible of each record. There are, however, certain limits we must be aware of. As mentioned in the introduction, there is nothing in the adjoint method itself that prevents us from constructing a kernel from noise-dominated portions of the data. As the purpose of 3D-3D tomography is to improve the fine details of Earth models, it would be counterproductive to pollute the inversion process with such measurements and kernels. It is clear that the use of adjoint methods for tomography requires a strategy for selecting and windowing seismograms that avoids seismic noise while at the same time extracting as much information as possible from the signals.

The adjoint kernels are only strictly valid for the 3D Earth model they were constructed in, and therefore need to be re-computed at each iteration of the tomographic inversion (Tape et al., 2007). At each iteration, the similarities between the synthetic and observed seismograms improve, such that for later iterations a greater proportion of the waveform is adequate for measurement. In order to take advantage of this extra information, the windowing method used to isolate the portions of the waveform to be measured needs to be automated. The method must also be adaptable to the features that exist in the seismograms themselves, because 3D wavefield simulations are able to synthesize phases that do not exist in 1D simulations or traditional traveltime curves. All these considerations led us to favor a signal processing approach to the problem of data selection, an approach which in turn led to the development of the FLEXWIN algorithm we have presented here.

Finally, we note that the design of this algorithm is based on the desire *not* to use the entire timeseries of each event when making a measurement between data and synthetics. If one were to simply take the waveform difference between two timeseries, then there would be no need for selecting time windows of interest. However, this ideal approach (e.g., Gauthier et al., 1986) may only work in real applications if the statistical properties of the noise are well known, which is rare. Without an adequate description of the noise, it is more prudent to resort to the selection of time windows even when tomographic inversion is performed on waveform difference measurements.

3.2 An adjoint tomography example: Southern California

As an illustration of the application of FLEXWIN to adjoint tomography, I shall briefly present here some results from the Southern California adjoint tomography of Tape et al. (2009) and Tape et al. (2010). Carl Tape and I worked closely together on

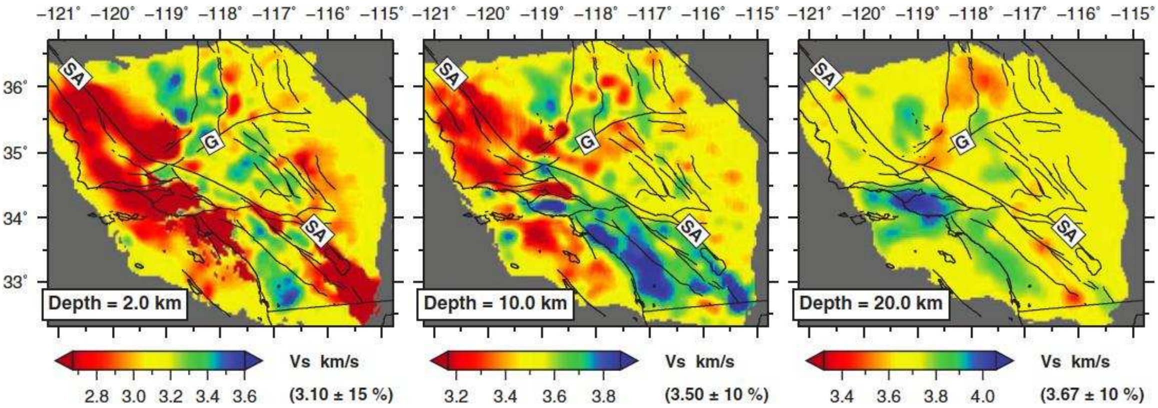

Figure 2.5: Horizontal cross sections of V_S tomographic model $\mathbf{m_{16}}$ at depths of 2, 10, and 20 km. Garlock (G) and San Andreas (SA) faults are labeled for reference. (Tape et al., 2009, Fig. 4)

fine tuning FLEXWIN and integrating it seamlessly into the tomographic process.

Tape et al. (2009) and Tape et al. (2010) iteratively improve a 3-D tomographic model of the southern California crust using numerical simulations of seismic wave propagation based on a spectral-element method (SEM) in combination with an adjoint method. The initial 3-D model is provided by the Southern California Earthquake Center. The data set comprises three-component seismic waveforms (i.e. both body and surface waves), filtered over the period range 2–30 s, from 143 local earthquakes recorded by a network of 203 stations. Time windows for measurements are automatically selected by the FLEXWIN algorithm Maggi et al. (2009). The misfit function in the tomographic inversion is based on frequency-dependent multitaper traveltime differences. The gradient of the misfit function and related finite-frequency sensitivity kernels for each earthquake are computed using an adjoint technique. The inversion involved 16 iterations, which required 6800 wavefield simulations.

The new crustal model, $\mathbf{m_{16}}$, is described in terms of independent shear (V_S) and bulk-sound (V_B) wave speed variations (Figure 2.5). It exhibits strong heterogeneity, including local changes of ±30% with respect to the initial 3-D model. The model reveals several features that relate to geological observations, such as sedimentary basins, exhumed batholiths, and contrasting lithologies across faults. The quality of the new model is validated by quantifying waveform misfits of full-length seismograms from 91 earthquakes that were not used in the tomographic inversion. The new model provides more accurate synthetic seismograms that will benefit seismic hazard assessment.

The objective is to fit the entire seismogram, wiggle for wiggle. This includes

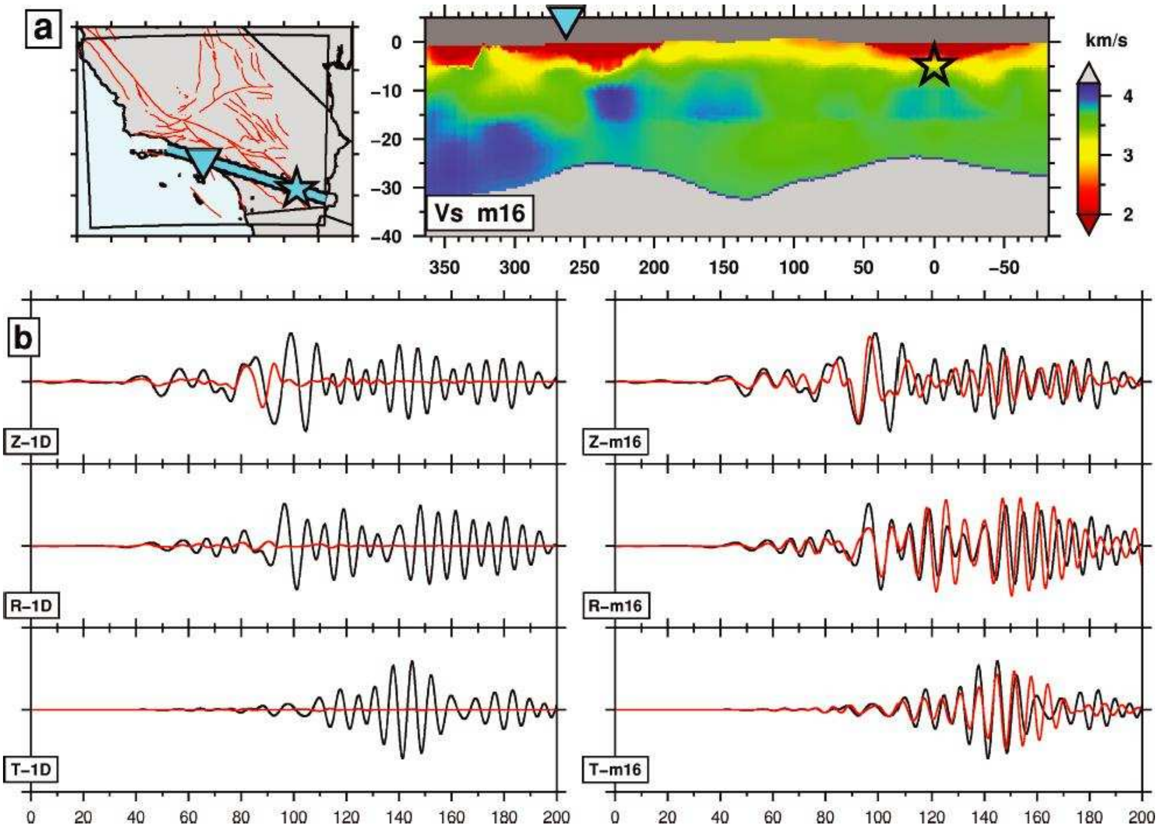

Figure 2.6: The influence of sedimentary basins on the seismic wavefield. (a) Cross-section of the final V_S crustal model $\mathbf{m_{16}}$, containing the path from an event beneath the Salton trough, to station LAF.CI within the Los Angeles basin. (b, left column) Data (black) and 1-D synthetics (red). (b, right column) Data (black) and 3-D synthetics for model $\mathbf{m_{16}}$ (red). The seismograms are bandpass filtered over the period range 6–30 s. Z, vertical component, R, radial component, T, transverse component. (Tape et al., 2010, Fig. 5)

body waves, surface waves and seismic waveforms that are not readily identifiable, such as the example shown in Figure 2.6. In this example the observed seismogram exhibits resonance from both the Salton trough (near the source) and the Los Angeles basin (near the station). The overall characteristics of the observed waveform are nicely captured by the 3-D model ($\mathbf{m_{16}}$) but are virtually absent using a standard 1-D model. This three-component seismogram, like hundreds in the data set, does not contain readily identifiable waveforms such as 'the P wave' or 'the Love wave'. Nevertheless, it is possible to fit such waveforms, as long as a measurement between the synthetic and observed seismograms can be made.

FLEXWIN was used to select time windows for measurement for all seismograms in the data set. There is a trade-off between the window-acceptance criteria of FLEXWIN and the amount of manual checking required. The authors chose to use liberal window-acceptance criteria, resulting in a maximal number of selected windows, including some that contained exotic waveforms such as laterally reflected surface waves, but requiring some manual checking to remove any undesirable measurements.

The selection of time windows was performed by FLEXWIN for each new set of synthetic seismograms for model $\mathbf{m_k}$ and for each of three sets of bandpasses (6–30 s, 3–30 s and 2–30 s). The total number of seismograms 'seen' by FLEXWIN in this study was approximately 3.08 million: 3 (different bandpasses) × 141 (average number of broad-band stations available) × 3 (components) × 143 (earthquakes) × 17 (models $\mathbf{m_{00}}$ to $\mathbf{m_{16}}$). Only an automated procedure such as FLEXWIN made it possible to manage such a large data set. Figure 2.7 shows an example of FLEXWIN–selected windows for an earthquake that was not used in the inversion, but was used for model validation.

4 Summary

The FLEXWIN algorithm was designed to automatically pick time windows for tomographic problems in which phase separation and identification are not necessary, however it can also be applied to problems in which phase separation is necessary and occurs naturally. It provides an automated window-selection solution that is midway between full-waveform selection and the selection of known phases or phase-groups based on *a priori* arrival times.

FLEXWIN has no *a priori* knowledge related to input model, geographic scale or frequency range. It is a configurable process that can be applied to different seismic scenarios by changing the handful of parameters in Table 2.1. The configuration

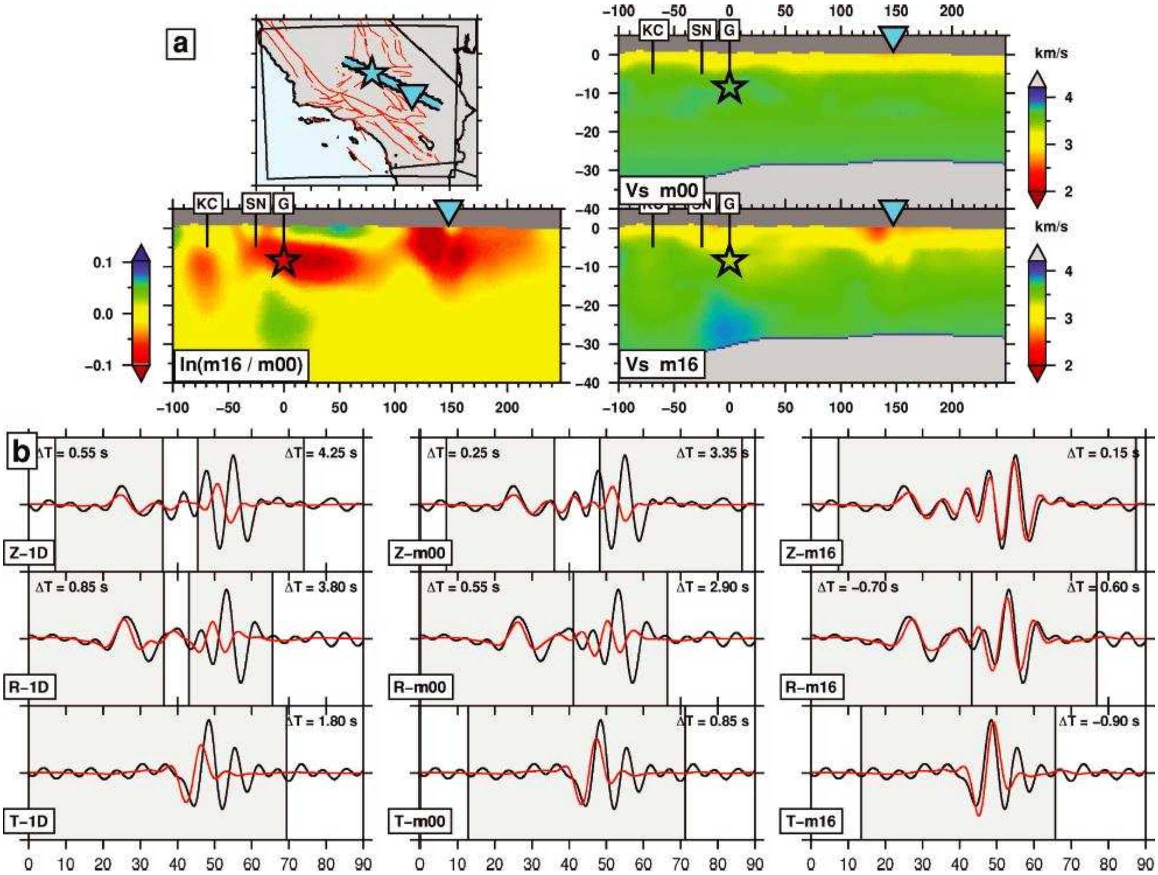

Figure 2.7: Vertical cross-sections and corresponding three-component seismograms. (a) Cross-section of the V_S tomographic models for a path from an event on the Garlock fault, to station HEC.CI in the eastern Mojave Desert. Upper right panel is the initial 3-D model, $\mathbf{m_{00}}$, lower right panel is the final 3-D model, $\mathbf{m_{16}}$, and lower left panel is the difference between the two, $\ln(\mathbf{m_{16}}/\mathbf{m_{00}})$. KC, Kern Canyon fault; SN, Sierra Nevada fault; G, Garlock fault. (b) Synthetic seismograms (red) and observed seismograms (black) for the period range 6–30 s. The left column shows synthetics computed using a 1-D model for southern California. The centre column shows synthetics computed using the initial 3-D model $\mathbf{m_{00}}$. The right column shows synthetics computed using the final 3-D model $\mathbf{m_{16}}$. Z, vertical component, R, radial component, T, transverse component. In this example, the highlighted time windows are automatically selected for measurement using the FLEXWIN algorithm. This earthquake was not used in the tomographic inversion. (Tape et al., 2010, Fig.9)

process is data-driven: starting from the description of how each parameter influences the window selection (Section 2 and MANUAL), the user tunes the parameters using a representative subset of the full dataset until the algorithm produces an adequate set of windows, then applies the tuned algorithm to the full dataset. The choice of what makes an adequate set of windows remains subjective, as it depends strongly on the quality of the input model, the quality of the data, and the region of the Earth the tomographic inversion aims to constrain. We consider the algorithm to be correctly tuned when false positives (windows around undesirable features of the seismogram) are minimized, and true positives (window around desirable features) are maximized. For a given dataset, the set of tuned parameters (Table 2.1) and their user-defined time dependencies completely determine the window selection results, which are therefore entirely reproducible.

The desire to study regions with strong 3D variations in Earth structure requires seismologists to deal with increasingly complex seismic records, and to use methods that take advantage of full wavefield simulations. Only by using all available information will tomographic inversions produce more accurate and higher resolution images of the Earth's interior. A window selection method such as FLEXWIN is necessary in order to fully unleash the potential of recent tomographic methods – and specifically of adjoint tomography – to exploit information from all parts of the waveform.

FLEXWIN is available as an open-source package through CIG (Computational Infrastructure for Geodynamics, `http://www.geodynamics.org`).

Chapter 3

WaveLoc : Continuous waveform event detection and location

We present WaveLoc, an earthquake detection and location technique that does not rely on wave onset phase picking and on event phase association, but uses continuous stream-like correlation between processed waveform data and a set of reference waveforms. At each time step, earthquake occurrence is tested through the sum of the correlation values on a set of potential location points. Our technique generalizes and further develops the LWCEDS methodology introduced by Withers et al. (1999). We have applied WaveLoc to the $M_w6.1$, April 6, 2009, L'Aquila earthquake sequence, and detect nearly 13,500 events, of which over 7000 can be associated with the ISIDE catalog of events manually detected and located at the INGV seismic monitoring center. WaveLoc detected over 85% of $M_L2.5-3.5$ events listed by ISIDE, and missed only one of the 50 $M_L > 3.5$ events (98% detection rate). Development of the WaveLoc methodology is ongoing, and it can be adapted to both real-time domains (seismic monitoring) and data-mining (the analysis of large volumes of data without human intervention).

1 Introduction

The ever increasing volume of continuous digital waveform data collected at data centers, available both in real-time and off-line, requires the development of automatic and robust procedures for the identification of a variety of seismic phenomena, ranging from regular earthquakes (e.g., Rowe et al., 2002) to the recently discovered slow earthquakes and non-volcanic tremor episodes (e.g., Obara, 2002; Rogers and Dragert, 2003; Ide et al., 2007). Detecting all these phenomena, often hidden in the background noise or occurring within short time lapses in the immediate minutes after a large earthquake, requires the development of techniques that exploit the coherency of phases or of signal patterns among stations (e.g., Kao and Shan, 2004; Baker et al., 2005; Brown et al., 2008; Wech and Creager, 2008; Naoki Suda and Ryoko Nakata and Takehiro Kusumi, 2009).

Traditional earthquake location is performed using phase arrivals and event association (e.g., Lee and Stewart, 1981). Extraction of phase arrivals from waveform data greatly reduces the volume of information processed during the location process (e.g., Withers et al., 1998b), but requires the introduction of complex logic in order to associate each arrival to a single event. After a large main shock (e.g., $M \geq 6$), a cascade of earthquakes abruptly inundates the acquisition/detection system, and has been long known to cause standard procedures based on phase picks and event association to fail, because of the occurrence of multiple, near-simultaneous events in different parts of the aftershock zone (e.g., Johnson et al., 1994). As a result, many of these events may be either falsely associated and mis-located, or missed altogether. It is thus of importance to develop and implement techniques capable of exploiting fully and automatically more of the information contained in the recorded waveforms (e.g., Young et al., 1996). The automation of procedures becomes especially important when a large number of data streams are available. Given the speed of current CPUs, analyses that take into account complete waveform data streams have now become feasible.

During the past two decades a number of studies have been published on the use of full waveforms to locate earthquakes both at global and regional/local scales. All these techniques rely on phase coherency through back projection and reverse time migration. Early work on the global scale was carried out by Shearer (1994) through waveform match filtering, and adopting a grid representing potential event locations. Young et al. (1996) further developed the grid technique and proposed the Waveform Correlation Event Detection System, WCEDS. More recently, a detection approach based on waveform deconvolution was developed by Ekström (2006) to identify sources lacking in body-waves, an approach that led Ekstrom et al. (2003) to detect anomalous seismic sources such as glacial earthquakes. On regional/local scale, a similar methodology was first proposed by Withers et al. (1999), who pursued the correlation technique of Young et al. (1996) and developed the Local Waveform Correlation Event Detection System, LWCEDS. Along the same ideas and more recently, Kao and Shan (2004) proposed the Source-Scanning Algorithm, SSA, and Baker et al. (2005) proposed the Real-time Kirchhoff Location, RKL, method. The latter two techniques, however, appear less flexible and general than that introduced by Withers et al. (1999). LWCEDS relies on the cross-correlation between processed data and pre-computed reference waveforms, RWs, before stacking, whereas both SSA and RKL migrate the recorded amplitudes using traveltimes. Time reverse migration is another approach toward back projection, and initial developments were made by McMechan et al. (1985). Rietbrock and Scherbaum (1994) and, more recently, Gajewski and Tessmer (2005) and Larmat et al. (2006) also adopted the same basic idea.

Central to all these methodologies is phase coherency, required in order to reverse time migrate (back project) the recorded energy back to discontinuities (e.g. Claerbout, 1971) or, as in our case, to the location of the seismic source for single event (Withers et al., 1999; Kao and Shan, 2004; Baker et al., 2005), or to the location of prominent seismic energy radiation zones during rupture of M>6 earthquakes (e.g. Ishii et al., 2005; Walters et al., 2005; Kao and Shan, 2007; Allmann and Shearer, 2007)

Implementation of correlation approaches such as LWCEDS requires a constant volume of computation (e.g., Baker et al., 2005), regardless of the number of event detections, and contains no complex logic. The inherent simplicity of such a system, and its apparent lack of optimization, make it robust and stable, even during an energetic aftershock sequence, a feature that is highly desirable for seismic monitoring centers.

Finally, it is interesting to note that the location techniques adopted by most methodologies mentioned above are closely related to the method of circles, first introduced by Milne (1886). Other well-known descendants of the method of circles are the strip method described by Richter (1958), and the phase associator used by Earthworm Johnson et al. (1995, 1994).

In this paper, we shall describe a re-adaptation of the Withers et al. (1999) LWCEDS technique, which we have called WaveLoc (WL). We have applied WaveLoc to the recent $M_w = 6.3$ (6.1 according to a more recent study by Scognamiglio et al., 2010, and this estimate will be used hereafter), April 6, 2009, L'Aquila earthquake sequence (Chiarabba et al., 2009), and we shall quantify its performance by statistical comparison with the bulletin produced for this sequence by the INGV seismic monitoring center.

2 Method

The LWCEDS algorithm, developed and described in detail by Withers et al. (1999), was based on earlier work by Young et al. (1996). In the following we provide a comprehensive description of the methodology, focusing in particular on the novelties we have introduced in developing WaveLoc.

An illustration of the basic procedure is shown in Fig. 3.1. Consider a simplified acquisition geometry (Fig. 3.1a), consisting of three stations (S1, S2 and S3), the true seismic source location (indicated by a star), and two potential seismic source locations (G1 and G2). Consider also that the waveforms for the three stations have been processed to enhance their first arrivals, using short-term/long-term averages (STA/LTA) for example. For location G1, close to the true source location, the processed waveforms align correctly with theoretical travel-time curves (Fig. 3.1b), while this is not the case for location G2 (Fig. 3.1c). Location G1 should therefore be preferred over G2. The LWCEDS algorithm correlates processed observed waveforms with reference waveforms constructed directly from travel-time curves, and compares the amplitude of this correlation for all possible source locations. This approach can be considered a brute-force implementation of the Richter (1958) strip method: instead of using the correspondence of observed and theoretical arrival times to derive an epicentral distance, this approach iterates through all possible epicentral distances and rejects those that do not correspond.

In order to determine the locations and origin times of earthquakes, the algorithm calculates the following time-dependent stack:

$$S_j(t) = \frac{1}{N} \sum_{i=1}^{N} \mathbf{u}_i(t) \cdot \mathbf{g}_{ij}, \tag{3.1}$$

where $\mathbf{u}_i(t)$ $(i = 1, 2, \ldots, N)$ indicates the processed waveform recorded at the i^{th} station and starting at time t, and $\mathbf{g}_{ij}$ indicates the corresponding reference waveform for propagation between the i^{th} station and the j^{th} potential source location from a set of points $\mathbf{x}_j$ $(j = 1, 2, \ldots, M)$. The observed and reference waveforms have the same length Δt, and the reference waveforms $\mathbf{g}$ are adapted to the processing applied to $\mathbf{u}(t)$. For each t, the algorithm determines the maximum

$$S_{max}(t) = \max\{S_j(t), j = 1, 2, \ldots, M\}, \tag{3.2}$$

and infers that a seismic source has occurred at time t and location $\mathbf{x}_j$ when the value of $S_{max}(t)$ is a local maximum larger than a pre-defined threshold (Withers et al., 1999).

In developing WaveLoc, we have generalized the basic LWCEDS method: we use continuous data streams, allow the reference waveforms $\mathbf{g}_{ij}$ to be path-specific, and allow the set of potential source locations $\mathbf{x}_j$ to be irregular. We also allow for the use of a combination of waveform processing methods, each tailored to enhancing a

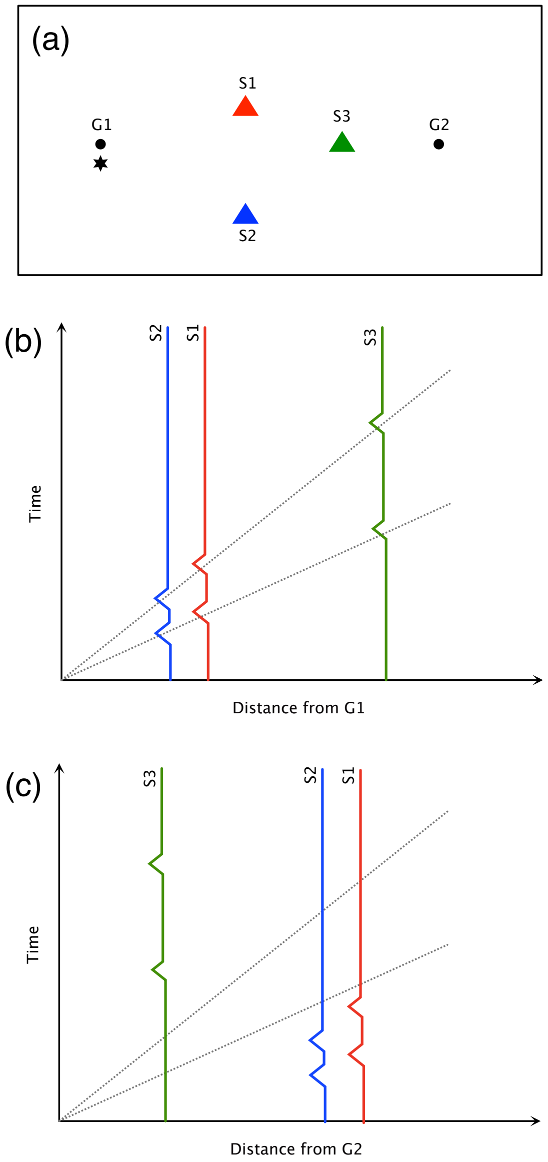

Figure 3.1: Cartoon of the basic procedure common to LWCEDS (Withers et al., 1999) and WaveLoc. (a) A simple acquisition geometry: an event occurs at the point indicated by the black star, and is recorded at stations S1, S2 and S3. Two potential event locations are indicated by G1 and G2. (b) Record section of simplified recorded seismograms with respect to potential location G1 : *P* and *S* arrivals align correctly with predicted travel-time curves. (b) Record section with respect to potential location G2 : *P* and *S* arrivals no longer align correctly with the travel-time curves.

particular feature of the observed seismogram, and each accompanied by a specific set of reference waveforms. Under this generalization, equation (3.1) becomes

$$S_j(t) = \frac{1}{N \times K} \sum_{k=1}^{K} \sum_{i=1}^{N} \mathbf{u}_{ik}(t) \cdot \mathbf{g}_{ikj} \tag{3.3}$$

where $(k = 1, 2, \ldots, K)$ indicates the type of processing adopted. With this generalization, WaveLoc can be used to identify many different phenomena or combinations of phenomena.

In implementing methods based on correlation between observed and reference signals, it is important to choose the processing applied to the signals according to the information we wish to extract. For the problem we are addressing in this paper, seismic source detection and location, we wish to determine a simple, 4-parameter quantity: a 3-D geographical point and an origin time corresponding to the space and time location of the event. As this quantity is related to the timing of the seismic phases in the waveform, we extract the timing information by applying signal processing to enhance the P-wave onsets (we use a 15 s kurtosis filter, see Section 2.1), and use reference waveforms that consist of simple P-wave travel-time envelopes. Clearly, for problems in which more complex quantities are sought, more complete reference waveforms and different types of data processing may be used (see e.g., Auger et al., 2006; Tsuruoka et al., 2009, for moment tensor determination using stream data).

2.1 WaveLoc in a laterally homogenous Earth : a method of circles

For a one-dimensional, laterally homogeneous Earth, a single set of azimuth-independent reference waveforms contains all the timing information required for the detection and location problem (Withers et al., 1999). For a three-dimensional, laterally heterogeneous Earth, reference waveforms for all combinations of potential source locations and recording stations should in principle be calculated and stored. In this paper we limit our discussion to the 1D case (Earth structure only depends on depth), in which the azimuth-independence of the reference waveforms leads to a significant reduction in computing cost. Implementation of the 3D case would produce improved locations, though at greater computing cost, and only if sufficiently accurate reference waveforms could be calculated from knowledge of the regional velocity structure, or if they were derived from pre-recorded observed waveforms (empirical reference waveforms). As we shall apply the technique to the l'Aquila sequence, which occurred entirely within the upper crust, we shall further simplify the presentation of the method by considering a fixed depth for the seismic sources.

We have stated above that earthquake location performed using cross-correlation techniques like LWCEDS and WaveLoc is related to the method of circles (Milne, 1886) and to the strip method (Richter, 1958). In order to understand the similarities between these methods, it is instructive to observe what happens in WaveLoc when an earthquake occurs (see Fig. 3.2). Visualize a set of continuous, real-time data streams, in which newer points appear on the right (colored waveforms in Fig. 3.2). Shortly after an earthquake occurs, the nearest station starts recording it. The signal from the earthquake appears to the right of the data stream, so the stream correlates well only with the reference waveform corresponding to the farthest distance. The corresponding time-slice in map view contains a circular band of higher correlation values at that distance from the nearest station (Fig. 3.2a). As time proceeds, the signal moves towards the left on the data stream, so the stream correlates well with reference waveforms corresponding to closer distances. In the corresponding time-slices, the circular band decreases in size, and collapses towards the location of the station. As more stations record the earthquake, more collapsing circular bands appear in the time-slices (Fig. 3.2b). When the procedure steps through to the time-slice corresponding to the origin time, i.e., when the reference waveforms are aligned with the data for each station, all the circular bands intersect at a point corresponding to the epicenter (Fig. 3.2c). The circular bands then continue collapsing onto the station locations (Fig. 3.2d). Simple geometrical considerations imply that, for real-time operation, the time required to locate an earthquake will depend on its distance from the nearest station and on the length of the most distant reference waveform. In this study we have used 50 s long reference waveforms containing only P wave onset times, and stations within ∼100 km of the epicentral area for the l'Aquila main-shock. Under these conditions, earthquake detection and location can be obtained within 20 s of the origin time.

2.2 Data processing

Data processing is a fundamental step in the design and implementation of correlation-based techniques. The types of analyses that can be carried out using these methods depend on the features in the waveforms that are singled out by the data processing. Given today's numerical techniques, such as spectral element methods for full wave-field propagation in complex 3D media (e.g. Komatitsch and Tromp, 2002a,b), we could in principle calculate full reference waveforms for any phenomenon for which

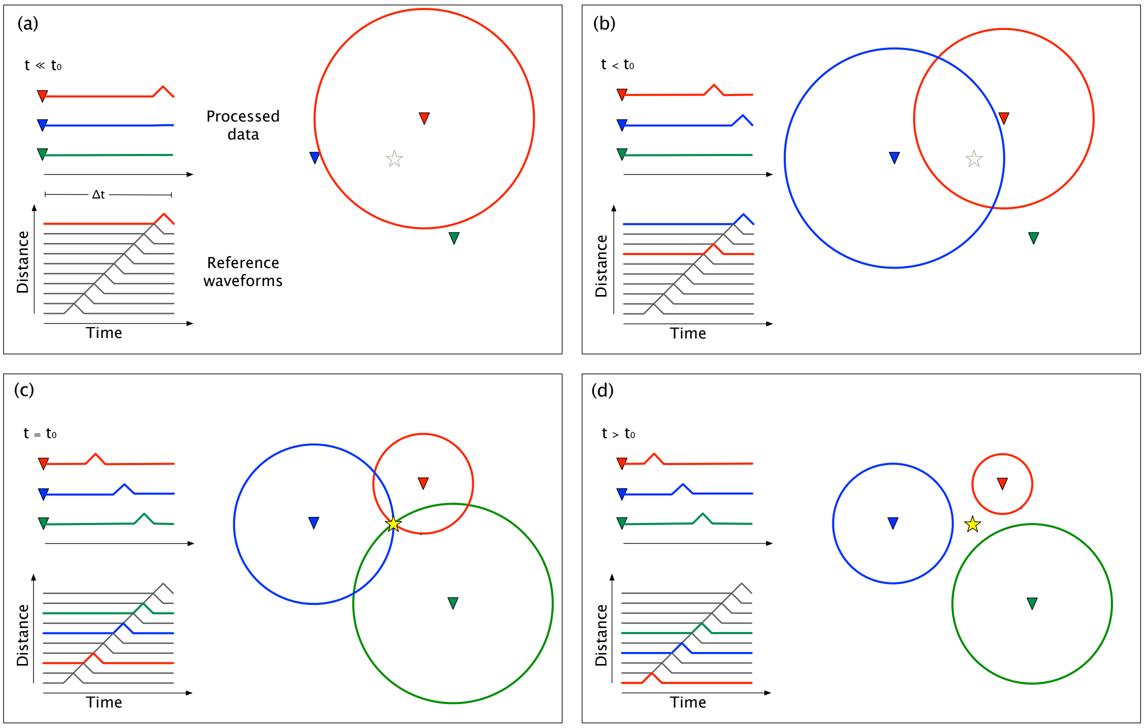

Figure 3.2: Visualization of the correlation-based event detection process. The four panels represent the state of the system at increasing times. Seismic stations are indicated by inverted triangles on the right-hand portion of each panel. Streams of processed waveform data from each of these stations are plotted in color at the top left of each panel, and a set of reference waveforms for increasing epicentral distances is plotted below them. All waveforms are of length Δt. An event occurs at time t_0 at the location indicated by the star. Time t refers to the first point of the data streams; the latest point is at time $t + \Delta t$. (a) $t \ll t_0$: The event has occurred, and the nearest station has just recorded the corresponding P-wave. The stream correlates with the furthest reference waveform, and creates a circular band around the nearest station. (b) $t < t_0$: The second station records the event. A new circular band forms around the second station, while that corresponding to the first data stream collapses towards its station. (c) $t = t_0$: All three stations have recorded the event. The corresponding circular bands intersect at the event location. (d) $t > t_0$: The circular bands continue to collapse towards their corresponding stations.

the source physics and the propagating medium is sufficiently well understood. Processing would still be required, however, to enhance the signal-to-noise ratio of the features corresponding to the phenomenon in the observed data.

The choice of reference waveform and that of the data processing are both inextricably linked to the phenomenon we are trying to isolate. For the earthquake location problem, the information we require is encapsulated in the phase arrival-times, so it follows that we should select the reference waveforms and the data pre-processing most likely to enhance these arrival-times. The enhancement of arrival-times is a fundamental part of most automated wave-onset picking algorithms, and the most commonly used enhancement method is based on the comparison between the short term (STA) and long term average (LTA) of the signal (e.g. Allen, 1987; McEvilly and Majer, 1982; Earle and Shearer, 1994a, among many others).

Withers et al. (1999) choose an implementation of the STA/LTA method as their data-processing method. We have experimented with a number of other processing methods within WaveLoc, including computing the kurtosis (fourth moment) of the data within fixed-length sliding windows along the observed seismogram,

$$\mathrm{Kurt}(x_1, \ldots, x_n) = \left\{ \frac{1}{N} \sum_{j=1}^{N} \left[\frac{x_j - \bar{x}}{\sigma} \right]^4 \right\} - 3, \tag{3.4}$$

where N is the number of samples within each window, and $\sigma = \sigma(x_1, \ldots, x_n)$ is their standard deviation. Such higher statistical moments have only recently started to be used in automated arrival-time picking algorithms (e.g. Saragiotis et al., 2002; Gentili and Michelini, 2006; Kuperkoch et al., 2010; Nippress et al., 2010). The output time-series obtained by these different processing methods depends on the choice of window length. Two window lengths are required for the STA/LTA method, one for the short-term and one for the long-term average, while only one window length is required for the kurtosis method. In Fig. 3.3, we compare time-series obtained by running STA/LTA and kurtosis processing, with different window lengths, on the same observed data. We find that kurtosis generally produces sharper onset peaks than STA/LTA, which is an advantage for arrival-time picking. The choice of kurtosis window length Δt_k is a trade-off between sensitivity to small amplitude variations, which requires shorter windows (the kurtosis is incapable of distinguishing two arrivals occurring within Δt_k of each other), and robustness, which requires longer windows (Fig. 3.3b). After considerable testing, we have chosen to use kurtosis processing with a $\Delta t_k = 15$ s time-window in our application.

Fig. 3.4 shows the result of kurtosis processing applied a typical 35-minute span

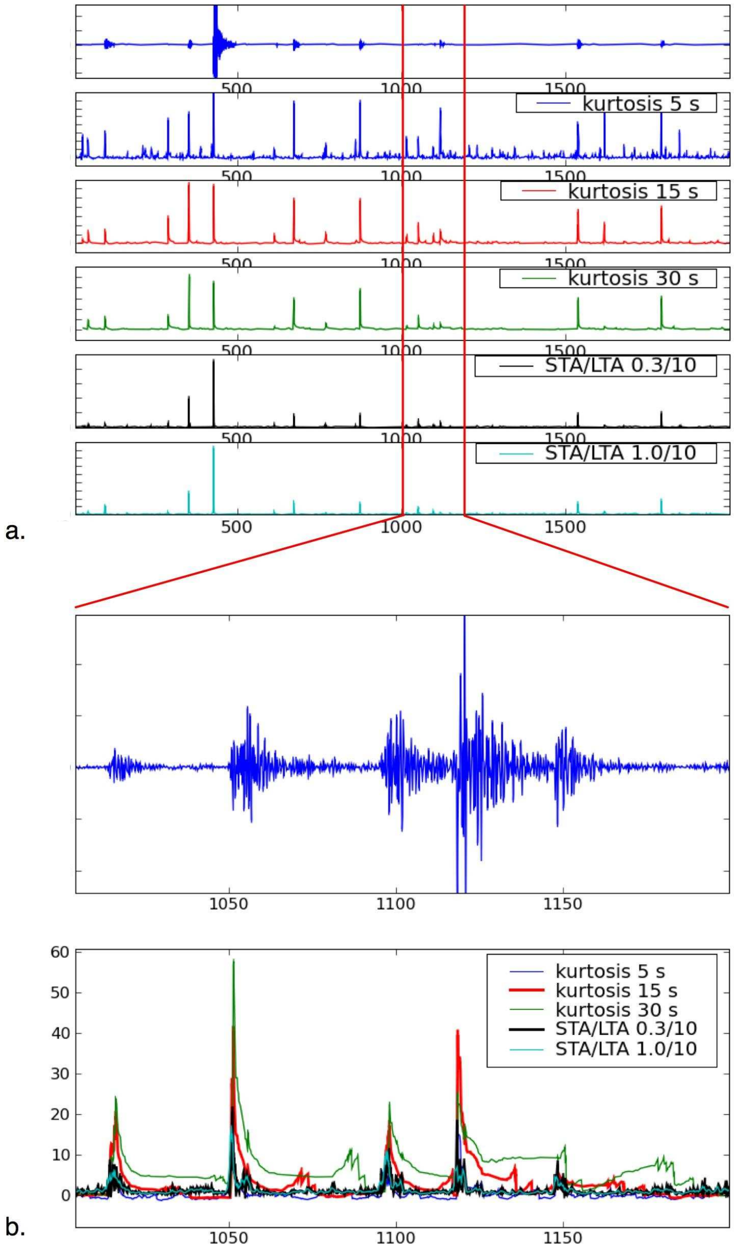

Figure 3.3: Example of waveform processing of a 35' window. (a) from top to bottom: recorded waveform, kurtosis and STA/LTA pre-processing (see figure legends for detail); (b) 200 s blown-up of the central part of the data window with original seismogram (top) and the pre-processings in (a) plotted on the same panel.

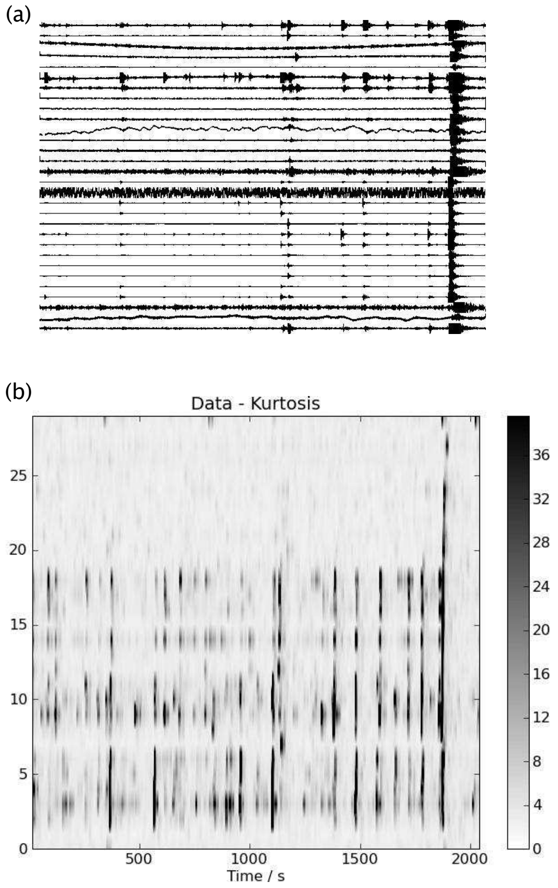

Figure 3.4: Phase arrival coherence enhanced by kurtosis processing. (a) High frequency, vertical component raw waveforms from the L'Aquila earthquake sequence (a 35-minute span starting April 9th at 09:00 GMT). Data have been de-trended, and amplitude-limited in order to increase visibility of the smaller events, for ease of plotting only. No particular ordering of the waveforms has been performed. (b) Summary image of the kurtosis-processed waveforms. Each horizontal band corresponds to a single station, and stations are ordered loosely by the time of the first maximum in the processed data. Amplitude of kurtosis is indicated by the grayscale. The coherence of phase arrivals is visibly enhanced compared with that of the raw data in (a).

of local and near-regional data from the l'Aquila sequence. The coherence of phase arrivals across the network, already visible in the raw data (Fig. 3.4a), is considerably enhanced after kurtosis processing (Fig. 3.4b).

2.3 The WaveLoc computational approach

The computational approach used by WaveLoc for the 1D case is conceptually similar to that used by LWCEDS (cf. Withers et al., 1999). The 1D-Earth and fixed-depth assumptions allow us to consider a reduced set of reference waveforms $\mathbf{g}_l$ ($l = 1, 2, \ldots, N_g$), at a range of epicentral distances, each of length Δt. We analyze processed observed waveforms $\mathbf{u}_i(t)$ of length $\Delta T \gg \Delta t$ from N stations. For each point in the set of M potential source locations $\mathbf{x}_j$, we find the reference waveform $\mathbf{g}_l$ corresponding to the distance to nearby seismic stations, and store the corresponding $(i, l)_j$ triplets (there are at most N triplets for each j). We calculate the cross-correlation of each observed waveform $\mathbf{u}_i(t)$ with each reference waveform $\mathbf{g}_l$, to form $C_{il}(t)$, in which each element is a cross-correlogram of length $\Delta T - \Delta t$. For each $\mathbf{x}_j$, we stack the elements C_{il} that correspond to the precomputed $(i, l)_j$ triplets :

$$S_j(t) = \frac{1}{N} \sum \mathbf{C}_{il}(t), \forall (i, l)_j. \tag{3.5}$$

This 1D approach requires at most the computation of $N \times N_g$ cross-correlations, while the corresponding 3D approach would require $N \times M$ cross-correlations. For a typical region, $N_g \ll M$, leading to a significant reduction in computing cost if the detection/location can be carried out in 1D. The resulting set of stacked cross-correlograms $S_j(t)$ can be sliced in time to give maps of correlation (Fig. 3.5a), to which we apply equation (3.2) to obtain the maximum-correlation time-series $S_{max}(t)$ (Fig. 3.5b).

2.4 The WaveLoc event detector / locator

The WaveLoc event detector operates on the maximum-correlation time-series $S_{max}(t)$. Prominent local maxima in $S_{max}(t)$ correspond to seismic events, as can be seen by comparing typical data recorded at station AQU (L'Aquila) with the corresponding maximum-correlation time-series (Fig. 3.6a,b). The amplitudes of the local maxima of $S_{max}(t)$ scale approximately with the number of stations that detect the event. The WaveLoc event detector is essentially a maximum-picking algorithm. Although selecting local maxima is a relatively simple exercise for smoothly varying signals, it becomes increasingly difficult when the signal is as irregular and jagged as that in

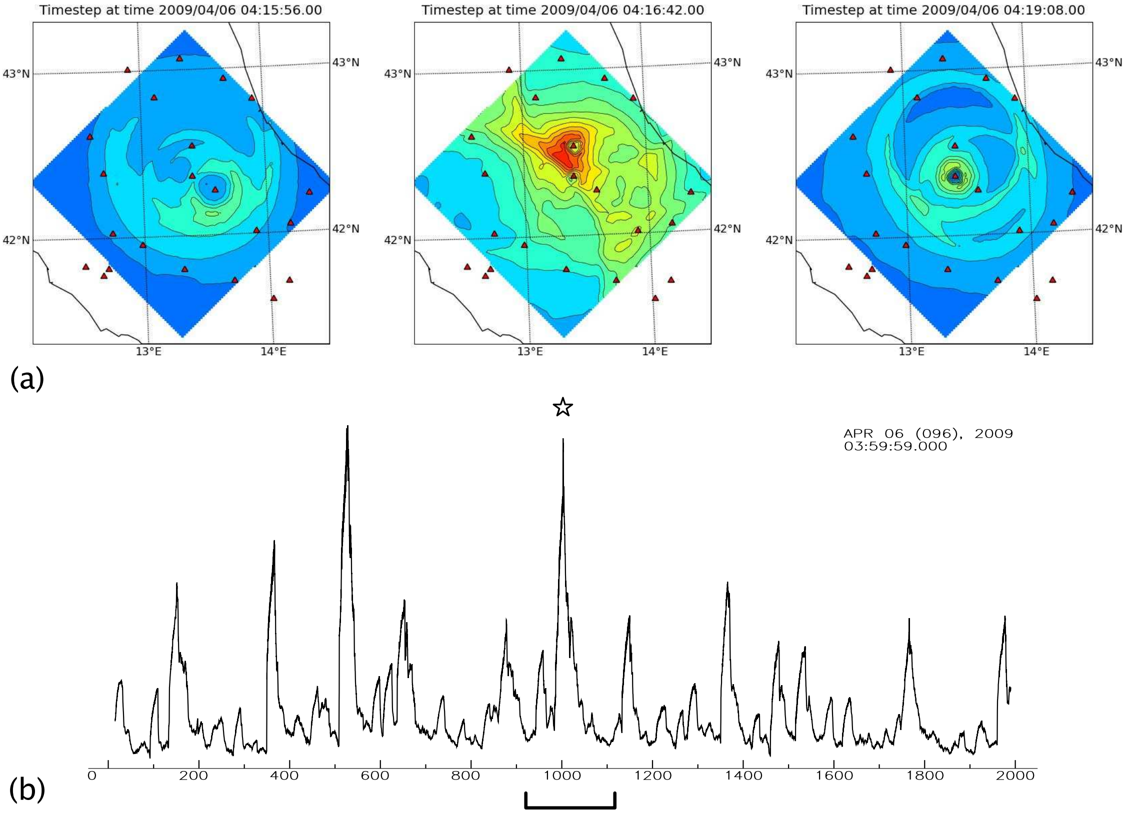

Figure 3.5: Correlation time-slices and the maximum-correlation time-series $S_{max}(t)$ for a 35-minute time-span of the L'Aquila sequence starting April 6th at 04:00 GMT. (a) Time slices through the stacked correlations from equation (3.5). Amplitude of the stacked correlation is indicated by the color-scale, from blue (low correlation values) to red (high correlation values). (b) $S_{max}(t)$ for the 35-minute time-span. The three time-slices in (a) all occur within the time-span indicated below the horizontal axis of the plot. The local maximum indicated by the star corresponds to the central time-slice in (a).

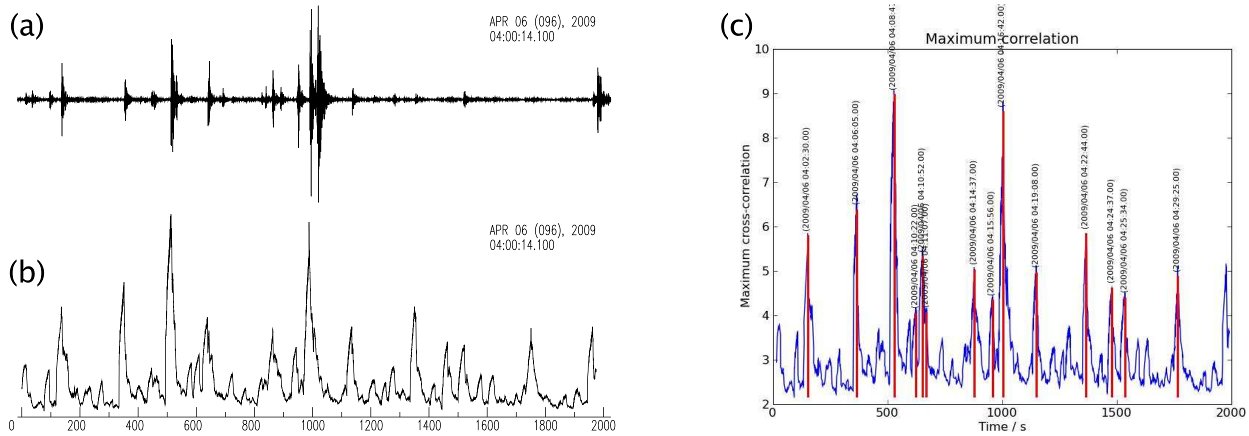

Figure 3.6: The WaveLoc detector. (a) Raw data from station AQU (L'Aquila) for the same 35-minute time-span illustrated in Fig. 3.5. (b) The corresponding $S_{max}(t)$ time-series. (c) The $S_{max}(t)$ time-series after WaveLoc event detection: red bars indicate event detections; the corresponding origin times are written above them.

Fig. 3.6b, and contains many small local maxima on the flanks of the more prominent ones.

The problem turns out to be analogous to that of automatically selecting windows around portions of a signal containing energy from distinct seismic phases, a problem addressed by the Flexwin algorithm of Maggi et al. (2009). The WaveLoc detector design was strongly influenced by previous work on that algorithm. It operates on a smoothed version of $S_{max}(t)$, obtained by cubic spline interpolation using a smoothing length of 5 s (one third of the length of the kurtosis filter), and considers only the local maxima that lie above a water-level w (we have found $w = 4$ to be a good choice for the 15 s window kurtosis pre-processing). The detector evaluates whether or not a smaller maximum above this water-level should be considered as a detection by taking into account its amplitude relative to a near-by larger maximum, and their distance in time: small maxima close to large ones are rejected, while those further away may still be accepted if they are prominent enough. Time-separation between maxima is considered relative to the characteristic time-scale of $S_{max}(t)$, which we have taken to be the kurtosis window-length Δt_k: two local maxima of equal height are considered as detections of two distinct events if they are separated in time by at least $2\Delta t_k$.

Once an event has been detected, its origin time is given by the time of the local maximum in $S_{max}(t)$ (Fig. 3.6c), and its epicenter is given by the $\mathbf{x}_j$ point at which that maximum occurred. For a regularly spaced grid of $\mathbf{x}_j$ points, the epicenter has a minimum uncertainty equal to the grid spacing.

3 Application details

During the developement of WaveLoc, we have tested the technique on many earthquakes in Italy at a regional scale (Maggi and Michelini, 2009a,b). In this paper, we focus on its application to the M_w6.1 April 6 2009 (01:32 UTC) L'Aquila earthquake that shook Central Italy, causing more than 300 fatalities, and to the first 25 days of its aftershock sequence.

3.1 Data

The waveform data used in this study were recorded by the stations of the Italian National Seismic Network (international network code IV) and MedNet (international network code MN, Amato et al., 2006; Mazza et al., 2005), run by the Istituto Nazionale di Geofisica e Vulcanologia, INGV. Twenty-five permanent stations, consisting mainly of 3-component broadband recordings (40 s period sensors) are situated within a radius of 100 km from the city of L'Aquila, and are telemetered to the main acquisition center at INGV in Rome. We also used additional data from the post-seismic deployment of temporary stations consisting of 20 short period, standalone velocimeters (5 s sensors), and 5 telemetered strong motion instruments (Fig. 3.7a). Data from the permanent stations are sampled at 100 Hz, data from the standalone short period stations at 125 Hz, and the strong motion data at 50 Hz. All the data have been archived in miniSEED format (FDSN, 2006), and are available from `http://eida.rm.ingv.it`.

For the purpose of this study we have selected vertical component data, from 00:00 UTC on April 6, 2009, to 23:59 UTC on April 30, 2009, for a total of 25 days. The data were time-synchronized, decimated to 10 Hz after low-pass filtering at 2.5 Hz in order to avoid possible aliasing, then were arranged in 35-minute time-windows, with an overlap of 5 minutes every half hour. Given that many of the stations rely on satellite telemetry, gaps are present in some of the data. In order to avoid signal processing problems induced by data-gaps, we have only considered stations that recorded and transmitted successfully all the data samples within a given 35-minute time-window. Therefore, our station coverage varies between time-windows. For the 25 days covered by this study, the median value of the number of stations used for a single time-window is 45, the mean value is 43 and all windows but one contain complete data recorded by more than ten stations.

z (km)	0.00	3.50	9.60	17.60	35.20
V_P (km/s)	5.00	5.85	6.21	6.90	8.10

Table 3.1: The central Apennines velocity model (Li et al., 2007), used to produce reference waveforms for WaveLoc.

3.2 Grid and reference waveforms

For this study we use a set of potential seismic source locations consisting of a 150×150 km square grid of 2,500 points spaced by 3 km, and spanning 22,500 km^2. The grid center is at (42.33 N, 13.33 E) near the epicenter of the L'Aquila main shock (Fig. 3.7a).

We adopt simple, P-wave travel-time envelopes as reference waveforms. We calculate the travel-times using a standard 1D ray-tracing algorithm, applied to the central Apennines velocity model determined by Li et al. (2007) and reproduced in Table 3.1. The travel-times are inserted as Dirac delta functions, then convolved with a 1 s box-car function. We apply a linear distance scaling to the box-car amplitudes, in order to account approximately for the attenuation of amplitudes with distance. We construct reference waveforms for a fixed source depth of 8 km, and epicentral distances ranging from 5 to 300 km at 1 km intervals.

4 Results and analysis

In the following, we shall analyze the results of applying the WaveLoc algorithm to the aftershock sequence of the L'Aquila earthquake. The mainshock generated a strong coda, and raised the background noise level for several minutes, making it significantly more difficult to detect the immediate aftershocks. We therefore divide this analysis in two parts: we start by discussing the first 25 days of the aftershock sequence starting half an hour after the main-shock, and continue by discussing in detail the first half hour of the aftershock sequence.

4.1 Results excluding the first half-hour

The results of the analysis of the 25 days of aftershock sequence excluding the first half-hour, but including the main-shock itself, are shown in Figs. 3.7–3.10. WaveLoc detected a total of 13679 events in this time period, using 15 s kurtosis windows and a detector water-level $w = 4$. Of these events, 198 were common to the end of one overlapping 35-minute time-period and the start of the next. Once these multiply-detected events were removed from the catalog, we were left with 13481

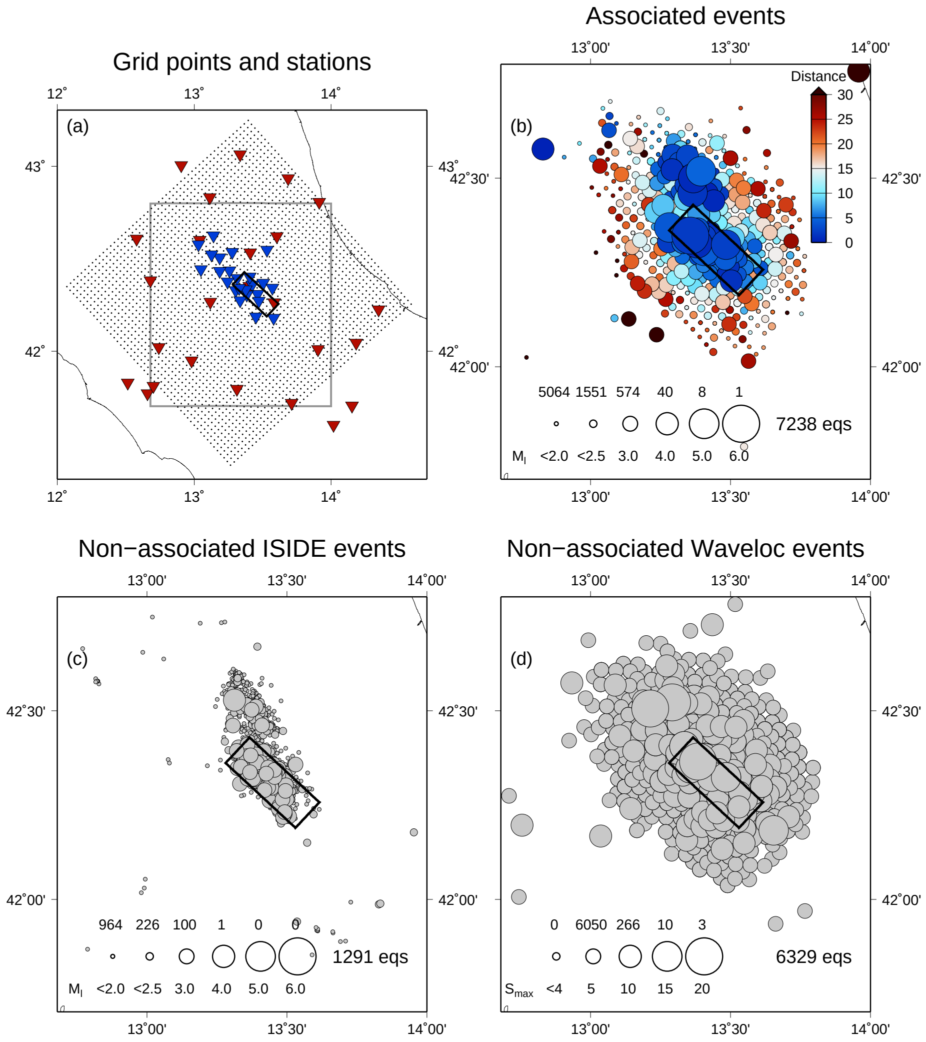

Figure 3.7: (a) Map of grid points (black dots) and station locations (inverted triangles). Permanent stations are shown in red, and stations from the post-seismic temporary deployment are shown in blue. The perimeter of the region of slip for the L'Aquila main-shock (Cirella et al., 2009) is indicated by a black rectangle. The grey rectangle delineates the region shown in panels (b) to (d). (b) Geographical distribution of events associated between the ISIDE (IS) and WaveLoc (WL) catalogs. Events are plotted at their WL locations. Symbol size is determined by the local magnitude M_L from IS, and color by the distance between the IS and WL locations. Sizes used are shown at the bottom of the panel: $M_L < 2$, < 2.5, < 3.5, < 4.5, < 5.5 and $M_L \geq 5.5$. The number of events in each magnitude group is shown above the respective symbol. (c) Non-associated events from IS. Symbol sizes as in (b). (d) Non-associated events from WL. Symbol size is determined by the maximum correlation value S_{max} corresponding to the event detection. Sizes used are shown at the bottom of the panel: $S_{max} < 4$, $4 \leq S_{max} < 7.5$, $7.5 \leq S_{max} < 12.5$, $12.5 \leq S_{max} < 17.5$, and $S_{max} \geq 17.5$.

WaveLoc detections.

In order to appraise the performance of WaveLoc, we have systematically compared the catalog we obtained (WL) to the final bulletin locations reported by INGV, which are available from the INGV-ISIDE web portal (IS, `http://iside.rm.ingv.it`). The IS bulletin locations are all manually determined and verified by the INGV personnel. The final bulletin for the period covering the first 25 days of the L'Aquila sequence was published in early 2010 and contains 8444 events if we exclude the first half-hour after the main-shock. For our earlier work on WaveLoc and the L'Aquila sequence (Maggi and Michelini, 2009b), only the preliminary manual locations provided by the INGV seismic center were available from ISIDE, and they concerned fewer than 5000 events. ISIDE bulletin locations for the L'Aquila sequence were obtained using data from the permanent stations and from the 5 additional strong motion stations telemetered to the INGV seismic center. Data from the short period, standalone temporary stations were not used.

We have associated events between the IS and WL catalogs based solely on absolute origin time difference $|T_0| \leq 10$ s. We were able to associate 7238 events between the two catalogs (Fig. 3.7b), and were left with 1291 unassociated IS events (Fig. 3.7c), and 6329 unassociated WL events (Fig. 3.7d). The associated events in Fig. 3.7b are plotted at their WL locations, and color-coded according to the distances between the IS and WL epicenters ($\Delta_{\mathrm{IS-WL}}$). The better located events (blue in the figure) are, unsurprisingly, the larger ones ($M_L > 2.5$), and tend to delineate the two main aftershock zones of the L'Aquila earthquake: the southern one, responsible for the main-shock and whose slip region is denoted by the black rectangle in the figure (Cirella et al., 2009); and the secondary fault zone to the North (Chiarabba et al., 2009), activated later in the aftershock sequence. WaveLoc detected 85% of M_L $2.5-3.5$ events listed by ISIDE, and of the 50 $M_L > 3.5$ events, only one was missed (98% detection rate). The missed earthquake was a $M_L 3.6$ event (2009-04-14 17:27:30) that occurred only seconds after a M_L 2.6 event that was detected by WaveLoc (see section 5.2 for more details).

The completion of the WL catalog as a function of magnitude is examined in more detail in Fig. 3.8a, WaveLoc detects more than 60% of the events present in the ISIDE catalog, regardless of magnitude. Missed events start at $M_L \sim 3.0$ and increase in number with decreasing magnitude, as the smaller signal-to-noise ratio of the data makes automatic detection more difficult. The IS catalog is considered to be complete for $M_L > 1.8$. Therefore the decrease in number of events missed by WaveLoc for $M_L < 1.5$ is only apparent, as the IS catalog itself is far from complete at these magnitudes. Fig. 3.8b shows that, although even small values

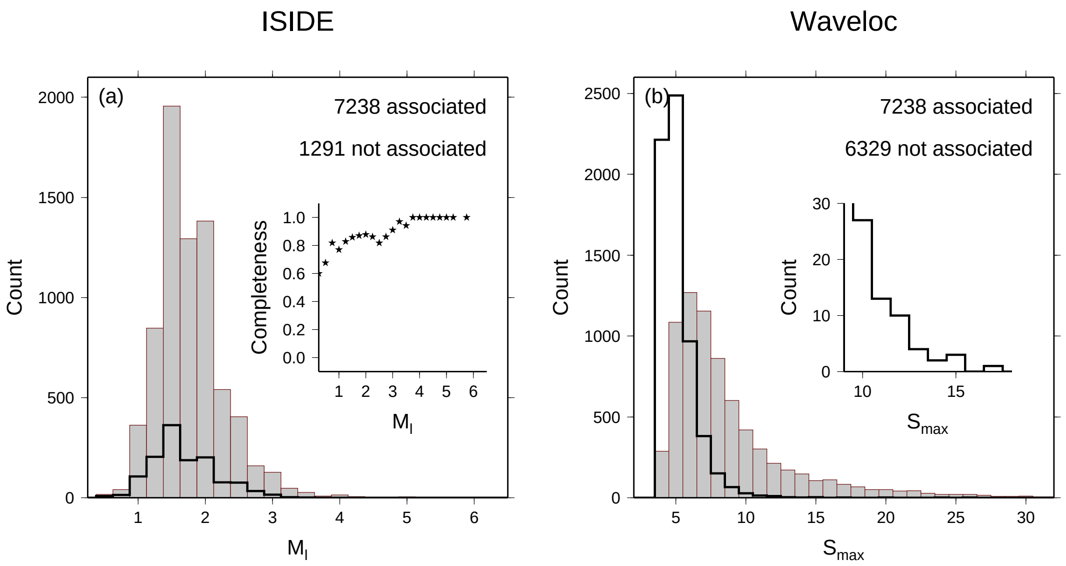

Figure 3.8: (a) Histogram of the magnitude distribution of events present in both IS and WL catalogs (grey) and those present only in the IS catalog (thick black line). Inset shows the fraction of events in the IS catalog detected by WaveLoc, as a function of magnitude. (b) Histogram of the S_{max} distribution of events present in both catalogs (grey) and those present only in the WL catalog (thick black line). Inset shows a blown-up version for the WL-only events with $S_{max} \geq 10$.

of $S_{\max}$ can indicate WaveLoc detection of events that are also found in ISIDE, the number of WL detections that cannot be associated increases exponentially for $S_{\max} < 10$. A proportion of these over 6000 small-$S_{\max}$ detections are likely to be spurious, but given their number we have not investigated them in detail. Rather, we have concentrated our efforts in understanding the occurrence of the 35 $S_{\max} > 10$ detections not present in ISIDE, and have found 8 events missed by the manually verified catalog that were well recorded across the network of permanent stations, and 15 that were well recorded only on the temporary network. A detailed discussion of all the missed $S_{\max} > 10$ events can be found in section 5.3.

The relationship between M_L, the maximum correlation S_{max}, and the differences between the IS and WL epicentral locations ($\Delta_{\text{IS}-\text{WL}}$), is explored in Fig. 3.9. Fig. 3.9a shows that nearly all events with $S_{max} > 15$ are located to better than 10 km by WaveLoc, suggesting that the maximum correlation is good indicator of location quality. The maximum values of S_{max} for each magnitude scale approximately with M_L, however the size of the scatter precludes using S_{max} as a WaveLoc proxy to magnitude. The value of S_{max} scales as the proportion of events within the data set with clean enough signals for the P-wave arrival to produce a strong kurtosis peak. As larger magnitude events are generally better recorded across the network, they

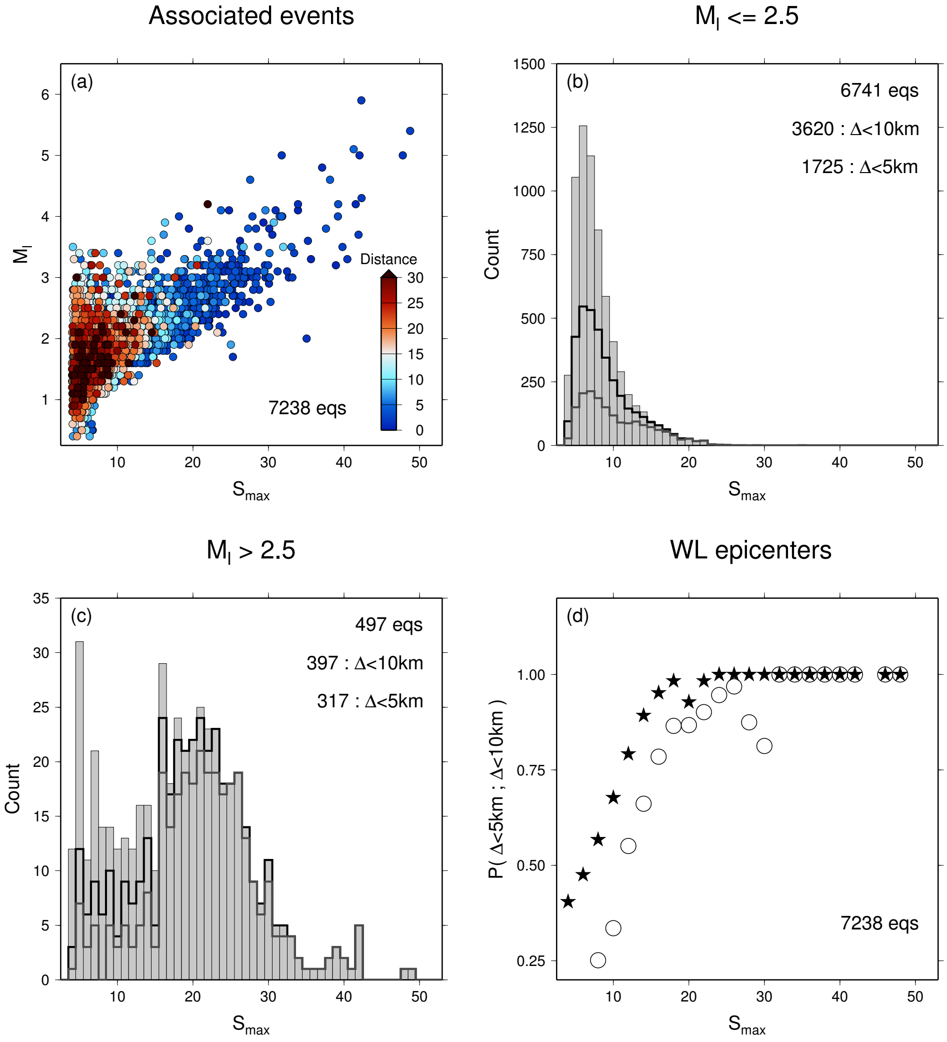

Figure 3.9: (a) Distribution of M_L and epicentral difference $\Delta_{\mathrm{IS-WL}}$ as a function of $S_{\max}$. Symbol color indicates epicentral distance in km. All 7238 associated events are plotted, in order of increasing $\Delta_{\mathrm{IS-WL}}$, so that bad quality locations appear above the better ones in the scatter plot. (b) Histogram of $S_{\max}$ values for associated events with $M_L <= 2.5$. The thick black line indicates events located with $\Delta_{\mathrm{IS-WL}} < 10$ km, and the thick grey line those located with $\Delta_{\mathrm{IS-WL}} < 5$ km. (c) As (b) for associated events with $M_L > 2.5$ (d) The probability of a WaveLoc detected event being located with $\Delta_{\mathrm{IS-WL}} < 10$ km (filled stars) or with $\Delta_{\mathrm{IS-WL}} < 10$ km (open circles) as a function of $S_{\max}$.

will tend to produce larger S_{max} values. For the L'Aquila sequence, $S_{max} > 15$ for all $M_L > 3.5$ events, however, S_{max} values > 15 have also been obtained for events as small as M_L 1.5, confirming the unpracticality of using S_{max} alone to estimate the size of an event.

In Fig. 3.9b,c we plot histograms of S_{max} values for two classes of events, those with magnitude below and above M_L 2.5 respectively. In both cases, we outline those events that we consider to be well-located, i.e. those for which the distance between the IS and WL epicentral locations, $\Delta_{\mathrm{IS-WL}}$, is smaller than 5 or 10 km. Although the distribution of S_{max} for small earthquakes ($M_L \leq 2.5$, Fig. 3.9b) peaks at values of 6–7, then falls off towards higher values, a significant number of these events are detected with $S_{max} > 10$. The distribution of S_{max} for larger earthquakes ($M_L > 2.5$, Fig. 3.9c) is more irregular, with the majority of events being detected with S_{max} values between 15 and 30. The proportion of well-located events increases with S_{max} for both small and large earthquakes, and tends to 100% for $S_{max} > 15$. The quality of a WaveLoc epicenter location may, therefore, be estimated from the value of S_{max}, as illustrated in Fig. 3.9d: the probability that a WL event is located to within 10 km (or 5 km) of the corresponding manual location increases rapidly with increasing S_{max}, and tends to 1 for $S_{max} > 15$ (or $S_{max} > 25$). We may therefore be reasonably confident in the WaveLoc epicentral locations for these larger S_{max} events, as is confirmed by the distribution of $\Delta_{\mathrm{IS-WL}}$ values shown in Fig. 3.10a where it can be seen that the differences peak at distances around 2 km.

We now asses in more detail the differences in origin time and depth estimates between WaveLoc and the ISIDE catalog. The distributions of depth differences, $\Delta h_{\mathrm{IS-WL}}$, and origin time differences, $\Delta t_{\mathrm{IS-WL}}$, are shown in Fig. 3.10b,c respectively. The depth distribution (Fig. 3.10b) peaks at $\Delta h_{\mathrm{IS-WL}} = 2$ km, consistent with the discrepancy between the fixed depth for which we have calculated the reference waveforms (8 km), and the median depth of events in the L'Aquila sequence (10 km, Chiarabba et al., 2009). As the WL depth is fixed, this histogram essentially illustrates the depth distribution of events in the IS catalog. The distribution for $S_{max} > 15$ retains approximately the same shape, but is more compact.

The origin time distribution (Fig. 3.10c) peaks at $\Delta t_{\mathrm{IS-WL}} = -2$ s for all events, and at $\Delta t_{\mathrm{IS-WL}} = -0.5$ s for $S_{max} > 15$. This latter value is not unreasonable: given the 2 km depth discrepancy mentioned above, and the velocity model from Table 3.1, we would expect the origin time distribution to peak at -0.3 s. Although the $S_{max} > 15$ events are broadly consistent with this prediction, they display a much larger dispersion in $\Delta t_{\mathrm{IS-WL}}$ than would be required to account for their respective values of $\Delta h_{\mathrm{IS-WL}}$ via the well-known depth/origin-time trade-off. Indeed, when

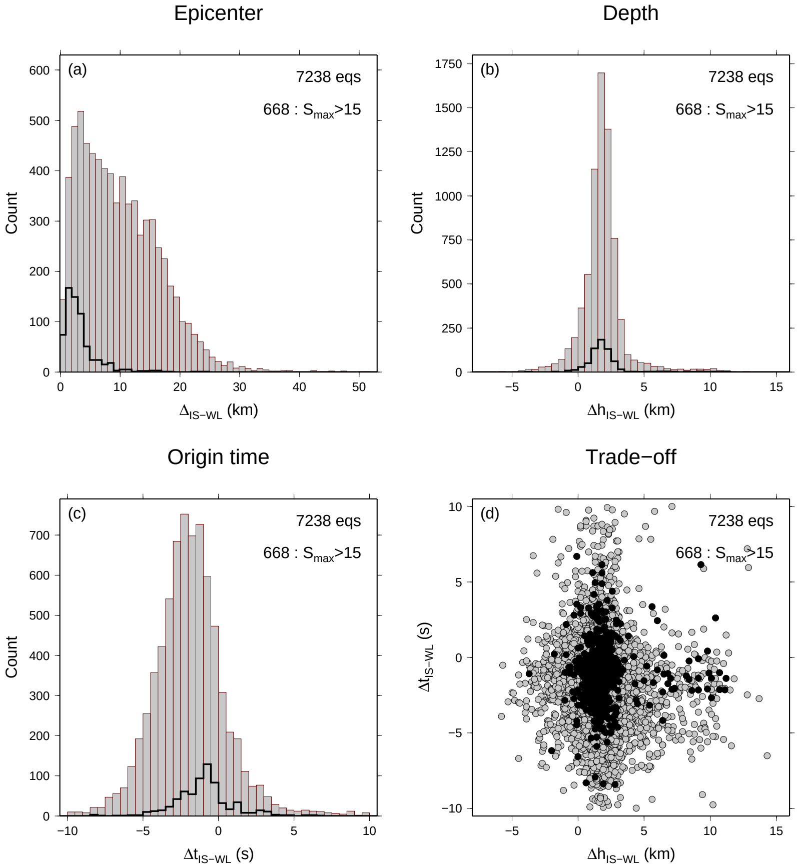

Figure 3.10: (a) Histograms of (a) epicentral difference $\Delta_{\mathrm{IS-WL}}$, (b) depth difference $\Delta h_{\mathrm{IS-WL}}$ and (c) origin time difference $\Delta t_{\mathrm{IS-WL}}$ for associated events. The thick black line (in (a-c)) indicates events detected with $S_{\max} > 15$. (d) Distribution of $\Delta t_{\mathrm{IS-WL}}$ as a function of $\Delta h_{\mathrm{IS-WL}}$, with $S_{\max} > 15$ events shown as filled circles.

we plot $\Delta t_{\mathrm{IS-WL}}$ against $\Delta h_{\mathrm{IS-WL}}$ in Fig. 3.10d, the trade-off we expect to see is swamped. In section 5.1, we shall explain the probable mechanism behind the dispersion in WaveLoc origin times.

4.2 The first half-hour

The first half hour after a main shock is certainly the most difficult to analyse for any automatic detection/location seismic monitoring system (e.g., Vidale et al., 2003). Aftershocks occurring in the initial few minutes are difficult to observe due to the mainshock coda, clipped recordings, and the confusion of many nearly simultaneous events, all of which raise the background noise level. For the L'Aquila earthquake, this increased noise level lasts for several minutes after the mainshock, and we have found that the kurtosis processing parameters used for the 25 days of the aftershock sequence are unsuited to the first half-hour of the sequence.

The first half-hour of the L'Aquila sequence recorded at the AQU station (STS2, HHZ) is shown in Fig. 3.11a. This station is nearly co-located with the epicenter of the main shock, and it represents perhaps the most faithful index of the immediate aftershocks, since it is the least affected by the mix of coda and surface waves affecting more distant stations. First we note that the background noise level changes dramatically before and after the mainshock: the ratio between noise levels for time windows two minutes after and before the first P-wave arrival is about 2000. This ratio decreases progressively to about 50 at the end of the half-hour window.

The kurtosis processing, as any other methodology that seeks abrupt amplitude variations of the signal, is affected by the range of background variability of the waveforms, and produces smaller peak values when encountering a signal change in the presence of strong noise. This behavior is illustrated in Figure 3.11a, that shows S_{max} and the vertical component data at AQU for the 35' window starting just before the mainshock origin time. The red horizontal line in the top panel of Figure 3.11a indicates the $w = 4$ detection water-level adopted for rest of the L'Aquila sequence; using this value for the first half-hour results in only three event detections (Figure 3.11c).

Figure 3.11b shows a close-up of S_{max} and the AQU data just after the mainshock: it is clear that there are many distinct local maxima in S_{max} that correspond to distinguishable aftershocks, although none reach the standard, preset detection level. We have lowered the detection level to $w = 2.25$, which appears to be a reasonable compromise between increased detection and the background S_{max} level, and obtain 16 event detections, corresponding to most of the S_{max} peaks (Figure 3.11d). For

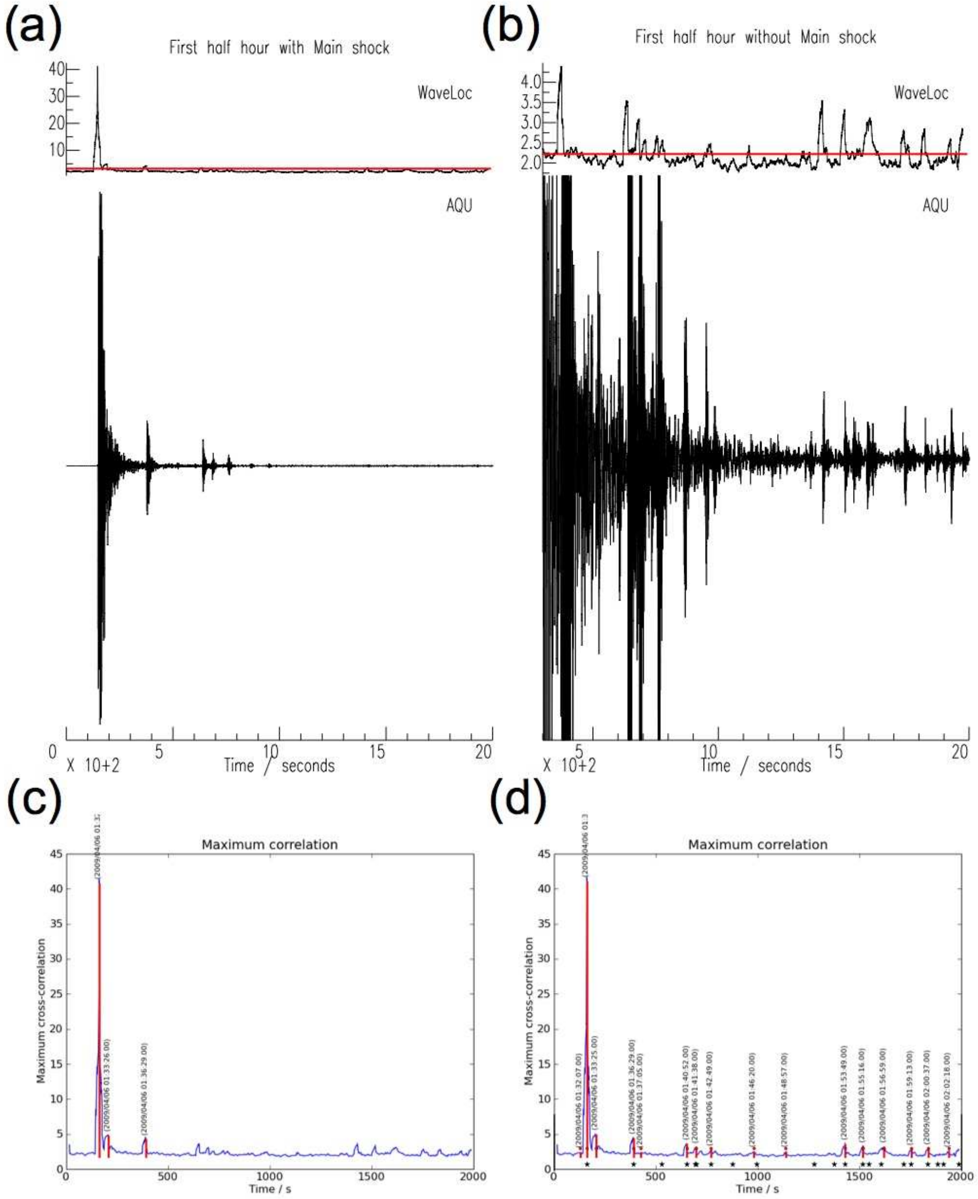

Figure 3.11: First half hour after the L'Aquila main shock using the standard 15 s window kurtosis processing. (a) Maximum correlation value ($S_{max}(t)$), the red horizontal line indicates the $w = 4$ threshold; (b) same as (a) but for $w = 2.25$ and removing the initial part of the time series that contains the main shock; (c) Flexwin detections relative to (a); (d) same as (c) but using the $w = 2.25$ value and removing the initial part of the time series. The stars at the bottom of the maximum correlation in (d) indicate the earthquakes listed in ISIDE. For reference, the recordings of the HHZ channel of station AQU are shown.

comparison, we have also plotted stars at the origin times of earthquakes listed in IS, and we note a good match between WL and IS for most of the events.

5 Discussion

We designed WaveLoc primarily as a robust automatic detector, and preliminary locator, of seismic phenomena, capable of working on a large number of data streams. WaveLoc uses a correlation approach (Young et al., 1996; Withers et al., 1999) to take advantage of the coherence of seismic signals across a network, after enhancing the information-carrying part of these signals by suitable pre-processing.

We have tested the technique using data recorded by the Italian National Seismic Network of the recent L'Aquila earthquake sequence that followed the $M_w 6.1$ main shock. With the exclusion of the first half-hour after the main shock which is problematic for almost any automatic location system because of the large noise level induced by the main shock and the cascade of aftershocks, our results have shown that nearly 100% of the seismic events having magnitude larger than 3.0 have been detected and located properly. More specifically it has been shown in Fig. 3.9 and Fig. 3.10a that the epicentral differences between locations from manually picked onset phases and those obtained automatically from WaveLoc are in the largest majority confined within 5 km for $M \geq 3.0$ events. At $M = 2$, nearly 80% of the events reported in ISIDE have been correctly detected and the detection level decreases significantly only for earthquakes with $M \leq 1.5$ (only 36%, Fig. 3.8a). In Italy, the agreement between INGV and the national authorities in charge of civil protection encompasses the notification of $M_L \geq 2.5$ earthquakes. This threshold value is generally representative, depending on population density of the area and source depth, of the magnitude above which earthquakes are felt. From the L'Aquila sequence analysis, we find that more than 90% of the earthquakes having local magnitude around $M_L = 2.5$ are properly identified.

The WaveLoc algorithm, despite being computationally intensive, is very easy to parallelize. We have therefore been able to progress from a computation time of 5-minutes for each 35-minute span of data on a laptop computer Maggi and Michelini (2009a,b), to a computation time of 40-minutes for the entire 25-day data-set on the INGV cluster that consists of 512 CPUs. Since WaveLoc analyses the time windows independently no effort is required to separate the problem into a number of parallel tasks. This computation time should be compared with the 8 months required for INGV to produce the final, validated ISIDE catalog for the L'Aquila event.

In the following, we shall examine in more detail the remaining discrepancies between the WL and IS catalogs for the L'Aquila sequence. We shall see that although WaveLoc is not perfect, it is able to detect events that were missed by the manual catalogs. We shall then discuss the usefulness of WaveLoc in the contexts of data-mining and real-time seismic monitoring, and the directions of future development of the method.

5.1 Origin time dispersion

As briefly mentioned at the end of Section 4.1, the dispersion in WL origin times is much greater than would be expected from the fixed-depth assumption, and the distribution of origin-time errors $\Delta t_{\mathrm{IS-WL}}$, shown in Fig.3.10c, is centered around -2 s (or -0.5 s for $S_{\max} > 15$ events). In order to understand the cause of the origin-time dispersion, it is useful to go back to the basic WaveLoc procedure as described in Fig. 3.2: if the velocity model used to construct the reference waveforms is correct, and the data-processing correctly enhances the P-wave arrival, then all the collapsing circles in Fig. 3.2 will intersect at the true epicenter and origin time.

Let us assume that the velocity model used to construct the reference waveforms is faster than the real Earth, and run the collapsing-circles thought experiment. The circles would start out being smaller, and each would collapse towards its corresponding station faster. For stations at different distances from the epicenter, and in the limit of infinitely thin circles, the circles would never intersect at a point, and would generate multiple locations for each earthquake. In practice, however, the width of the collapsing circles is controlled by the spacing of potential epicenters, and the width of the signal in the reference waveforms (respectively 3 km and 1 s in our case). We have estimated the effect of Earth-model errors in our implementation of WaveLoc by predicting P-wave arrival times using IS locations and our velocity model (Table 3.1 and Li et al., 2007), and comparing them with the corresponding ISIDE P-wave picks. We find an error of $\Delta t_{\mathrm{IS-Pred}} = 0.7 \pm 0.8$ s (Hector, 2010). This error is comparable to the 1 s width of the pulses in our reference functions, indicating that the collapsing circles will still overlap. It is also consistent with the -0.5 s shift in WL origin times for the $S_{\max} > 15$ events: the Earth model is faster than that assumed by ISIDE, so the pulses in the reference waveforms will occur earlier in the signal, and therefore the origin times predicted using WaveLoc will be systematically late.

Errors in the Earth model alone cannot account for the large dispersion in origin time errors in Fig.3.10c. Although the kurtosis processing is highly effective in enhancing the first P-wave arrival (Fig 3.3; Fig 3.4; Saragiotis et al., 2002; Gentili

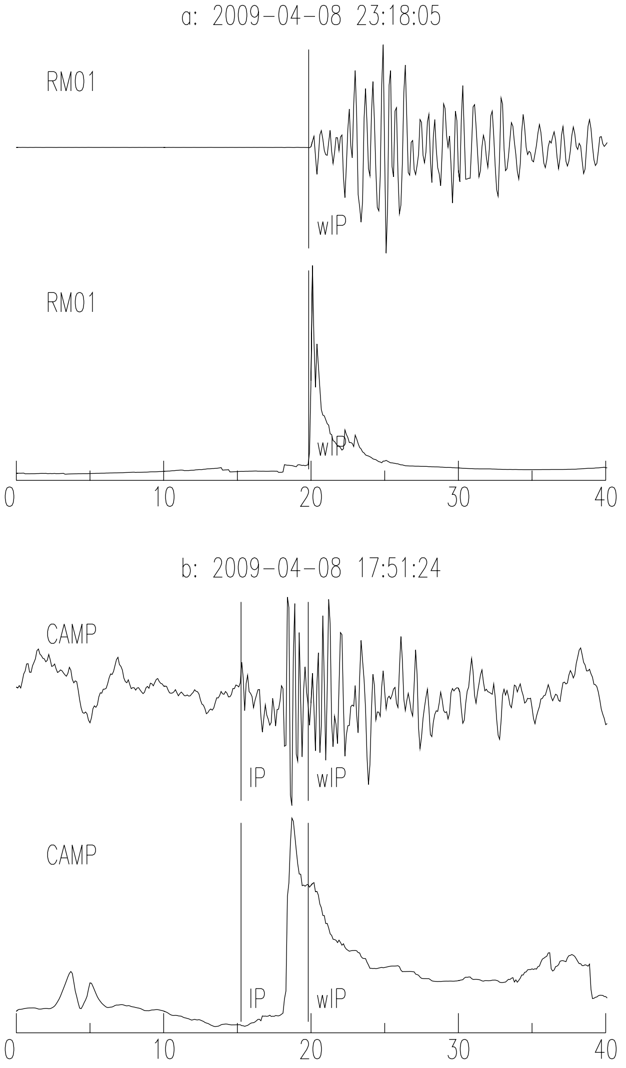

Figure 3.12: Example of kurtosis pre-processing for different levels of station background noise and P-, S-wave phase character. (a) Impulsive P-wave onset phase within relatively small amounts of background noise; (b) P-wave onset within significant background noise. In this latter case the kurtosis pre-processing enhances the larger and relatively more impulsive S-wave.

and Michelini, 2006), it is not infallible. In some cases, notably in the presence of significant noise, the kurtosis pre-processing enhances the S-wave rather than the P-wave (see Fig. 3.12 for an example). The effect on WaveLoc is the same as using a very fast Earth model: as $V_p > V_s$, the pulses in the reference waveforms will occur earlier than those in the corresponding kurtosis waveforms, and the WL origin times will be systematically late. For a circular band of stations at distance Δ from the epicenter, the delay in origin time is, trivially, $\Delta(V_P - V_S)/(V_P V_S)$. The problem becomes much less trivial when the complex geometry of the seismic network is taken into account: each successive concentric band of stations for which the S-wave is enhanced will generate circles that intersect at the epicenter at a different origin-time, but will also interfere with all the remaining stations, leading to local maxima in $S_{\max}$ that are not necessarily located at the epicenter, and can even occur before the true origin time. Further complexity is added when we consider that seismic noise can be highly station-dependent, and therefore some stations in the network may correctly enhance the first arriving P-wave, while others enhance a later, more impulsive P-wave phase, and yet others the S-wave, further reducing the coherence across the network. Incorrect kurtosis enhancements therefore lead directly to noise in the $S_{\max}$ waveform, and can cause the origin-time dispersion we observe. This behavior tends to occur for smaller size events featuring more emergent onset phases.

We have implemented the following steps to cope with and reduce the noise in $S_{\max}$. Firstly, the maximum-picking algorithm that serves as the WaveLoc event detector (Section 2.4) is designed to reject secondary maxima in $S_{\max}$, and therefore to reduce the probability of selecting an incorrect origin-time and epicenter when only a small number of stations display late kurtosis enhancements. Secondly, the linear distance scaling we apply to the P-wave travel-time reference waveforms (Section 3.2) enhances the effect of the nearby stations, for which the P- and S-waves arrive closer in time to each other, thereby increasing the probability that their circles will intersect close to the epicenter. In order to reduce this origin-time dispersion further in future WaveLoc development, we shall investigate improvements in pre-processing (e.g. high-pass filtering, multiple processing methods) to ensure more systematic true-P-wave enhancement, and also design a new detector that uses the full information in the correlation maps, rather than simply the $S_{\max}$ value. However, as with all other location methods, the coherence of signals across a network and hence the quality of WaveLoc locations will always depend strongly on the network geometry and the signal-to-noise ratios at each station.

Origin time	Lat (°N)	Lon (°E)	M_L
2009-04-06 02:13:51	42.344	13.455	3.1
2009-04-06 02:18:32	42.461	13.307	3.1
2009-04-06 03:13:34	42.338	13.368	3.1
2009-04-06 04:17:06	42.334	13.426	3.2
2009-04-06 13:14:04	42.232	13.492	3.2
2009-04-07 17:48:41	42.358	13.531	3.3
2009-04-14 17:27:30	42.528	13.313	3.6

Table 3.2: ISIDE events with $M_L > 3$ that were missed by WaveLoc. Origin times and epicentral locations are those provided by IS.

5.2 Events missed by WaveLoc

In the ISIDE catalog, there are 7 events with $M_L > 3.0$ that are not associated with events detected by WaveLoc (see inset in Fig.3.8a). The complete list of these missed events can be found in Table 3.2, and three example events are shown in Fig. 3.13. Four of these events occurred in the first three hours after the L'Aquila mainshock, when the superposition of many hundreds of aftershocks reduces the ability of the kurtosis filter to efficiently enhance coherence across the permanent broad-band network, the only one running at the time. The combined effects of noisy data and few stations, in turn, lead to relatively low values of $S_{\max}$ that fail to trigger the WaveLoc detector: the $S_{\max}$ maximum corresponding to the first of the two distinct events in Fig.3.13a is smaller than the $w = 4$ detection water-level, as is the maximum corresponding to the second of the two distinct events in Fig.3.13b.

The missed M_L3.6 event (2009-04-14 17:27:30, Fig.3.13c) merits special discussion, as it is a large event that occurred ∼12 s after a much smaller M_L2.6 event that WaveLoc detected successfully. The primary cause of this event being missed is its closeness in time with the previous event: as the large amplitudes from the first event are still present within the 15 s kurtosis window when the second event occurs, the distribution of amplitude values within the window becomes more gaussian, and the kurtosis value for the start of the second event is reduced, leading to a smaller amplitude maximum in $S_{\max}$. For this event, however, $S_{\max} > 4$, but the second maximum is small in amplitude and close in time compared to the first maximum, and therefore fails to be recognized as an independent event by the WaveLoc detector (see Section 2.4). The behavior of the WL detector could be tuned to include more secondary maxima as independent events, but this would lead to a much greater number of false positive detections, as we shall discuss in Section 5.3.

For smaller magnitude events, loss of sensitivity of the kurtosis filter to the second of two events occurring close in time can be much stronger than in this example,

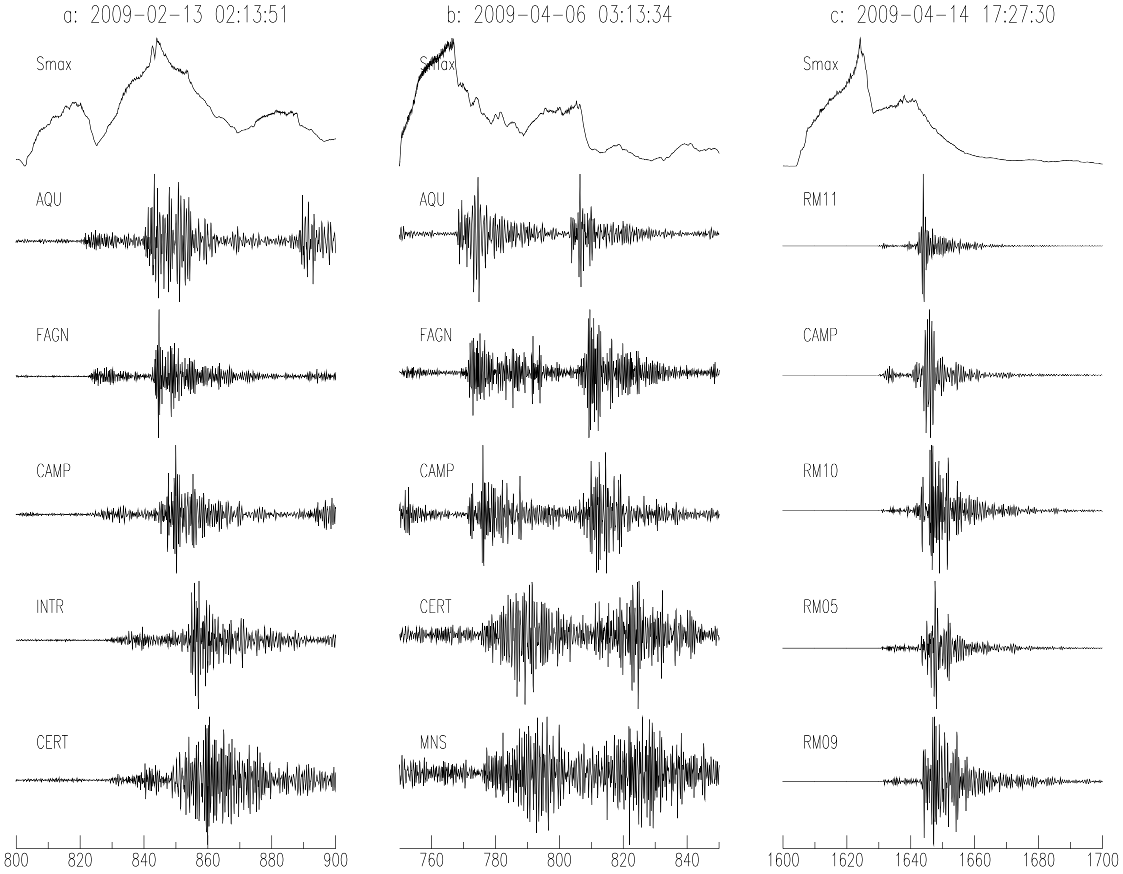

Figure 3.13: Examples of events detected by IS and missed by WL. (a) The (top subpanel) maximum corresponding to the first of the two distinct events is smaller than the $w = 4$ detection water-level; (b) the $S_{\max}$ of the second of the two distinct events is smaller than the $w = 4$ detection water-level (c) two very close in time events where the second, although larger in size ($M_L 2.6$), lies within the larger amplitudes of the first one. (See main text and Table 3.2 for detail.)

as can be seen by comparing the central portions of Fig.3.6a and Fig.3.6b, in which the second of two nearly identical events visible on the AQU raw data completely disappears on the $S_{\max}$ trace. Pathological cases of this kind suggest that it may be time to move beyond using a single processing scheme to enhance first arrivals, to using several schemes together, especially as multiple processing schemes can readily be implemented into the WaveLoc framework (see equation 3.3). Detailed discussion of the implementation of such processing schemes is outside the scope of this paper.

5.3 Events missed by ISIDE

In the WaveLoc catalog, there are 35 events with $S_{\max} > 10$ that are not associated with events from ISIDE (see inset in Fig. 3.8b). From the statistical analysis above, we expect detections with these values of $S_{\max}$ to be reliable, so we have systematically gone back to the recorded data for these events to examine why they could not be associated with IS.

Twenty-three of the unassociated events correspond to local earthquakes visible in the seismic data (Table 3.3). The majority of these (15 events, top of the table) were small, and poorly recorded on three or fewer of the permanent broad-band stations used by INGV to construct the IS catalog. Many of these events occurred within a few minutes of each other, at times in which real-time transmission of data from the permanent network was disrupted. They were successfully detected by WaveLoc on the basis of data from the temporary short-period stations, not used in IS. The first of these events is shown in Fig. 3.14a, as an example. The remaining 8 events (bottom of Table 3.3) were very well recorded across the entire network, as shown by the example in Fig 3.14b, and we believe that human error may have been a factor in these events slipping through the net. In both cases, we are satisfied that WaveLoc produces added value to standard event detection procedures: on the one hand by permitting rapid integration of extra data from temporary deployments, and on the other by catching events that may be missed through human error.

Twelve of the unassociated $S_{\max} > 10$ events turned out to be artifacts. Within these, we counted 6 cases of late $S_{\max}$ maxima that resulted in origin-time differences greater than the 10 s used for association between the IS and WL catalog. The remaining artifacts break down into 5 false positive WL detections due to secondary peaks in $S_{\max}$ behind a well-detected event (example in Fig 3.14c), and one detection of a teleseismic event (the 2009-04-07 04:23:34 Kuril Islands $M_w 7.0$ event).

The late $S_{\max}$ maxima and the false-positive detections from secondary $S_{\max}$ peaks are both related to the behavior of the kurtosis filter. In Fig 3.14c, for ex-

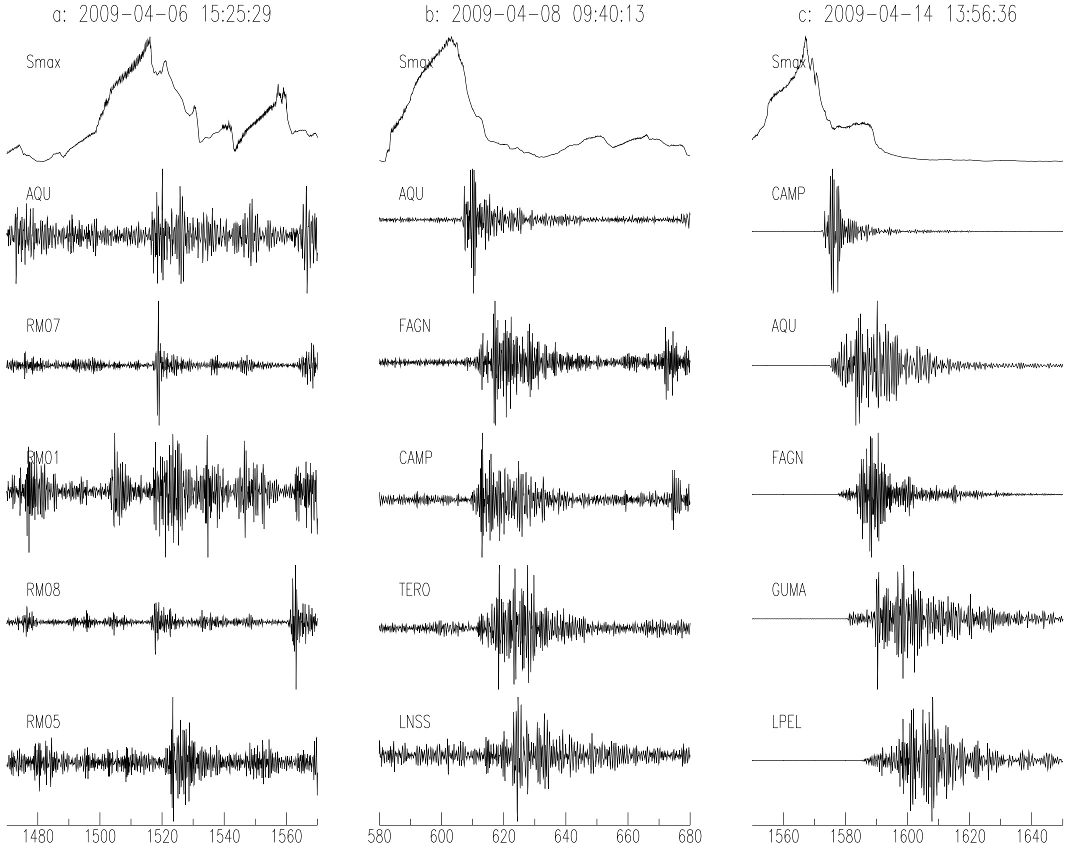

Figure 3.14: Examples of events detected by WL and missed by IS. (a) An event recorded only by AQU and the temporary short-period stations (names start with RM). (b) An event that was well-recorded across the permanent network. (c) A false WL detection. The upturn at the end of the step in $S_{\max}$ after the main peak generated a WL detection. This step was created by strong kurtosis amplitudes from S-waves at some stations, such as GUMA. (See man text and Table 3.3 for detail.)

Origin time	Lat (°N)	Lon (°E)	$S_{\max}$
2009-04-06 15:25:29	42.348	13.357	11.24
2009-04-06 15:29:40	42.456	13.519	10.07
2009-04-06 15:42:26	42.348	13.357	11.25
2009-04-06 15:43:10	42.150	13.549	10.50
2009-04-06 15:48:25	42.330	13.330	10.97
2009-04-06 15:58:56	42.344	13.460	11.89
2009-04-07 05:58:50	42.300	13.611	12.43
2009-04-07 10:09:30	42.344	13.460	11.53
2009-04-07 10:32:55	42.264	13.557	11.01
2009-04-07 11:36:59	42.314	13.252	10.16
2009-04-07 13:05:45	42.304	13.508	10.26
2009-04-09 06:13:56	42.338	13.614	10.75
2009-04-09 12:45:27	42.348	13.357	14.55
2009-04-09 12:48:38	42.348	13.357	11.31
2009-04-09 13:00:04	42.322	13.535	10.53
2009-04-09 01:49:47	42.458	13.468	10.05
2009-04-10 12:04:08	42.230	13.452	10.84
2009-04-11 00:01:22	42.284	13.533	11.08
2009-04-18 19:30:23	42.635	13.351	10.48
2009-04-18 22:03:37	42.324	13.484	14.67
2009-04-20 18:20:59	42.246	13.530	10.62
2009-04-21 01:12:53	42.268	13.454	10.10
2009-04-21 22:26:35	42.184	13.654	13.89

Table 3.3: Confirmed events detected by WaveLoc with $S_{\max} > 10$, but missed by ISIDE. The top part contains events that were recorded essentially on the temporary velocimetric network, and on no more than three stations of the permanent network; the bottom part contains events that were well-recorded across both networks. Origin times and epicentral locations are those provided by WL.

ample, the kurtosis tends to enhance the strong S-wave arrival at station GUMA and similar stations. WaveLoc then back-propagates this energy using the apparent P-wave velocity, thereby creating either a late-arriving maximum in $S_{\max}$, if the kurtosis enhances the S-wave on the majority of stations, or a late-arriving plateau in $S_{\max}$, if only a minority of stations is affected, as in this example. The late $S_{\max}$ maxima cases are extreme cases of the same mechanism that produces the origin-time dispersion discussed in Section 5.1. For the secondary-peak false-positive detections, the local maximum at the end of the plateau in $S_{\max}$ occurs late enough after the principal maximum to be identified as an independent event by the WL detector.

It is important to note the similarity between the shape of $S_{\max}(t)$ in Figs.3.13c and 3.14c: in both cases there is an upwards-trending plateau following a distinct maximum. However, in the first case, this plateau indicates an actual second event that was detected by manual picking and rejected by the WL detector because it occurred too soon after the first event, while in the second case the plateau was created by the kurtosis triggering on the S-wave and was incorrectly accepted by the WL detector. The similarity between these two cases underlines an important limitation of the current implementation of WaveLoc: fine-tuning of the WL detector alone cannot remove both the tendency to miss secondary events and the tendency to trigger on false secondary maxima. Possible solutions to this issue could be extending the analysis to three-component data, and using multiple waveform processing methods (see the general form of equation 3.3), which would be differently sensitive to P- and S-wave arrivals.

Large teleseismic events may trip the WaveLoc detector, as they generate very coherent signals across the entire network, with little or no move-out. The correlations between processed data and reference waveforms are good for all stations, which leads to a large number of overlapping circles in the stacked correlation maps. A teleseismic event therefore produces a broad, high-amplitude peak in $S_{\max}$, whose local maximum is picked by the WL detector, and mapped to a point within the correlation grid. Similar problems can occur for large near-regional events that occur outside of the area covered by the set of epicentral locations tested by WL. In our future development of the WaveLoc algorithm, we shall investigate ways of detecting occurrences of teleseismic or regional events by taking into account the 2D shape of the stacked correlation maps, and the shape of the $S_{\max}$ peaks.

5.4 WaveLoc application to data-mining

In its current implementation, WaveLoc can readily be applied to data-mining applications, as it allows for the rapid processing of very large volumes of waveform data, such as those acquired by temporary networks. The manpower required for the analysis of such large volumes of data is often prohibitive. In this context, WaveLoc can provide robust, rapid and cost-effective detection and preliminary location of the phenomena of interest, even on a very large scale (e.g. an entire national network).

As we have seen above, WaveLoc is currently unable to produce the high-resolution locations that are ultimately required for detailed studies of seismically active regions. The planned improvements to the WaveLoc method mentioned (improved pre-processing, multiple-processing schemes, empirical reference waveforms, consideration of the full 2D correlation maps in the detection algorithm) above will undoubtedly improve the accuracy of its locations, but this improvement may not be sufficient for truly high-resolution applications.

Following the lead of Waldhauser and Schaff (2008) and Waldhauser (2009), we have started to develop a modular automated procedure that uses WaveLoc as an event detector, then goes back to the corresponding original seismograms to perform waveform picking followed by event relocation and magnitude estimation. Preliminary results from this procedure are promising (Hector, 2010), especially regarding the improvement of WaveLoc origin-times.

5.5 WaveLoc in real-time

WaveLoc was designed specifically to work on continuous data streams, with the idea of developing a real-time waveform-based detector and locator of earthquakes or other seismic phenomena to be used alongside more traditional methods in seismic monitoring centers. For real-time operation, incoming data-streams would be pre-processed on the fly, and cross-correlated with the reference waveforms exactly as depicted in Fig. 3.2, thereby producing the 2D correlation maps that could be displayed directly. The detector algorithm described in Section 2.4 would have to be modified to work in near-real time.

In Section 2.1, we have shown that for local and near-regional operation, and in the absence of data latency, WaveLoc can obtain a detection and preliminary location within 20-30 s of the event origin time, depending essentially on station coverage. This time could be shortened slightly by considering only very short epicentral distances in the construction of the reference-waveforms, but this would lead to a reduced set of stations on which to test data coherence, and would reduce the robustness of the method. A robust real-time implementation of WaveLoc would probably be too slow to compete with dedicated Earthquake Early Warning methods (e.g., Satriano et al., 2008), but it would easily be fast enough for seismic monitoring, and would have the added advantage of robustness, especially for the larger earthquakes which are those, ultimately, of major interest.

Development of a real-time version of WaveLoc is currently underway as part of NERA (Network of European Research Infrastructures for Earthquake Risk Assessment and Mitigation). The resulting algorithm will be implemented both as a standalone application, and as modules for the two most commonly used seismic monitoring packages: Earthworm (Johnson et al., 1995) and SeisComP (`http://www.seiscomp3.org/`).

6 Conclusions

WaveLoc performs detection and location using continuous stream-like correlation between processed data and a set of reference waveforms. The processing scheme and the choice of reference waveforms depend on the phenomenon to be detected. WaveLoc departs from the traditional methods of earthquake location using phase arrivals and event association, and instead exploits the coherence of the seismic signal across a network. We developed the method by generalizing and expanding the Local Waveform Correlation Event Detection System (LWCEDS) of Withers et al. (1999). In this paper we have illustrated the method via an implementation designed for detecting and locating the aftershocks of the 6 April 2009 L'Aquila $M_w6.1$ earthquake.

The results show that WaveLoc detects nearly 13,500 events during the first 25 days of the L'Aquila aftershock sequence, of which over 7000 could be associated with events picked manually and relocated by the INGV seismic monitoring center (ISIDE catalog). WaveLoc detected over 85% of $M_L2.5-3.5$ events listed by ISIDE, and missed only one of the 50 $M_L > 3.5$ events (98% detection rate). Among the WaveLoc detections with strong correlation values, we found 8 events that were missed by the ISIDE catalog despite being well recorded across the network of permanent stations.

Development of the WaveLoc methodology is ongoing, and it can be adapted to both real-time domains (seismic monitoring) and data-mining (the analysis of large volumes of data without human intervention). Although at the present stage of development the technique cannot produce the high-resolution locations required for detailed understanding of seismically active regions, it has been shown to be a robust and effective event detector and it appears well suited as initial processing module within a procedure for automatic, high resolution event location of large waveform data volumes.

Chapter 4

Directions of current and future research

1 Seismology in Antarctica

My responsibilities as coordinator of the EOST Global Seismological Observatories include running the permanent seismic stations in the Southern Indian Ocean (Crozet, Kerguelen, Amsterdam Island) and Antarctica (Dumont d'Urville), and helping to run the permanent seismic station at Concordia (CCD, also in Antarctica) with Jean-Jacques Lévêque. As "Antarctic people", Jean-Jacques and I could not let the last International Polar Year (2007-2009) go by without proposing a research project. Our project, called "Concordia, Antarctica, Seismic Experiment for the International Polar Year", or CASE-IPY for short, includes partners from IPGP and OMP, was funded by ANR in 2007, and has the logistical support of IPEV (Institut Paul Emile Victor, the French Polar Institute). Section 1.1 contains a brief overview of the project, including a description of the field operations and some preliminary scientific results. Section 1.2 describes preliminary results regarding the characteristics of oceanic microseismic noise at Antarctic coastal stations.

1.1 CASE-IPY

The CASE-IPY project is a part of a larger IPY initiative, the Polar Earth Observing Network (POLENET), which includes contributions from 24 countries, including France, Italy, Australia and the United States. The aim of the POLENET consortium is to investigate polar geodynamics, the Earth's magnetic field, crust, mantle and core structure and dynamics, and systems-scale interactions of the solid Earth, the cryosphere, the oceans and the atmosphere. Activities are focused on deployment

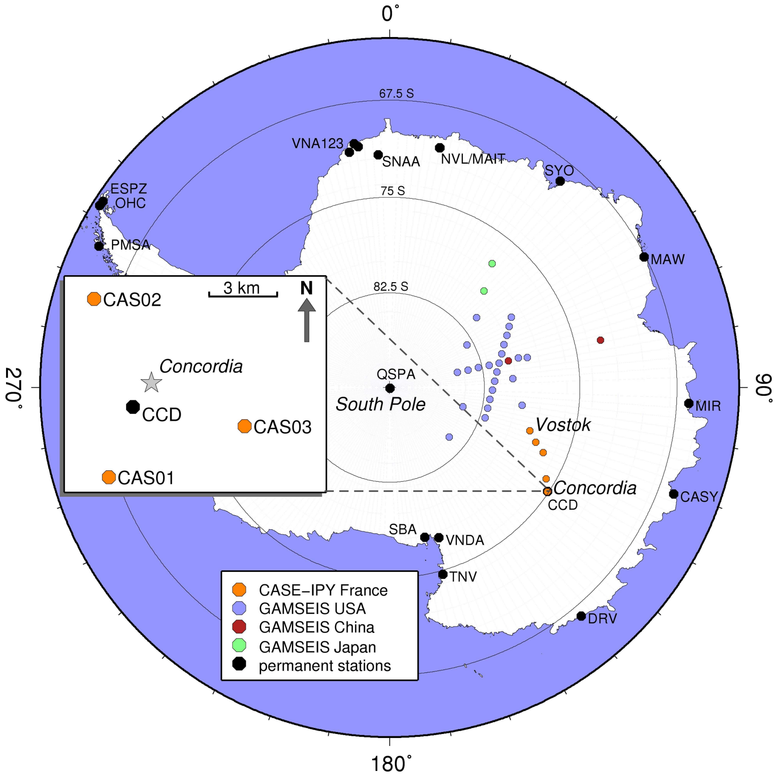

Figure 4.1: Map of CASE-IPY and POLENET stations.

of autonomous observatories at remote sites on the continents and offshore, coordinated with measurements made at permanent station observatories. CASE-IPY aims at deploying 5 to 8 autonomous seismic stations on the East Antarctic Plateau between Concordia (Dome C) and Vostok, and is coordinated with the GAMSEIS (USA-China-Japan) deployment in the region of Gamburtsev mountains. The general purpose of the project is both to dramatically improve the coverage of the plateau to get a better knowledge of the underlying crustal and lithospheric structures, and to record waves traveling through the inner core along polar paths, that are critical for core studies and very rare.

We started by designing and building 3 prototype autonomous seismic stations that we deployed at a distance of 5 km from Concordia during the 2007/2008 summer campaign. The main problems we had to design for were the extreme cold (-30°C in summer to -70°C in winter), and the long Antarctic night (from early May to late August at these latitudes). These stations communicated with Concordia station by radio, and we followed their progress during the winter of 2008. They were powered by 10 lead gel-acid batteries, that are able to function at very low temperatures, and that are recharged by solar panels. During the polar night, the stations went into hibernation, then woke up successfully again the following spring. We kept them

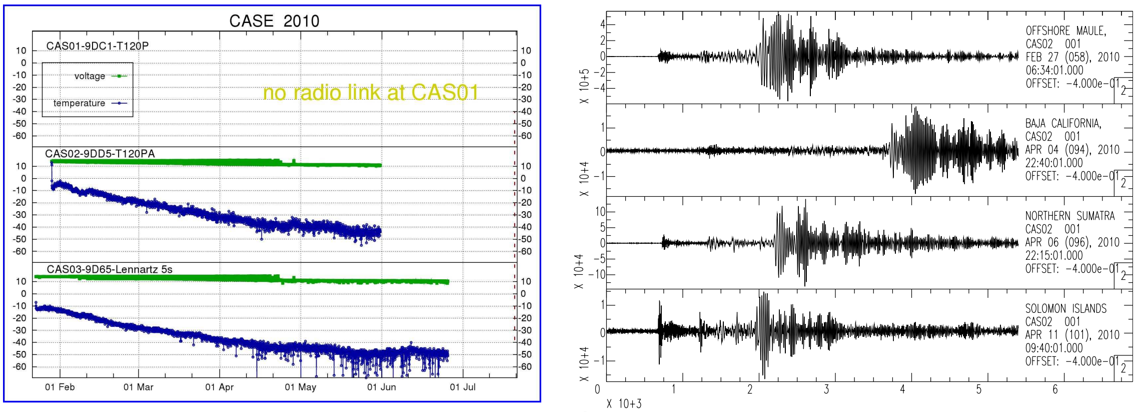

(a) (b)

Figure 4.2: (a) Internal temperature and power supply voltage for the benchmark stations. (b) Teleseismic events recorded at CAS02.

running for a second year (2009) with similar results.

The information we collected from the first year of deployment was fed into the design of the other 5 stations, which were shipped to Antarctica in 2009 after extensive testing (including tests at -70°C). During the 2009-2010 summer campaign, IPEV supplied us with flight time on a Twin Otter light aircraft equipped with skis, thanks to which we were able to install 4 stations in sites along the Concordia–Vostok profile (see Figure 4.1). The field operations were successful thanks to the thorough anticipation of the difficulties inherent in this type of operation, made possible by the experience accumulated over the previous two years, and very detailed planning. We were not able to install the 5th station because of poor weather conditions. This installation is now planned for the 2010-2011 summer campaign, during which all stations will be visited (using terrestrial means this time) to recover the data recorded during 2010.

No information from the 4 more isolated stations is available during winter time, however two of the three autonomous stations close to Concordia (similar in design to the profile stations) communicate with Concordia by radio. We therefore have two benchmark stations that allow us to have some idea of what is happening in the field. These two stations have worked better than expected during 2010: we expected them to go to sleep towards the beginning of May (when the sun sets at Concordia), but one worked up until June 1st, and the other until June 28th (see Figure 4.2a). As an example, Figure 4.2b shows four teleseismic events recorded this year by the benchmark station CAS02.

Exploitation of data from the CASE-IPY experiment has yet to start in earnest, as the first data from the Concordia–Vostok profile will only be available in 2011.

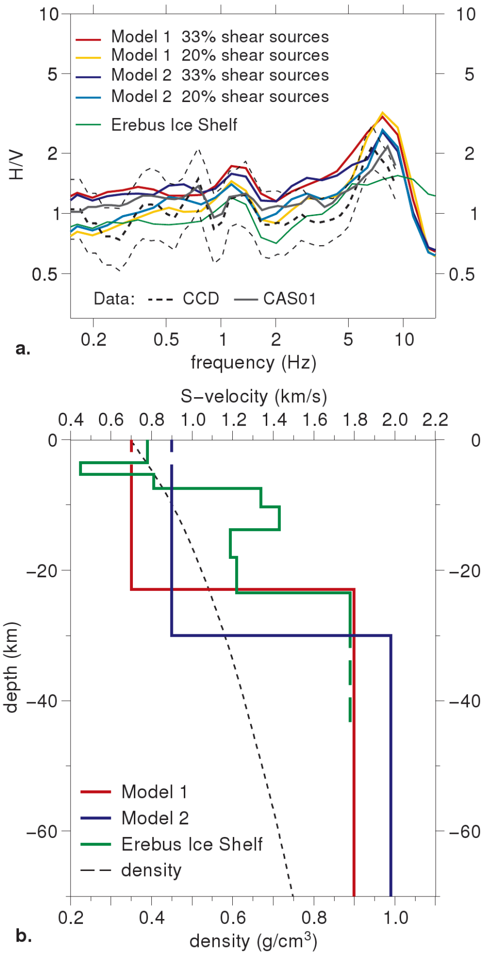

Figure 4.3: (a) Fit of the H/V spectral ratios at the Dome C stations CCD (dashed, with standard deviation) and at CAS01 (grey line), with two different models and two different compositions of the noise. Also shown is the result obtained for an Erebus ice shelf model. (b) S-wave velocity models used in (a) (scale at the top, model 1 preferred), and density profile at Concordia (L. Arnaud, personal communication 2010, scale at the bottom). Lévêque et al. (2010, Fig. 6)

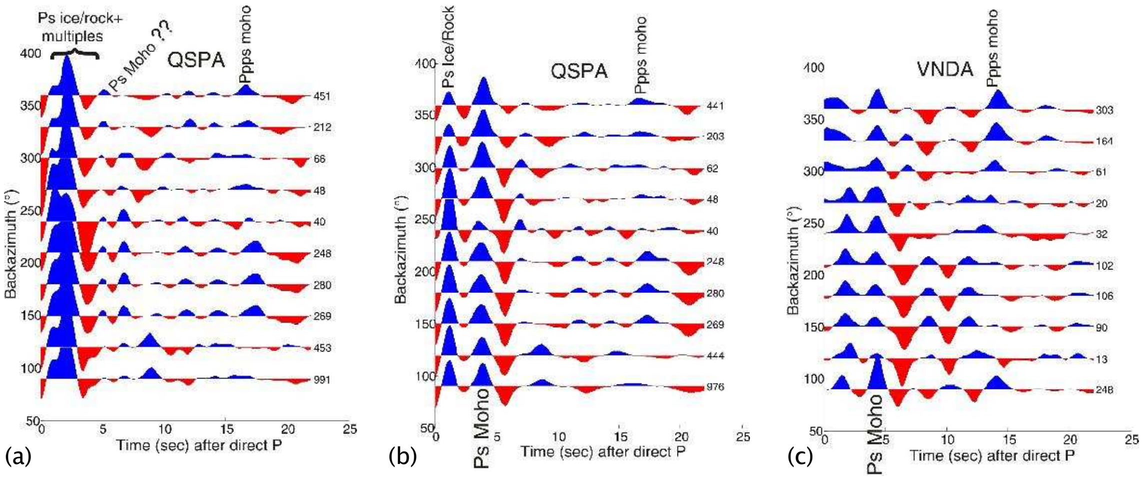

Figure 4.4: Receiver function results: (a) raw receiver functions at QSPA; (b) receiver functions at QSPA with ice effect removed; (c) receiver functions at VNDA (rock station).

Preliminary work on the data from the prototype stations near Concordia in 2008 and 2009, combined with data from the permanent station at Concordia (CCD), has confirmed the lack of local seismicity. In collaboration with Annie Souriau, co-investigator for CASE-IPY, we have recently published a seismic model of the snow and ice structure near Concordia obtained from these data using H/V methods (see Lévêque et al., 2010, and Figure 4.3). In preparation for exploiting the full data-set, Gerard Wittlinger and Véronique Fara (both co-investigators for CASE-IPY), have started exploring receiver-functions from Antarctic stations, which are unusual in nature because of reverberations in the approximately 3 km thick ice layer that tend to block out the signal from the Moho and other crustal layers. They have succeeded in developing an anti-ice filter, essentially by first understanding the detailed seismic structure of the ice-layer itself through higher frequency receiver function analyses. Preliminary results are illustrated in Figure 4.4, that shows raw receiver functions at South Pole (QSPA, on ∼2.5 km of ice, Figure 4.4a), the receiver functions at the same station after removing the ice reverberations (Figure 4.4b), and those at a station installed directly on rock (VNDA, Figure 4.4c). The similarity between the signals at VNDA and the filtered signals from QSPA illustrates the efficacy of the anti-ice filter, which allows us to recover the reflector corresponding to the Moho.

Field operations will continue on CASE-IPY for at least another two years. We hope to recover the stations and all the remaining data by January 2013. We shall continue to exploit the data locally and with our POLENET partners until 2015, after which they will be distributed to the scientific community at large.

We currently expect to concentrate on the ice-structure between Concordia and Vostok, receiver function studies of the crust and lithosphere, surface wave studies in collaboration with other POLENET partners, and the retrieval and exploitation of core-phases for studies of inner core structure and differential rotation.

1.2 Seismic Noise

Ocean microseismic noise in the 1–20 s period band is a well-known and recently much studied phenomenon. Primary microseisms (10-20 s period) are generated when ocean gravity waves reach shallow water near the coast and interact with the sloping seafloor (e.g. Hasselmann, 1963). These seismic waves have periods similar to the incident ocean gravity waves. The secondary microseisms are generated by the interaction of two ocean gravity waves of similar periods that travel in opposite directions. When these ocean waves meet, they generate standing pressure fluctuations at the ocean bottom through a nonlinear mechanism (Longuet-Higgins, 1950). The pressure fluctuations have half the period of the ocean waves and are the source of the secondary microseisms. Recently, modeling of the deep ocean non-linear wave-wave interaction in a source region between the Labrador Sea and Iceland showed an excellent agreement with the secondary microseism amplitude recorded by stations in North America and Western Europe (Kedar et al., 2007), demonstrating the validity of Longuet-Higgins's theory.

Microseism amplitude is generally higher during local winter (Stutzmann et al., 2009) because nearby oceans are stormier in winter than in summer. In Antarctica the opposite is observed: microseism amplitude is attenuated during local winter for both primary and secondary microseisms. This seems to be due to the presence of the sea ice floe. Primary microseisms may be attenuated because the ice floe impedes direct coupling between ocean gravity waves and the sloping seafloor. Secondary microseisms are generated in the open ocean. Their attenuation may be due to the lack of coastal reflection of ocean gravity waves, which then reduces the probability of occurrence of ocean waves traveling in opposite directions in the open ocean.

The Stutzmann et al. observation of the effect of ice floe on microseismic noise in Antarctica was made only for Dumont d'Urville station (DRV). Mélanie Grob (a recent PhD at EOST), two first-year Masters students, Lise Retailleau and Simon Boyat, and I have extended the analysis to 10 stations in Antarctica for which data are available from the IRIS (Incorporated Research Institutes for Seismology) and GEOSCOPE data centers for the decade 2000-2009. Figure 4.5 shows yearly amplitude variations of daily seismic noise spectra for the 10 stations, and confirms

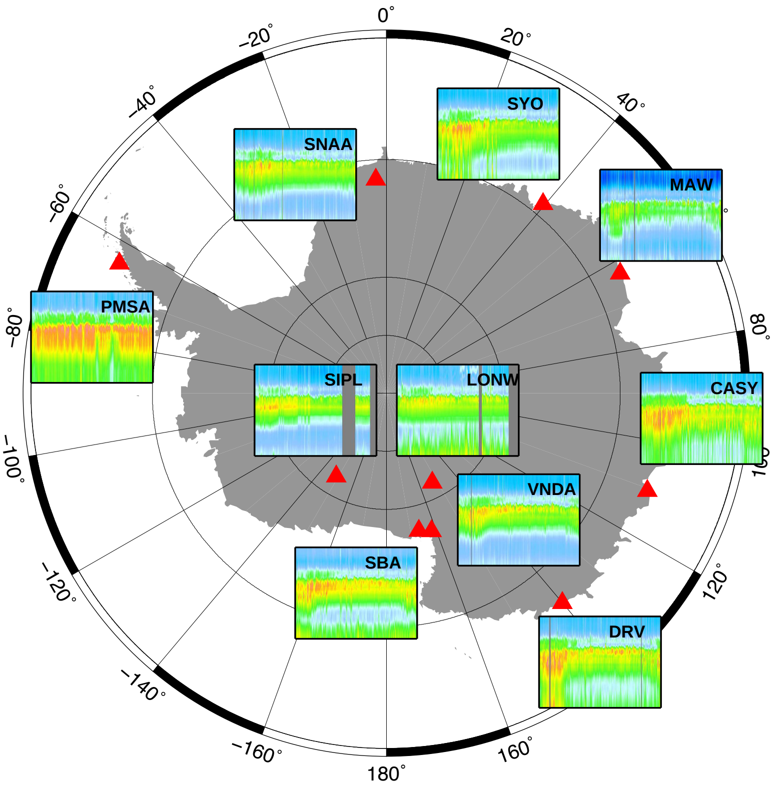

Figure 4.5: Map of Antarctica with the locations of the 10 stations analyzed in this study (red triangles). The images near each station represent the amplitude variations of daily seismic noise spectra over the period 0.1–80 s for a whole year (PMSA 2008, SNAA 2004, SYO 2002, MAW 2008, CASY 2008, VNDA 2006, LONW 2009, SIPL 2009, DRV 2008, SBA 2004). The amplitude values are given by the color-bar in Figure 4.6 (gray color corresponds to lack of data).

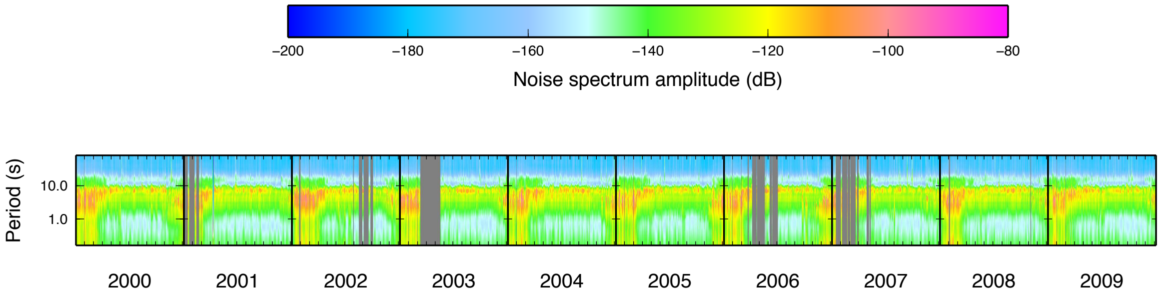

Figure 4.6: Annual seismic noise spectra for Dumont d’Urville station (DRV) from 2000 to 2009. The amplitude values are given by the color-bar (gray color corresponds to lack of data).

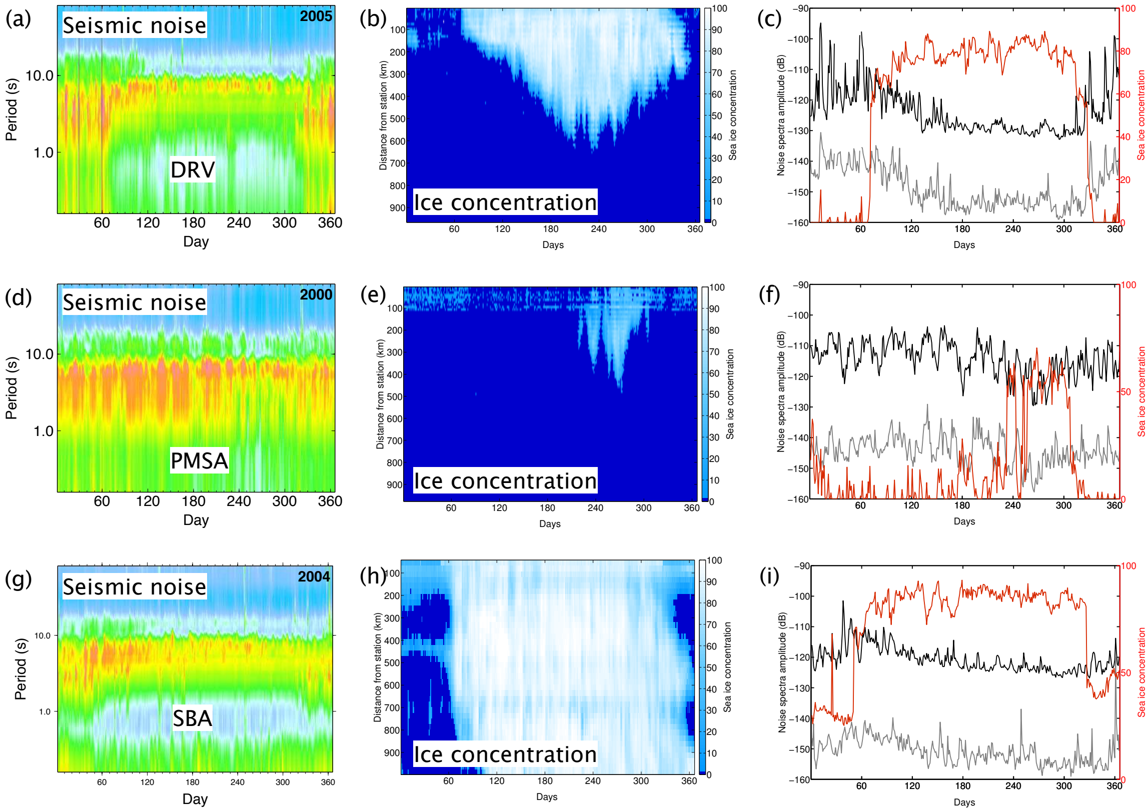

Figure 4.7: Detailed analysis for DRV (a)-(c), PMSA (d)-(f) and SBA (g)-(i). (a),(d),(g) Annual seismic noise spectra. (b),(e),(h) Evolution of sea ice concentration as a function of distance from each station for over the year. (c),(f),(i) Comparison of seismic noise with ice concentration: grey = average noise spectra for primary microseisms (10–20 s), black = average noise spectra for secondary microseisms (3–6 s), red = sea ice concentration nearest to the coast and the station.

that the noise spectra at all stations are lower during local winter. We have been able to repeat this observation over a decade (see Figure 4.6), confirming that the pattern of attenuation in local winter is repeated over the years.

In order to confirm the correlation between microseismic noise attenuation and ice floe presence, we have compared in Figure 4.7 the annual trends of primary and secondary microseism amplitude and the sea ice concentration. Microseism amplitude and coastal sea-ice concentration are very nicely anti-correlated. The differences in the microseismic amplitude variations between DRV and PMSA are caused by the different durations of sea-ice presence: March–November at DRV and September only at DRV.

These preliminary analyses confirm the main observation: that the presence of ice-floe attenuates seismic noise at coastal stations in Antarctica. Many details remain to be investigated. What happens to the ocean gravity wave when it encounters the ice floe? Where does its energy go? Does the energy go into flexure of the sea ice? What about the ocean-bottom coupling that causes the secondary microseisms? Secondary microseisms generated in the open, non-frozen ocean should not be influenced by ice-floe presence. Can we use the ice's tendency to prevent efficient coastal reflections to estimate the relative strengths of open-ocean and near-coastal secondary microseism generation? Can we use polarization analysis, like Stutzmann et al. (2009), to help pinpoint the origin of summer and winter microseismic noise?

2 Future directions of research

Over the next few years, I shall continue to be active on a number of fronts. I am a minor co-investigator in the PYROPE project (ANR, Sébastien Chevrot), in the DoRA project (ANR, Cécile Doubre), and in the soon-to-be-submitted Lunette project (NASA, Philippe Lognonné). I shall, of course, continue work on the CASE-IPY project through the end of the field operation phase and throughout the data exploitation phase. I also hope to continue my investigations on the effect of grounded and/or floating ice on the transmission of microseismic noise. However, the main thrust of my research over the next 5 years will be the consolidation and further development of WaveLoc, in continued collaboration with Alberto Michelini at INGV, and probably also with Jocelyn Guilbert at CEA.

We currently envisage three main axes of development and application of the WaveLoc method: improvements to the core of the method, such as those suggested in the discussion section of Chapter 3; a real-time implementation for seismic monitoring applications; and adaptation to high resolution locations and data mining. I plan to submit an ANR proposal to fund part of these developments, principally to recruit a PhD student and/or a post-doctoral student.

2.1 WaveLoc core development

As discussed in Chapter 3, WaveLoc is a relatively robust procedure for detecting and locating chosen seismic phenomena. There are still a number of improvements to be made to the system to increase its robustness and the accuracy of its locations. Amongst these are: extending the analysis to three-component data; using multiple waveform processing methods, which would be differently sensitive to P- and S-wave arrivals; and detecting occurrences of teleseismic or regional events by taking into account the 2D shape of the stacked correlation maps, and the shape of the $S_{\max}$ peaks.

2.2 WaveLoc in real-time

WaveLoc was designed specifically to work on continuous data streams, with the idea of developing a real-time waveform-based detector and locator of earthquakes or other seismic phenomena to be used alongside more traditional methods in seismic monitoring centers. For real-time operation, incoming data-streams would be pre-processed on the fly, and cross-correlated with the reference waveforms exactly as depicted in Fig. 3.2, thereby producing the 2D correlation maps that could be displayed directly. The detector algorithm described in Section 2.4 would have to be modified to work in near-real time.

In Section 2.1, we have shown that for local and near-regional operation, and in the absence of data latency, WaveLoc can obtain a detection and preliminary location within 20-30 s of the event origin time, depending essentially on station coverage. This time could be shortened slightly by considering only very short epicentral distances in the construction of the reference-waveforms, but this would lead to a reduced set of stations on which to test data coherence, and would reduce the robustness of the method. A robust real-time implementation of WaveLoc would probably be too slow to compete with dedicated Earthquake Early Warning methods (e.g., Satriano et al., 2008), but it would easily be fast enough for seismic monitoring, and would have the added advantage of robustness, especially for the larger earthquakes which are those, ultimately, of major interest.

Development of a real-time version of WaveLoc is currently underway as part of NERA (Network of European Research Infrastructures for Earthquake Risk Assessment and Mitigation). The resulting algorithm will be implemented both as a standalone application, and as modules for the two most commonly used seismic monitoring packages: Earthworm (Johnson et al., 1995) and SeisComP (`http://www.seiscomp3.org/`). Three probable test-beds for the real-time version will be the INGV and CEA seismic monitoring centers, and the EOST real-time data center.

2.3 WaveLoc and data mining

In its current implementation, WaveLoc can readily be applied to data-mining applications, as it allows for the rapid processing of very large volumes of waveform data, such as those acquired by temporary networks. The manpower required for the analysis of such large volumes of data is often prohibitive. In this context, WaveLoc can provide robust, rapid and cost-effective detection and preliminary location of the phenomena of interest, even on a very large scale (e.g. an entire national network).

As we have seen above, WaveLoc is currently unable to produce the high-resolution locations that are ultimately required for detailed studies of seismically active regions. The planned improvements to the WaveLoc method mentioned above will undoubtedly improve the accuracy of its locations, but this improvement may not be sufficient for truly high-resolution applications.

Following the lead of Waldhauser and Schaff (2008) and Waldhauser (2009), we have started to develop a modular automated procedure that uses WaveLoc as an event detector, then goes back to the corresponding original seismograms to perform waveform picking followed by event relocation and magnitude estimation. We envisage eventually performing waveform picking using high-resolution three-component phase pickers and/or differential time pickers based on waveform correlation. Locations would then be performed using traditional single-event or double difference methods. Preliminary results from this procedure, using a simple kurtosis-based picking algorithm and the NLLOC non-linear location (Lomax et al., 2000), are promising, especially regarding the improvement of WaveLoc origin-times (Hector, 2010). CEA is very excited about this part of the project, and has agreed to co-fund a PhD studentship on the subject.

My contribution to the PYROPE project will be high-resolution data-mining of seismicity from the full dataset of permanent and portable stations. I have also received expressions of interest for testing the WaveLoc data-mining capabilities in geothermal applications (e.g. microseismicity at Soultz) and volcanic observatories (Piton la Fournaise). If WaveLoc can be shown to work in these two fields, specific real-time versions for monitoring geothermally induced seismicity and volcanic seismicity may be envisaged. Other fields of interest for application of WaveLoc in a data-mining sense are the search for volcanic and/or non-volcanic tremor episodes, and specific non-standard sources (this latter is of great interest to CEA). A very high-frequency application to finite sources studies is also envisaged (this would be somewhat similar to migration approaches).

References

A. Adams, R. Brazier, A.A. Nyblade, A. Rodgers, and A. Al-Amri. Source parameters for moderate earthquakes in the Zagros mountains with implications for the depth extent of seismicity. *B. Seismol. Soc. Am.*, 99(3):2044–2049, 2009.

M. Alavi. Tectonic map of the Middle East, Geological Survey of Iran, 1991. Scale 1:5,000,000.

R.V. Allen. Automatic phase pickers: their present use and future prospects. *B. Seismol. Soc. Am.*, 72:S225–S242, 1982.

R.V. Allen. Automatic earthquake recognition and timing from single traces. *B. Seismol. Soc. Am.*, 68:1521–1531, 1987.

Bettina P Allmann and Peter M Shearer. A high-frequency secondary event during the 2004 parkfield earthquake. *Science*, 318(5854):1279–1283, 2007.

Alessandro Amato, L Badiali, M Cattaneo, A Delladio, F Doumaz, and Francesco Mele. The real-time earthquake monitoring system in italy. *Geosciences*, 4:70–75, 2006.

R. Aster and C. Rowe. Automatic phase pick refinement and similar event association in large seismic datasets. In C. H. Thurber and N. Rabinowitz, editors, *Advances in Seismic Event Location*, pages 231–263. Kluwer, Dordrecht, Netherlands, 2000.

Emmanuel Auger, Luca D'Auria, Marcello Martini, Bernard Chouet, and Phillip Dawson. Real-time monitoring and massive inversion of source parameters of very long period seismic signals: An application to stromboli volcano, italy. *Geophys. Res. Lett.*, 33:–, 2006.

C. Bai and B. L. N. Kennett. Automatic phase-detection and identification by full use of a single three-component broadband seismogram. *B. Seismol. Soc. Am.*, 90:187–198, 2000.

C.Y. Bai and B.L.N. Kennett. Phase identification and attribute analysis of broadband seismograms at far-regional distances. *J. Seismol.*, 5:217–231, 2001.

C. Baker, J. Jackson, and K. Priestley. Earthquakes on the Kazerun Line in the Zagros Mountains of Iran: Strike–slip faulting within a fold–and–thrust belt. *Geophys. J. Int.*, 115:41–61, 1993.

Teresa Baker, Robert Granat, and Robert W Clayton. Real-time earthquake location using kirchhoff reconstruction. *Bulletin of the Seismological Society of America*, 95(2):699–707, 2005.

G. Barruol, D. Suetsugu, H. Shiobara, H. Sugioka, S. Tanaka, G.H.R. Bokelmann, F.R. Fontaine, and D. Reymond. Mapping upper mantle flow beneath French Polynesia from broadband ocean bottom seismic observations. *Geophy. Res. Lett.*, 36, 2009.

G. Barruol et al. PLUME investigates the South Pacific Superswell. *EOS Trans. AGU*, 83:511–514, 2002.

E. Beucler, E. Stutzmann, and J.-P. Montagner. Surface wave higher-mode phase velocity measurements using a roller-coaster-type algorithm. *Geophys. J. Int.*, 155:289–307, 2003.

L. Boschi, J.P. Ampuero, D. Peter, P.M. Mai, G. Soldati, and D. Giardini. Petascale computing and resolution in global seismic tomography. *Phys. Earth Planet. Interiors*, 163:245–250, 2007.

Justin R Brown, Gregory C Beroza, and David R Shelly. An autocorrelation method to detect low frequency earthquakes within tremor. *Geophys. Res. Lett.*, 35:–, 2008.

E. Burov. The equivalent elastic thickness (T-e), seismicity and the long-term rheology of continental lithosphere: Time to burn-out "creme brulee"? Insights from large-scale geodynamic modeling. *Tectonophysics*, 484:4–26, 2010.

S.C. Cande, J.L. LaBrecque, R.L. Larson, W.C. Pitmann, X. Golovchenko, and W.F. Haxby. Magnetic lineations of the world's ocean basins, 1989. Map Series.

Y. Capdeville. An efficient Born normal mode method to compute sensitivity kernels and synthetic seismograms in the Earth. *Geophys. J. Int.*, 163:639–646, 2005.

Y. Capdeville, E. Chaljub, J.P. Vilotte, and J.P. Montagner. Coupling the spectral element method with a modal solution for elastic wave propagation in global earth models. *Geophys. J. Int.*, 152:34–67, 2003.

M. Cara and J.J. Lévêque. Waveform inversion using secondary observables. *Geophy. Res. Lett.*, 14:1046–1049, 1987.

P. Chen, L. Zhao, and T. H. Jordan. Full 3D tomography for the crustal structure of the Los Angeles region. *B. Seismol. Soc. Am.*, 97:1094–1120, 2007.

C Chiarabba, Alessandro Amato, M Anselmi, P Baccheschi, I Bianchi, M Cattaneo, G Cecere, L Chiaraluce, M G Ciaccio, P De Gori, G De Luca, Massimo Di Bona, R Di Stefano, L Faenza, A Govoni, L Improta, F P Lucente, A Marchetti, L Margheriti, Francesco Mele, Alberto Michelini, G Monachesi, M Moretti, M Pastori, N Piana Agostinetti, Davide Piccinini, P Roselli, D Seccia, and Luisa Valoroso. The 2009 L'Aquila (central Italy) Mw6.3 earthquake: Main shock and aftershocks. *Geophys. Res. Lett.*, 36, 2009.

G. Choubert and A. Faure-Muret. Geological world atlas, UNESCO, 1976. Scale 1:10,000,000.

Antonella Cirella, Alessio Piatanesi, Massimo Cocco, Elisa Tinti, Laura Scognamiglio, Alberto Michelini, Anthony J Lomax, and Enzo Boschi. Rupture history of the 2009 L'Aquila (Italy) earthquake from non-linear joint inversion of strong motion and GPS data. *Geophys. Res. Lett.*, 36, 2009.

Jon F Claerbout. Toward a unified theory of reflector mapping. *Geophysics*, 36(3): 467–481, 1971.

A. Curtis, J. Trampert, R. Snieder, and B. Dost. Eurasian fundamental mode surface wave phase velocities and their relationship with tectonic structures. *J. Geophys. Res.*, 103:26,919–26,947, 1998.

F. Dahlen and A. Baig. Fréchet kernels for body wave amplitudes. *Geophys. J. Int.*, 150:440–446, 2002.

F. A. Dahlen, S.-H. Hung, and G. Nolet. Fréchet kernels for finite-frequency traveltimes—I. Theory. *Geophys. J. Int.*, 141:157–174, 2000.

F.A. Dahlen and Y. Zhou. Surface-wave group-delay and attenuation kernels. *Geophys. J. Int.*, 165:545–554, 2006.

E. Debayle. SV-wave azimuthal anisotropy in the Australian upper mantle: preliminary results from automated Rayleigh waveform inversion. *Geophys. J. Int.*, 137:747–754, 1999.

E. Debayle and M. Sambridge. Inversion of massive surface wave data sets: model construction and resolution assessment. *J. Geophys. Res.*, 109, 2004. 10.1029/2003JB002652.

A.M. Dziewonski, T.A. Chou, and J.H. Woodhouse. Determination of earthquake source parameters from waveform data for studies of global and regional seismicity. *J. Geophys. Res.*, 86:2825–2852, 1981.

Paul S Earle and Peter M Shearer. Characterization of global seismograms using an automatic-picking algorithm. *Bulletin of the Seismologica Society of America*, 84 (2):366–376, 1994a.

P.S. Earle and P.M. Shearer. Characterization of global seismograms using an automatic picking algorithm. *B. Seismol. Soc. Am.*, 84:366–376, 1994b.

G. Ekström. Global detection and location of seismic sources using surface waves. *B. Seismol. Soc. Am.*, 94(4):1201–1212, 2006.

G. Ekström and A.M. Dziewonski. The unique anisotropy of the Pacific upper mantle. *Nature*, 394:168–172, 1998.

G. Ekström, J. Tromp, and E.W.F. Larson. Measurements and global models of surface wave propagtaion. *J. Geophys. Res.*, 102:8137–8157, 1997.

Goran Ekstrom, Meredith Nettles, and Geoffrey A; MacKenzie Abers. Glacial earthquakes. *Science*, 302(5645):622–624, 2003.

E.R. Engdahl, R. van der Hilst, and R. Bulland. Global teleseismic earthquake relocation with improved travel times and procedures for depth determination. *B. Seismol. Soc. Am.*, 88:722–743, 1998.

FDSN. Seed reference manual. *Incorporated Research Institutions for Seismology (IRIS).*, pages 1–212, Mar 2006.

D.W. Forsyth. The evolution of the upper mantle beneath mid-ocean ridges. *Tectonophysics*, 38:89–118, 1977.

Dirk Gajewski and Ekkehart Tessmer. Reverse modelling for seismic event characterization. *Geophysical Journal International*, 163(1):276–284, 2005.

O. Gauthier, J. Virieux, and A. Tarantola. Two-dimensional nonlinear inversion of seismic waveforms: Numerical results. *Geophysics*, 51:1387–1403, 1986.

S Gentili and Alberto Michelini. Automatic picking of p and s phases using a neural tree. *Journal of Seismology*, 10(1):39–63, 2006.

A. Haghipour and A. Aghanabati. Geological map of Iran, Ministry of Mines and Metals, Geological Survey of Iran, 1989. Scale: 1:2,500,00.

N. Harmon, D.W. Forsyth, and C. Weeraratne. Thickening of young Pacific lithosphere from high-resolution Rayleigh wave tomography: A test of the conductive cooling model. *Earth Planet. Sc. Lett.*, 278:96–106, 2009.

K. Hasselmann. A statistical analysis of the generation of microseisms. *Rev. Geophys.*, 1:177–209, 1963.

Basile Hector. Towards detection and high resolution location of regional earthquakes using continuous waveforms. Master's thesis, Université de Strasbourg, Jun 2010.

C. Houser, G. Masters, and G. Laske. Shear and compressional velocity models of the mantle from cluster analysis of long-period waveforms. *Geophys. J. Int.*, 174: 195–212, 2008.

Satoshi Ide, Gregory C Beroza, David R Shelly, and Takahiko Uchide. A scaling law for slow earthquakes. *Nature*, 447(7140):76–79, 2007.

Miaki Ishii, Peter M Shearer, Heidi Houston, and John E Vidale. Extent, duration and speed of the 2004 Sumatra-Andaman earthquake imaged by the Hi-Net array. *Nature*, 435(7044):933–936, 2005.

J.A. Jackson, D. McKenzie, K. Priestley, and B. Emmerson. New views on the structure and rheology of the lithosphere. *J. Geol. Soc. London*, 165:453–465, 2008.

C Johnson, A Bittenbinder, B Bogaert, L Dietz, and W Kohler. Earthworm: a flexible approach to seismic network monitoring. *IRIS Newsletter*, 14:1–4, 1995.

CE Johnson, AG Lindh, and B Hirshorn. Robust regional phase association. Technical Report 94-621, 1994.

K. Kadinsky-Cade, M. Barazangi, J. Oliver, and B. Isacks. Lateral variations in high-frequency seismic wave propagationat regional distances across the Turkish and Iranian plateaus. *J. Geophys. Res.*, 86:9377–9396, 1981.

E. Kaminski and N.M. Ribe. Timescales for the evolution of seismic anisotropy in mantle flow. *Geochem. Geophys. Geosyst.*, 3(8), 2002. 10.1029/2001GC000222.

Honn Kao and Shao-Ju Shan. The source-scanning algorithm: mapping the distribution of seismic sources in time and space. *Geophysical Journal International*, 157(2):589–594, 2004.

Honn Kao and Shao-Ju Shan. Rapid identification of earthquake rupture plane using source-scanning algorithm. *Geophysical Journal International*, 168(3):1011–1020, 2007.

S. Kedar, M. Longuet-Higgins, F. Webb, N. Graham, R. Clayton, and C. Jones. The origin of deep ocean microseisms in the North Atlantic Ocean. *Proc. R. Soc. A.*, 464:777–793, 2007.

M. Keskin, J.A. Pearce, and J.G. Mitchell. Volcano-stratigraphy and geochemistry of collision-related volcanism on the Erzurum–Kars Plateau, northeastern Turkey. *J. Volcanol. Geotherm. Res.*, 85(1–4):355–402, 1998.

D. Komatitsch and J. Tromp. Spectral-element simulations of global seismic wave propagation — i. validation. *Geophys. J. Int.*, 149:390–412, 2002a.

D. Komatitsch and J. Tromp. Spectral-element simulations of global seismic wave propagation — ii. three-dimensional models, oceans, rotation and self-gravitation. *Geophys. J. Int.*, 150:303–318, 2002b.

D. Komatitsch and J.-P. Vilotte. The spectral element method: An efficient tool to simulate the seismic response of 2D and 3D geological structures. *B. Seismol. Soc. Am.*, 88:368–392, 1998.

D. Komatitsch, J. Ritsema, and J. Tromp. The spectral-element method, Beowulf computing, and global seismology. *Science*, 298:1737–1742, 2002.

L Kuperkoch, Thomas Meier, J Lee, W Friederich, and EGELADOS Working Group. Automated determination of p-phase arrival times at regional and local distances using higher order statistics. *Geophysical Journal International*, 2010. doi: 10.1111/j.1365-246X.2010.04570.x.

Carène Larmat, Jean-Paul Montagner, Mathias Fink, Yann Capdeville, Arnaud Tourin, and Eric Clévédé. Time-reversal imaging of seismic sources and application to the great Sumatra earthquake. *Geophys. Res. Lett.*, 33, 2006.

G. Laske and G. Masters. Constraints on global phase velocity maps from long-period polarization data. *J. Geophys. Res.*, 101:16,059–16,075, 1996.

J. F. Lawrence and P. M. Shearer. Imaging mantle transition zone thickness with *SdS-SS* finite-frequency sensitivity kernels. *Geophys. J. Int.*, 174:143–158, 2008.

J. F. Lawrence, P. M. Shearer, and G. Masters. Mapping attenuation beneath North America using waveform cross-correlation and cluster analysis. *Geophy. Res. Lett.*, 33:L07315, 2006. doi: 10.1029/2006GL025813.

S. Lebedev, G. Nolet, T. Meier, and R. D. van der Hilst. Automated multimode inversion of surface and *S* waveforms. *Geophys. J. Int.*, 162:951–964, 2005.

W H K Lee and S W Stewart. *Principles and Applications of microearthquake networks*. 1981.

F.G. Lemoine et al. The NASA and DMA joint geopotential model. *EOS Trans. AGU*, 1996. Fall Meet. Suppl.

J.J. Lévêque, A. Maggi, and A. Souriau. Seismological constraints on ice properties at dome c, antarctica, from h/v measurements. *Antarctic Science*, 2010.

A.L. Levshin and M.H. Ritzwoller. Automated detection, extraction, and measurement of regional surface waves. *Pure App. Geophys.*, 158:1531–1545, 2001.

Hongyi Li, Alberto Michelini, Lupei Zhu, Fabrizio Bernardi, and Matteo Spada. Crustal Velocity Structure in Italy from Analysis of Regional Seismic Waveforms. *Bulletin of the Seismological Society of America*, 97(6):2024–2039, 2007. doi: 10.1785/0120070071.

X.D. Li and T. Tanimoto. Waveforms of long-period body waves in a slightly aspherical earth model. *Geophys. J. Int.*, 112:92–102, 1993.

Q. Liu and J. Tromp. Finite-frequency kernels based on adjoint methods. *B. Seismol. Soc. Am.*, 96:2383–2397, 2006.

Q. Liu and J. Tromp. Finite-frequency sensitivity kernels for global seismic wave propagation based upon adjoint methods. *Geophys. J. Int.*, 174:265–286, 2008.

R.B. Lohman and M. Simons. InSAR–constrained locations of earthqukes in the Zagros mountains of Iran. *EOS Trans. AGU*, 83(47), 2002. Fall Meet. Suppl.

A. Lomax, J. Virieux, P. Volant, and C. Berge. Probabilistic earthquake location in 3D and layered models: Introduction of a Metropolis-Gibbs method and comparison with linear locations. In C.H. Thurber and N. Rabinowitz, editors, *Advances in Seismic Event Location*, pages 101–134. Kluwer, Amsterdam, 2000.

M. Longuet-Higgins. A theory of the origin of microseisms. *Philos. T. Roy. Soc.*, 243(1–35), 1950.

A. Maggi and A. Michelini. Rapid waveform earthquake location in Italy. *Geophysical Research Abstracts*, 11, 2009a. EGU2009-4977.

A. Maggi and A. Michelini. Continuous waveform data stream analysis: Detection and location of the L'Aquila earthquake sequence. *Eos Trans. AGU*, 90(52), 2009b. Fall Meet. Suppl., Abstract U12A-01.

A. Maggi and K. Priestley. Surface waveform tomography of the Turkish Iranian plateau. *Geophys. J. Int.*, 160(3):1068–1080, 2005.

A. Maggi, J.A. Jackson, D. McKenzie, and K. Priestley. Earthquake focal depths, effective elastic thickness, and the strength of the continental lithosphere. *Geology*, 28:495–498, 2000a.

A. Maggi, J.A. Jackson, K. Priestley, and C. Baker. A re–assessment of focal depth distribution in southern Iran, the Tien Shan and northern India: Do earthquakes really occur in the continental mantle? *Geophys. J. Int.*, 143:629–661, 2000b.

A. Maggi, K. Priestley, and J. Jackson. Focal depths of moderate and large size earthquakes in Iran. *J. Seismology and Earthquake Engineering*, 4(2-3):1–10, 2002.

A. Maggi, E. Debayle, G. Barruol, and K. Priestley. Multi-mode surface waveform tomography of the Pacific Ocean: a close look at the lithospheric cooling signature. *Geophys. J. Int.*, 166:1384–1397, 2006a.

A. Maggi, E. Debayle, and K. Priestley. Azimuthal anisotropy of the Pacific Ocean upper mantle. *Earth Planet. Sc. Lett.*, 250:53–71, 2006b.

A. Maggi, L. Rivera, and D. Rouland. Detailed seismicity of the southern indian ocean. *EGU*, 2007.

A. Maggi, C. Tape, M. Chen, D. Chao, and J. Tromp. An automated time-window selection algorithm for seismic tomography. *Geophys. J. Int.*, 178:257–281, 2009.

N.S. Manaman and H. Shomali. Upper mantle S-velocity structure and Moho depth variations across Zagros belt, Arabian–Eurasian plate boundary. *Physics of the Earth and Planetary Interiors*, 180:92–103, 2010.

H. Marquering, F.A. Dahlen, and G. Nolet. Three-dimensional sensitivity kernels for finite-frequency traveltimes: the banana-doghnut paradox. *Geophys. J. Int.*, 137:805–815, 1999.

S Mazza, Marco Olivieri, A G Mandiello, and P Casale. The mediterranean broad band seismographic network. pages –, 2005.

T.V. McEvilly and E.L. Majer. ASP: An Automated Seismic Processor for microearthquake networks. *Bulletin of the Seismologica Society of America*, 72(1): 303–325, 1982.

D. McKenzie. Finite deformation during fluid flow. *Geophys. J. R. Astr. Soc.*, 58: 689–715, 1979.

George A McMechan, J H Luetgert, and HAROLD M Mooney. Imaging of earthquake sources in Long Valley Caldera, California, 1983. *Bulletin of the Seismological Society of America*, 75(4):1005–1020, 1985.

M.K. McNutt and K.M. Fischer. The South Pacific superswell. In B.H. Keating, P. Fryer, R. Batiza, and G.W. Boehlert, editors, *Seamounts, Islands, and Atolls*, volume 43 of *Geophysical Monograph*, pages 25–34. American Geophysical Union, Washington, D.C., 1987.

C. Mégnin and B. Romanowicz. The three-dimensional shear velocity structure of the mantle from the inversion of body, surface and higher-mode waveforms. *Geophys. J. Int.*, 143:709–728, 2000.

J Milne. *Earthquakes and Other Earth Movements.* 1886.

J.-P. Montagner. Upper mantle low anisotropy channels below the Pacific Plate. *Earth Planet. Sc. Lett.*, 202:263–274, 2002.

R. Montelli, G. Nolet, F. A. Dahlen, G. Masters, E. R. Engdahl, and S.-H. Hung. Finite-frequency tomography reveals a variety of plumes in the mantle. *Science*, 303:338–343, 2004.

R.D. Müller, W.R. Roest, J.-Y. Royer, L.M. Gahagan, and J.G. Sclater. Digital isochrons of the world's ocean floor. *J. Geophys. Res.*, 102(B2):3211–3214, 1997.

Naoki Suda and Ryoko Nakata and Takehiro Kusumi. An automatic monitoring system for nonvolcanic tremors in southwest japan. *J. Geophys. Res.*, 114, 2009.

S E J Nippress, A Rietbroc, and A E Heath. Optimized automatic pickers: application to the ancorp data set. *Geophysical Journal International*, 2010. doi: 10.1111/j.1365-246X.2010.04531.x.

C.E. Nishimura and D.W. Forsyth. The anisotropic structure of the upper mantle in the Pacific. *Geophys. J.*, 96:203–229, 1989.

G. Nolet. Partitioned waveform inversion ant two-dimensional structure under the Network of Autonomously Recording Seismographs. *J. Geophys. Res.*, 95:8499–8512, 1990.

Kazushige Obara. Nonvolcanic deep tremor associated with subduction in southwest japan. *Science*, 296(5573):1679–1681, 2002.

M. Panning and B. Romanowicz. A three-dimensional radially anisotropic model of shear velocity in the whole mantle. *Geophys. J. Int.*, 167:361–379, 2006.

R.L. Parker and D.W. Oldenburg. Thermal model of ocean ridges. *Nature*, 242: 137–139, 1973.

B. Parsons and J.G. Sclater. An analysis of the variation of ocean floor bathymetry and heat flow with age. *J. Geophys. Res.*, 82:803–827, 1977.

M.E. Pasyanos, W.R. Walter, and S.E. Hazler. A surface wave dispersion study of the Middle East and North Africa for monitoring the comprehensive nuclear-test-ban treaty. *Pure App. Geophys.*, 158:1445–1474, 2001.

A. Paul, A. Kaviani, D. Hatzfeld, J. Vergne, and Mokhtari. M. Seismological evidence for crustal-scale thrusting in the Zagros mountain belt (Iran). *Geophys. J. Int.*, 166:227–237, 2006.

J.A. Pearce, J.F. Bender, S.E. DeLong, W.S.F. Kidd, P.J. Low, Y. Guner, F. Saroglu, Y. Yilmaz, S. Moorbath, and J.G. Mitchell. Genesis of collision volcanism in eastern Anatolia, Turkey. *J. Volcanol. Geotherm. Res.*, 44(1-2):189–229, 1990.

Charles F Richter. *Elementary Seismology.* 1958.

Andreas Rietbrock and Frank Scherbaum. Acoustic imaging of earthquake sources from the Chalfant Valley, 1986, aftershock series. *Geophysical Journal International*, 119(1):260–268, 1994.

J. Ritsema and H.-J. van Heijst. Constraints on the correlation of P- and S-wave velocity heterogeneity in the mantle from P, PP, PPP and PKPab traveltimes. *Geophys. J. Int.*, 149:482–489, 2002.

J. Ritsema, H.J. van Heijst, and J.H. Woodhouse. Global transition zone tomography. *J. Geophys. Res.*, 106(B02302), 2004. 10.1029/2003JB002610.

M.H. Ritzwoller and A.L. Levshin. Eurasian surface wave tomography: Group velocities. *J. Geophys. Res.*, 103:4839–4878, 1998.

M.H. Ritzwoller, A.L. Levshin, L.I. Ratnikova, and A.A. Egorkin. Intermediate-period group-velocity maps across Central Asia, western China and parts of the Middle East. *Geophys. J. Int.*, 134:315–328, 1998.

A.R. Rodgers, J.F. Ni, and T.M. Hearn. Propagation characteristics of short–period S_n and L_g in the Middle East. *B. Seismol. Soc. Am.*, 87:396–413, 1997.

Garry Rogers and Herb Dragert. Episodic tremor and slip on the cascadia subduction zone: The chatter of silent slip. *Science*, 300(5627):1942–1943, 2003.

B. Romanowicz. Using seismic waves to image Earth's internal structure. *Nature*, 451:266–268, 2008.

Charlotte Rowe, Richard Aster, B Borchers, and Christopher Young. An automatic, adaptive algorithm for refining phase picks in large seismic data sets. *Bulletin of the Seismological Society of America*, 92(5):1660–1674, 2002.

E. Sandvol, K. Al-Damegh, A. Calvert, D. Seber, M. Barazangi, R. Mohamad, R. Gok, N. Turkelli, and C. Gurbuz. Tomographic imaging of L_g and S_n propagation in the Middle East. *Pure App. Geophys.*, 158:1121–1163, 2001.

C D Saragiotis, L J Hadjileontiadis, and S.M Panas. Pai–s/k: A robust automatic seismic p phase arrival identification scheme. *IEEE Transactions on Geoscience and Remote Sensing*, 40(6):1395–1404, Jul 2002.

Claudio Satriano, Anthony J Lomax, and Aldo Zollo. Real-time evolutionary earthquake location for seismic early warning. *Bulletin of the Seismological Society of America*, 98(3):1482–1494, 2008.

Laura Scognamiglio, Elisa Tinti, Alberto Michelini, Doug Dreger, Antonella Cirella, Massimo Cocco, Salvatore Mazza, and Alessio Piatanesi. Fast Determination of Moment Tensors and Rupture History: what has been learnt from the April 6th 2009, L'Aquila Earthquake. *SRL, under revision*, 2010.

Peter M Shearer. Global seismic event detection using a matched filter on long-period seismograms. *J. Geophys. Res.*, 99(B7):13713–13725, 1994.

L. Sichoix, A. Bonneville, and M.K. McNutt. The seafloor swells and Superswell in French Polynesia. *J. Geophys. Res.*, 103(B11):27,123–27,133, 1998.

A. Sieminski, Q. Liu, J. Trampert, and J. Tromp. Finite-frequency sensitivity of surface waves to anisotropy based upon adjoint methods. *Geophys. J. Int.*, 168: 1153–1174, 2007a.

A. Sieminski, Q. Liu, J. Trampert, and J. Tromp. Finite-frequency sensitivity of body waves to anisotropy based on adjoint methods. *Geophys. J. Int.*, 171:368–389, 2007b.

K. Sigloch and G. Nolet. Measuring finite-frequency body-wave amplitudes and traveltimes. *Geophys. J. Int.*, 167:271–287, 2006.

R. Sleeman and T. van Eck. Single station real-time P and S phase pickers for seismic observatories. In T. Takami and G. Kitagawa, editors, *Methods and Applications of Signal Processing in Seismic Network Operations*, volume 98 of *Lecture Notes in Earth Sciences*, pages 173–194. Springer, 2003.

D.B. Smith, M.H. Ritzwoller, and N.M. Shapiro. Stratification of anisotropy in the Pacific upper mantle. *J. Geophys. Res.*, 109, 2004. 10.1029/2004JB003200.

W.H.F. Smith and T. Sandwell. Global seafloor topography from satellite altimetry and ship depth soundings. *Science*, 277:1956–1962, 1997.

C.A. Stein and S. Stein. A model for the global variation in oceanic depth and heat flow with lithospheric age. *Nature*, 359:123–129, 1992.

E. Stutzmann, M. Schimmel, G. Patau, and A. Maggi. Global climate imprint on seismic noise. *Geochem. Geophys. Geosyst.*, 10, 2009.

D. Suetsugu, T. Isse, S. Tanaka, M. Obayashi, H. Shiobara, H. Sugioka, T. Kanazawa, Y. Fukao, G. Barruol, and D. Reymond. South Pacific mantle plumes imaged by seismic observation on islands and seafloor. *Geochem. Geophys. Geosyst.*, 10(11), 2009.

C. Tape, Q. Liu, and J. Tromp. Finite-frequency tomography using adjoint methods—Methodology and examples using membrane surface waves. *Geophys. J. Int.*, 168:1105–1129, 2007.

C. Tape, Q. Liu, A. Maggi, and J. Tromp. Adjoint tomography of the southern California crust. *Science*, 325:988–992, 2009.

C. Tape, Q. Liu, A. Maggi, and J. Tromp. Seismic tomography of the southern California crust based on spectral-element and adjoint methods. *Geophys. J. Int.*, 180:433–462, 2010.

A. Tarantola. Inversion of seismic reflection data in the acoustic approximation. *Geophysics*, 49:1259–1266, 1984.

J. Trampert and J. Spetzler. Surface wave tomography: finite-frequency effects lost in the null space. *Geophys. J. Int.*, 164:394–400, 2006.

J. Trampert and J.H. Woodhouse. Global phase velocity of Love and Rayleigh waves between 40 and 150 seconds. *Geophys. J. Int.*, 22:675–690, 1995.

J. Tromp, C. Tape, and Q. Liu. Seismic tomography, adjoint methods, time reversal and banana-doughnut kernels. *Geophys. J. Int.*, 160:195–216, 2005.

Hiroshi Tsuruoka, Hitoshi Kawakatsu, and Taku Urabe. GRiD MT (grid-based real-time determination of moment tensors) monitoring the long-period seismic wavefield. *Physics of the Earth and Planetary Interiors*, 175(1-2):8–16, 2009.

S. Van der Lee and G. Nolet. Upper mantle S velocity structure of North America. *J. Geophys. Res.*, 102:22,815–22,838, 1997.

H.J. Van Heijst and J.H. Woodhouse. Measuring surface-wave overtone phase velocities using a mode-branch stripping technique. *Geophys. J. Int.*, 131:209–220, 1997.

J.C. VanDecar and R.S. Crosson. Determination of teleseismic relative phase arrival times using multi-channel cross-correlation and least squares. *B. Seismol. Soc. Am.*, 80:150–169, 1990.

John E Vidale, E S Cochran, H Kanamori, and R W Clayton. After the lightning and before the thunder: non-Omori behavior of early aftershocks? *Eos Trans. AGU*, 84(46), 2003. Fall Meet. Suppl., Abstract S31A-08.

K. Visser, S. Lebedev, J. Trampert, and B. L. N. Kennett. Global Love wave overtone measurements. *Geophy. Res. Lett.*, 34:L03302, 2007. doi: 10.1029/2006GL028671.

F. Waldhauser and D.P. Schaff. Large-scale relocation of two decades of northern California seismicity using cross-correlation and double-difference methods. *J. Geophys. Res.*, 113(8):B08311, 2008.

Felix Waldhauser. Near-Real-Time Double-Difference Event Location Using Long-Term Seismic Archives, with Application to Northern California. *Bulletin of the Seismologica Society of America*, 99(5):2736–2748, 2009.

Kristoffer T Walters, Miaki Ishii, and Peter M Shearer. Rupture details of the 28 March 2005 Sumatra Mw 8.6 earthquake imaged with teleseismic P waves. *Geophys. Res. Lett.*, 32, 2005.

Aaron G Wech and Kenneth C Creager. Automated detection and location of cascadia tremor. *Geophys. Res. Lett.*, 35, 2008.

M. Withers, R. Aster, C. Young, J. Beiriger, M. Harris, S. Moore, and J. Trujillo. A comparison of select trigger algorithms for automated global seismic phase and event detection. *B. Seismol. Soc. Am.*, 88:96–106, 1998a.

Mitchell Withers, Richard Aster, Christopher Young, Judy Beiriger, Mark Harris, Susan Moore, and Julian Trujillo. A comparison of select trigger algorithms for automated global seismic phase and event detection. *Bulletin of the Seismological Society of America*, 88(1):95–106, 1998b.

Mitchell Withers, Richard Aster, and Christopher Young. An automated local and regional seismic event detection and location system using waveform correlation. *Bulletin of the Seismological Society of America*, 89(3):657–669, 1999.

K. Yoshizawa and B.L.N. Kennett. Non-linear waveform inversion for surface waves with a neighbourhood algorithm—application to multimode dispersion measurements. *Geophys. J. Int.*, 149:118–133, 2002.

Christopher Young, Mark Harris, Judy Beiriger, Susan Moore, Julian Trujillo, Mitchell Withers, and Richard Aster. The waveform correlation event detection system project phase 1: issues in prototype development and testing. Technical Report SAND96-1916, Aug 1996.

T.R. Zhang and T. Lay. Evolution of oceanic upper mantle structure. *Phys. Earth Planet. Interiors*, 114:71–80, 1999.

Y.-S. Zhang and T. Tanimoto. Global Love wave phase velocity variation and its significance to plate tectonics. *Phys. Earth Planet. Interiors*, 66:160–202, 1991.

L. Zhao, T.H. Jordan, and C.H. Chapman. Three dimensional fréchet differential kernels for seismic delay times. *Geophys. J. Int.*, 141:558–576, 2000.

L. Zhao, T. H. Jordan, K. B. Olsen, and P. Chen. Fréchet kernels for imaging regional earth structure based on three-dimensional reference models. *B. Seismol. Soc. Am.*, 95:2066–2080, 2005.

Y. Zhou, G. Nolet, F. A. Dahlen, and G. Laske. Global upper-mantle structure from finite-frequency surface-wave tomography. *J. Geophys. Res.*, 111:B04304, 2006. doi: 10.1029/2005JB003677.

Curriculum Vitae

Personal Information

Name :	Alessia Maggi
Date of birth :	18 / 12 / 1975
Place of birth :	Tradate, Italy
Nationality :	Italian
Position :	Physicien Adjoint
Professional address :	Ecole et Observatoire des Sciences de la Terre 5 rue René Descartes, 67084 Strasbourg Cedex
Tel :	+33 (0)3 90 24 50 28
Fax :	+33 (0)3 90 24 01 25
E-mail :	alessia.maggi@unistra.fr

Professional positions

2005 – present :	Physicien Adjoint l'Ecole et Observatoire des Sciences de la Terre, Strasbourg. *In charge of the Global Seismological Observatories.*
2005 :	Post doctorate at the Seismological Laboratory, California Institute of Technology, Pasadena CA. *Towards full waveform tomography using the adjoint method.*
2002 – 2004 :	Post doctorate at Université Louis Pasteur, Strasbourg (Marie Curie Individual Fellowship). *Surface wave tomography of the upper mantle under the Pacific Ocean.*
1998 – 2002 :	Ph.D. in Seismology at Bullard Laboratories, Cambridge University, UK. *Structure and Deformation from the Alps to the Himalayas.*

Grants / awards

2010 – 2013 :	co-I of NERA (Network of European Research Infrastructures for Earthquake Risk Assessment and Migitation) funded by EEC-FP7
2010 – 2013 :	co-I of PYROPE (PYRenean Observational Portable Experiment) funded by Agènce Nationale de la Recherche
2009 – 2012 :	co-I of DoRA (Dynamics of Rifting in Afar) funded by Agènce Nationale de la Recherche
2008 – 2011 :	co-PI of CASE-IPY (Concordia, Antarctica, Seismic Experiment for the International Polar Year) funded by Agènce Nationale de la Recherche
2006 – 2009 :	co-I of SIMBAAD (Seismic Imaging of the Mantle Beneath the Aegean-Anatolian Domain) funded by Agènce Nationale de la Recherche
2005 :	Post-doctoral grant, Caltech, Pasadena CA, USA.
2002 – 2004 :	Marie Curie Individual Fellowship.

Current Responsibilities

- Observatory
  - In charge of the Global Seismological Observatories, EOST, Strasbourg (stations in Antarctica, southern Indian Ocean, Africa and France)

- Administration
    - Member of Observatory Commission (EOST)
    - Member of Laboratory Council (IPGS)
    - Deputy chair of the Scientific Experts Committee (EOST)
    - Member of French Pilot Committee for Tsunami Warning in the Indian Ocean (SATOI / CNATOI)
    - Representative of France for Solid Earth Geophysics to SCAR (Scientific Committee on Antarctic Research)
- Teaching
    - Inverse theory and signal processing (Masters) - Lectures and Practicals
    - Earthquake seismology (Masters + Engineering School) - Practicals
    - Masters projects (first and second years):
        - 2010 : 4 x M1 projects, 1 x M2 project (Basile Hector: *Towards detection and high resolution location of regional earthquakes using continuous waveforms*; PhD with Jacques Hinderer, EOST, 2011)
        - 2009 : 3 x M1 projects
        - 2008 : 1 x M2 project (Joanne Buckenmeyer: *The detectability of mantle plumes*; PhD with Sergei Lebedev, Institute for Advanced Studies, Dublin)
        - 2007 : 1 x M1 project

Peer reviewed publications

D.D. Dunlap, A. Maggi, M.R. Soria, and L. Monaco. Nanoscopic structure of dna condensed for gene delivery. *Nucleic Acids Research*, 25(15):3095–3101, 1997.

A. Maggi, J.A. Jackson, D. McKenzie, and K. Priestley. Earthquake focal depths, effective elastic thickness, and the strength of the continental lithosphere. *Geology*, 28:495–498, 2000a.

A. Maggi, J.A. Jackson, K. Priestley, and C. Baker. A re–assessment of focal depth distribution in southern Iran, the Tien Shan and northern India: Do earthquakes really occur in the continental mantle? *Geophys. J. Int.*, 143:629–661, 2000b.

A. Maggi, K. Priestley, and J. Jackson. Focal depths of moderate and large size earthquakes in Iran. *J. Seismology and Earthquake Engineering*, 4(2-3):1–10, 2002.

R. Saunders, K. Kneissl, W. Grainge, M. Grainger, M. Jones, A. Maggi, et al. A measurement of h_0 from Ryle Telescope, *asca* and rosat observations of Abell 773. *Mon. Not. R. Astron. Soc.*, 341:937–940, 2003.

S. Pilidou, K. Priestley, J. Jackson, and A. Maggi. The 1996 cyprus earthquake: a large deep event in the cyprean arc. *Geophys. J. Int.*, 158(85-97), 2004.

A. Maggi and K. Priestley. Surface waveform tomography of the Turkish Iranian plateau. *Geophys. J. Int.*, 160(3):1068–1080, 2005.

A. Maggi, E. Debayle, G. Barruol, and K. Priestley. Multi-mode surface waveform tomography of the Pacific Ocean: a close look at the lithospheric cooling signature. *Geophys. J. Int.*, 166:1384–1397, 2006a.

A. Maggi, E. Debayle, and K. Priestley. Azimuthal anisotropy of the Pacific Ocean upper mantle. *Earth Planet. Sc. Lett.*, 250:53–71, 2006b.

A. Maggi, C. Tape, M. Chen, D. Chao, and J. Tromp. An automated time-window selection algorithm for seismic tomography. *Geophys. J. Int.*, 178:257–281, 2009.

C. Tape, Q. Liu, A. Maggi, and J. Tromp. Adjoint tomography of the southern California crust. *Science*, 325:988–992, 2009.

E. Stutzmann, M. Schimmel, G. Patau, and A. Maggi. Global climate imprint on seismic noise. *Geochem. Geophys. Geosyst.*, 10, 2009.

C. Tape, Q. Liu, A. Maggi, and J. Tromp. Seismic tomography of the southern California crust based on spectral-element and adjoint methods. *Geophys. J. Int.*, 180:433–462, 2010.

J.J. Lévêque, A. Maggi, and A. Souriau. Seismological constraints on ice properties at Dome C, Antarctica, from h/v measurements. *Antarctic Science*, 2010.

A. Maggi and A. Michelini. Continuous waveform seismic event detection and location: Application to the L'Aquila 2009 earthquake sequence. (submitted) *Geophys. J. Int.*, 2010.

M. Grob, A. Maggi, and E. Stutzmann. Antarctic ice-floe and seismic noise. (in prep) *Geophy. Res. Lett.*, 2010.

Résumé

Les sujets de recherche que j'ai choisi de traiter ces dix dernières années sont relativement éclectiques, couvrant des aspects relatifs tant aux sources sismiques qu'à la structure de la Terre. Un thème fédérateur qui émerge cependant est mon intérêt pour les nombreuses méthodes utilisées en sismologie pour extraire l'information pertinente des sismogrammes. Dans cette thèse d'habilitation, je parcours le fil conducteur des idées qui ont contribué à former ma pensée sur ce thème, décrivant avec plus de détails deux méthodes que j'ai développées et qui ont abouti récemment: FLEXWIN, qui permet d'identifier automatiquement dans un sismogramme complexe les fenêtres temporelles de mesure les plus appropriées dans un certain contexte, et WaveLoc, qui détecte et localise automatiquement les phénomènes sismiques à partir de formes d'ondes continues en exploitant la cohérence de l'information sur un réseau de stations sismologiques. De tels outils, basés au départ sur l'intégration du savoir-faire "artisanal" et son automatisation, permettent en fait d'aller plus loin dans l'exploitation des sismogrammes, et sont devenus indispensables au sismologue pour faire face au volume de données gigantesque produit par les réseaux sismologiques modernes.

Mot-clefs

sismologie, formes d'ondes, source, structure

Title

Du sismogramme complexe à l'information pertinente : exemples dans le domaine des sources et des structures.

Abstract

My choice of research projects over the past decade has been rather eclectic, covering aspects relating to both seismic sources and Earth structure. There is, however, a consistent theme, and that is a fascination with the large variety of methods for extracting pertinent information from seismic data. In this thesis, I give an brief, largely chronological outline of the steps and insights that have informed my current thinking on this theme, going into more detail on two methods that I have recently developed: FLEXWIN, for automatically selecting the most appropriate time-windows on complex seismograms in which to make measurements, and WaveLoc, for automatically detecting and locating seismic phenomena from continuous waveform data by exploiting the coherence of information across a seismic network. Such tools, based on the the integration and automation of practical seismological "know-how", allow us to exploit seismological data more completely, and are becoming indispensable in the context of the enormous volume of data produced by modern seismic networks.

Keywords

seismology, waveforms, source, structure

Adrr : EOST, 5 rue Renè Descartes, 67084 Strasbourg, Cedex